

AD 731090

DASA 2678  
August 1971

**MATERIAL MODEL STUDIES  
FOR ROCKS AND SOILS**

- I. Shock Conditioned Behavior Model for Granite, by M. H. Wagner
- II. General Constitutive Relations for Rocks and Soils, by M. Rosenblatt
- III. Fracture Model for Rocks, by M. Rosenblatt and S. Timurtas

Prepared for  
**DEFENSE NUCLEAR AGENCY**  
Washington, D.C. 20305  
Under NWER Subtask SB047  
Contract DASA 01-68-C-0044

DDC  
RECEIVED  
OCT 13 1971  
B

Reproduced by  
**NATIONAL TECHNICAL  
INFORMATION SERVICE**  
Springfield, Va. 22151

**SHOCK HYDRODYNAMICS INCORPORATED**  
18010 VENTURA BOULEVARD  
SHERMAN OAKS, CALIFORNIA 91403  
A SUBSIDIARY OF **Whittaker**

Approved for public release; distribution unlimited.

129

UNCLASSIFIED

Security Classification

## DOCUMENT CONTROL DATA - R &amp; D

(Security classification of title, body of abstract and indexing annotation must be entered when the overall report is classified)

1. ORIGINATING ACTIVITY (Corporate author)

SHOCK HYDRODYNAMICS INCORPORATED

2a. REPORT SECURITY CLASSIFICATION

UNCLASSIFIED

2b. GROUP

N/A

3. REPORT TITLE

MATERIAL MODEL STUDIES FOR ROCKS AND SOILS, PART I: SHOCK CONDITIONED BEHAVIORAL MODEL FOR GRANITE, PART II: GENERAL CONSTITUTIVE RELATIONS FOR ROCKS AND SOILS, PART III: FRACTURE MODEL FOR ROCKS

4. DESCRIPTIVE NOTES (Type of report and inclusive dates)

Technical Report

5. AUTHOR(S) (First name, middle initial, last name)

Part I: Mark H. Wagner

Part II: Martin Rosenblatt

Part III: Martin Rosenblatt and Si Timurtas

6. REPORT DATE

August 1971

7a. TOTAL NO. OF PAGES

109

7b. NO. OF REFS

34

8a. CONTRACT OR GRANT NO.

DASA01-68-C-0044

8b. ORIGINATOR'S REPORT NUMBER(S)

9. PROJECT NO.

NWER XANS

c.

Task and Subtask B047

9b. OTHER REPORT NO(S) (Any other numbers that may be assigned this report)

d. Work Unit 02

DASA 2678

11. DISTRIBUTION STATEMENT

Approved for public release; distribution unlimited

12. SUPPLEMENTARY NOTES

13. SPONSORING MILITARY ACTIVITY

Director  
Defense Nuclear Agency  
Washington, D. C. 20305

14. ABSTRACT

Results are described for three tasks in a continuing analytical study of rocks and soils:

I. Shock Conditioning - Post-shot measurements show gradual degradation of rock media physical properties as the range from underground nuclear events decreases. These changes correlate with the peak shock pressures to which the media has been exposed. The degraded physical properties affect the propagation of waves behind the shock, and thereby influence the decaying wave profile. A model incorporating the measured properties of granite at the HARD HAT site, before and after shocking to various levels, has been formulated and incorporated into a 1-D Lagrangian code. Predictions are made of free field motions at the nearby PILE DRIVER site. The predicted waveform in the decay and recovery phases obtained with the shock-conditioned model shows significantly better agreement with measured waveforms than are obtained with uniform field models.

II. General Model for Rocks and Soils - A phenomenological model is described which incorporates dilatancy (as controlled by inelastic shear deformation), hysteresis (as a function of maximum density experienced in loading), strain rate effects on inelastic deformation, and a dependence of inelastic shear deformation on proximity of the stress state to the static failure surface. The method of determining the material parameters from experimental data is outlined. The model is applied with satisfactory agreement to quasi-static data for triaxially loaded granite. The differential equations defining this model are hyperbolic, thereby assuring uniqueness.

DD FORM 1473  
1 NOV 65

UNCLASSIFIED

Security Classification

UNCLASSIFIED

Abstract (Continued)

III. Failure Model for Rocks - Triaxial extension and compression failure data for granite and limestone cannot be fit by one curve in maximum shear stress vs pressure plots. Thus the failure surface in these media cannot be described by the familiar von Mises, Prager-Drucker, or Tresca yield models. Extensive data for limestone failure were analyzed in this task. On the  $\pi_1$  plane, these data are first fit by a general quadric. Nearly straight-line fits are obtained, with the slopes being a function of pressure. A modified Coulomb failure model, incorporating a dependence on pressure and a test for tensile failure, is introduced and fit to the limestone data.

14. KEY WORDS

Constitutive Relations  
Rocks  
Soils  
Fracture Model  
Shock Condition  
Dilatance  
Strain Rate Effects  
Underground Nuclear Explosions

UNCLASSIFIED

DASA 2678  
August 1971

**MATERIAL MODEL STUDIES  
FOR ROCKS AND SOILS**

- I. Shock Conditioned Behavior Model for Granite, by M. H. Wagner
- II. General Constitutive Relations for Rocks and Soils, by M. Rosenblatt
- III. Fracture Model for Rocks, by M. Rosenblatt and S. Timurtas

Prepared for  
**DEFENSE NUCLEAR AGENCY**  
Washington, D.C. 20305  
Under NWER Subtask SE047  
Contract DASA 01-68-C-0044

**SHOCK HYDRODYNAMICS INCORPORATED**  
15010 VENTURA BOULEVARD  
SHERMAN OAKS, CALIFORNIA 91403

A SUBSIDIARY OF  **General Dynamics**

Approved for public release; distribution unlimited.

Disposition: Destroy this report when it is no longer needed. Do not return to sender.

## ABSTRACT

Results are described for three tasks in a continuing analytical study of rocks and soils.

**I. Shock Conditioning** - Post-shot measurements show gradual degradation of rock media physical properties as the range from underground nuclear events decreases. These changes correlate with the peak shock pressures to which the media has been exposed. The degraded physical properties affect the propagation of waves behind the shock, and thereby influence the decaying wave profile. A model incorporating the measured properties of granite at the HARD HAT site, before and after shocking to various levels, has been formulated and incorporated into a 1-D Lagrangian code. Predictions are made of free field motions at the nearby PILE DRIVER site. The predicted waveform in the decay and recovery phases obtained with the shock-conditioned model shows significantly better agreement with measured waveforms than are obtained with uniform field models.

**II. General Model for Rocks and Soils** - A phenomenological model is described which incorporates dilatancy (as controlled by inelastic shear deformation), hysteresis (as a function of maximum density experienced in loading), strain rate effects on inelastic deformation, and a dependence of inelastic shear deformation on proximity of the stress state to the static failure surface. The method of determining the material parameters from experimental data is outlined and the model is applied with satisfactory agreement to quasi-static data for triaxially loaded granite. The differential equations defining this model are hyperbolic, thereby assuring uniqueness.

**III. Failure Model for Rocks** - Triaxial extension and compression failure data for granite and limestone cannot be fit by one curve in maximum shear stress vs pressure plots. Thus the failure surface in these media cannot be described by the familiar von Mises, Prager-Drucker, or Tresca yield models. Extensive data for limestone failure were analyzed in this task. On the  $\pi_1$  plane, these data are first fit by a general quadric. Nearly straight-line fits are obtained, with the slopes being a function of pressure. A modified Coulomb failure model, incorporating a dependence on pressure and a test for tensile failure, is introduced and fit to the limestone data.

**BLANK PAGE**

# CONTENTS

Page

## PART I - Shock Conditioned Behavioral Model for Granite

I-1	INTRODUCTION . . . . .	1
I-1.1	Background . . . . .	1
I-1.2	Scope of Effort . . . . .	1
I-2	SHOCK CONDITIONING AND FREE FIELD RESPONSE . . . . .	3
I-2.1	Waveform Characteristics . . . . .	3
I-2.2	Past Efforts to Analyze Waveform . . . . .	2
I-2.3	Conditioning Effects of the Shock Wave . . . . .	5
I-3	PROPERTIES AND MODELING OF NTS GRANITE . . . . .	8
I-3.1	Pre-Shot Properties . . . . .	10
I-3.2	Equation of State . . . . .	10
I-3.3	Properties of Shocked NTS Granite . . . . .	12
I-3.4	Shock Conditioning Model . . . . .	17
I-4	NUMERICAL SOLUTIONS . . . . .	20
I-4.1	Problem Description . . . . .	20
I-4.2	Solution Results . . . . .	23
I-5	CONCLUSIONS AND RECOMMENDATIONS. . . . .	32
I-6	REFERENCES FOR PART I . . . . .	36

## PART II - General Constitutive Relations for Rocks

II-1	INTRODUCTION . . . . .	39
II-2	CONSTITUTIVE EQUATIONS . . . . .	39
II-3	SOME COMPARISONS OF THE PROPOSED MODEL AND THE ELASTIC-PLASTIC MODEL . . . . .	43
II-4	FITTING THE MODEL TO EXPERIMENTAL DATA . . . . .	45
II-4.1	An Example of the Technique for Determining the Material Parameters in the Proposed Model . . . . .	46
II-5	UNIQUENESS OF SOLUTIONS . . . . .	70
II-6	TABLE OF SYMBOLS FOR PART II . . . . .	79
II-7	REFERENCES FOR PART II . . . . .	81

CONTENTS (Cont'd)

PART III - FRACTURE MODEL FOR ROCKS

	Page
III-1.	INTRODUCTION . . . . . 83
III-2.	MATHEMATICAL DESCRIPTION OF THE ROTATED PRINCIPAL STRESS SPACE . . . . . 85
III-3.	DETERMINATION OF THE STATIC FAILURE SURFACE FOR SOLENHOFEN LIMESTONE . . . . . 90
III-3.1	The Least Square Fit to the Limestone Fracture Data . . . . . 90
III-3.2	A Physical Model for the Limestone Failure Surface . . . . . 94
III-3.3	Comparison with Recent Biaxial Stress Data . . . . . 98
III-4.	SUMMARY AND RECOMMENDATIONS . . . . . 101
III-5.	REFERENCES FOR PART III . . . . . 102

**PART I**  
**SHOCK CONDITIONED BEHAVIORAL MODEL**  
**FOR GRANITE**  
by M. H. Wagner

**I-1.     INTRODUCTION**

**I-1.1    BACKGROUND**

A number of investigations<sup>1-6\*</sup> have been concerned with prediction of the free-field ground motions for the HARD HAT and PILE DRIVER events. Through these studies an improved understanding of the problem evolved, but the remaining uncertainties and technical difficulties were sufficient to preclude fully satisfactory predictions of these large-scale response data. The central problem associated with the computations has been the attainment of an adequate prediction of the observed waveshape. The importance of a number of medium properties and of mechanisms operative in these events (e.g., coupling characteristics, radiation deposition, water content, porosity, and block motion) were investigated in the previous studies. From work on correlating mechanisms with various features of the observed free-field wave profiles<sup>6</sup>, it was hypothesized that the inclusion of shock conditioning or metamorphic effects in the granite medium model would provide improved predictions of the free-field response. The objective of the present study was to evaluate these effects through development of appropriate constitutive relations, followed by application of these in computations of the PILE DRIVER event.

**I-1.2    SCOPE OF EFFORT**

The program effort allocated to this study was limited to an evaluation of the significance of shock conditioning effects to prediction results, i.e., to determine if such effects appear sufficiently important to warrant their inclusion in future free-field calculations. There was therefore no attempt made to formulate a complete constitutive model which might provide a very close quantitative duplication of the PILE DRIVER experimental results. Such efforts are probably not justified, in any case, in view of the very limited experimental data available. The primary significance of the experimental results lies in the major characteristics of the waveform that are revealed, such as its broad decay and the recovery phase, which in turn imply the presence of certain medium properties or mechanisms which should be accounted for in the theoretical behavioral model.

\*Superscripts are reference numbers. The Reference List for Part I is on page 36.

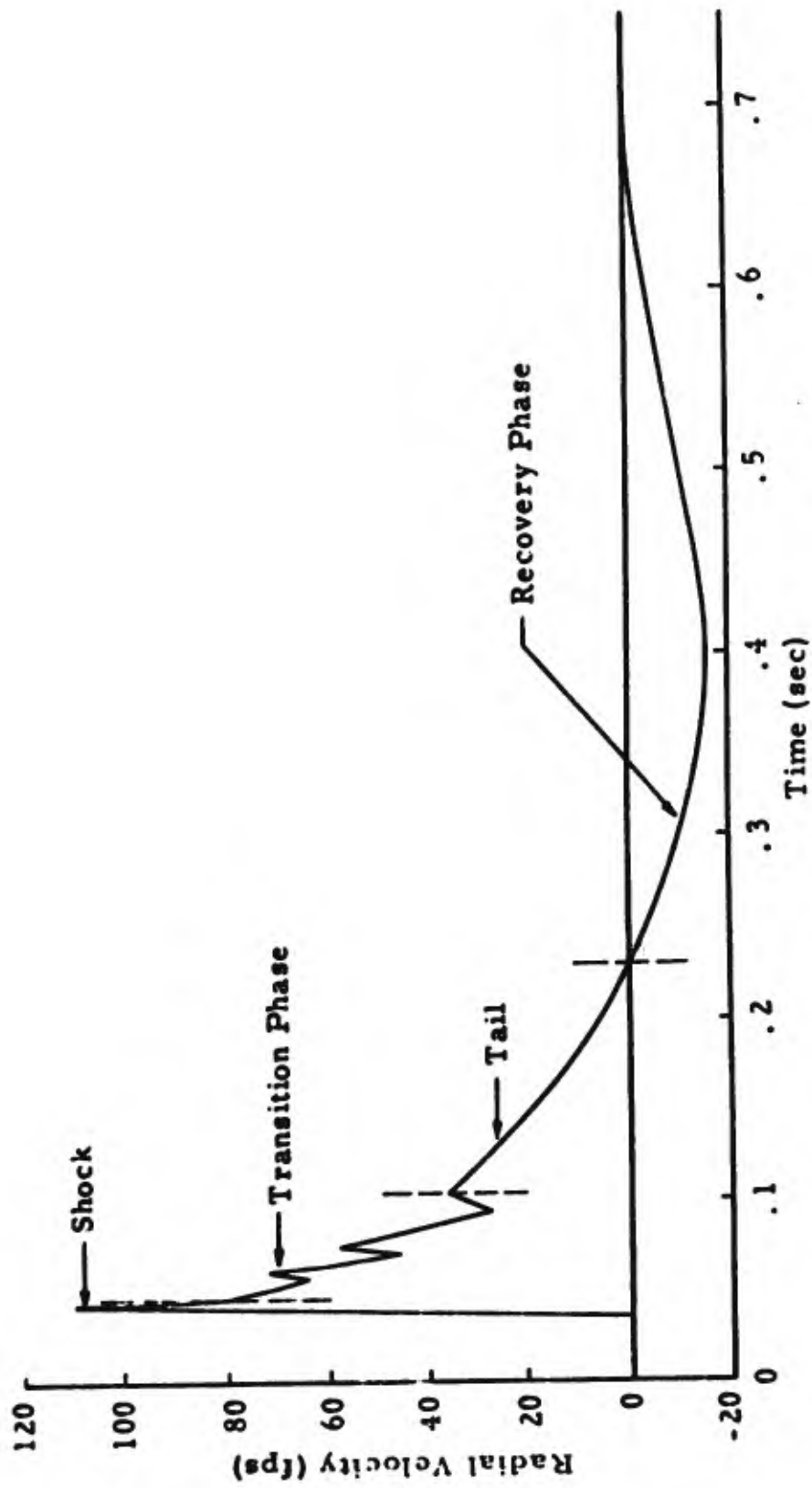


Figure 1. Observed Radial Velocity Profile at a Range of 668 ft.

## I-2. SHOCK CONDITIONING AND FREE FIELD RESPONSE

### I-2.1 WAVEFORM CHARACTERISTICS

The measured free field waveform (Figure 1)<sup>7</sup> for PILE DRIVER may be viewed as having several distinguishable parts, denoted in the figure. The first part of the waveform, corresponding to the sharp rise in velocity, is attributable to passage of the shock wave produced by the impulsive load from the nuclear explosion. The transition phase, corresponding to the jagged decrease in velocity, is due to unloading (rarefaction) waves and is dependent on complex conditioning effects in the medium produced by the shock as well as wave interactions within and near the cavity. The conditioning effects referred to are vaporization, melting, softening, crushing, brecciation, fracture, etc., which in turn alter the material properties. The tail of the wave, corresponding to a smooth attenuation of velocity, is attributable to the late-stage cavity pressure, which forces growth of the cavity and thus material displacement beyond the cavity out into the free field. Upon cessation of cavity growth the positive-phase of the waveform ends, and the recovery phase is entered.\* A summary of the foregoing correlations, along with a list of the important parameters or properties which influence these mechanisms, is given in Table I.

### I-2.2 PAST EFFORTS TO ANALYZE WAVEFORM

Looking at the history of investigations to predict free-field ground motions, it is apparent that the earliest efforts concentrated on predicting the first phase of the waveform, i.e., the shock front. These efforts were generally successful in predicting the variation of wave arrival time, peak stress, and peak velocity with range. Subsequent studies have recognized the importance of the proper treatment of the cavity motion, with the result that predictions of peak displacement vs range have been notably improved. Some effort has more recently been made towards predicting the transition phase, and a number of mechanisms and effects have been suggested and evaluated. Of these, the most important appears to be the occurrence of dilatancy in the medium. The past studies paid little attention to the recovery phase of the waveform, and accurate predictions of the residual displacements have not yet been made.

The velocity waveforms from most of the early computations were characterized by a sharp spike followed immediately by a long duration trailing wave, i.e., there was usually little or no transition phase evident. In addition, the recovery phase in these computations was too shallow, resulting in residual displacements which were only slightly less than the peak values.

---

\*A discussion of the relationship between late-stage cavity motion and free-field response may be found in Reference 6.

TABLE I. CORRELATION OF OBSERVED RESPONSE WITH MECHANISMS AND MEDIA PROPERTIES

PART OF WAVE	RESPONSIBLE MECHANISM	IMPORTANT MEDIA PROPERTIES
Sharp Wave Front	<ul style="list-style-type: none"> <li>o Direct Shock</li> </ul>	<ul style="list-style-type: none"> <li>o Equation of State of Medium</li> <li>o Loading Yield Surface</li> </ul>
Transition Phase	<ul style="list-style-type: none"> <li>o Rarefaction Waves and Early Cavity-Medium Interactions</li> </ul>	<ul style="list-style-type: none"> <li>o Dilatancy</li> <li>o Sonic Velocity and Yield Strength (As Altered Due to Conditioning Effects of Shock)</li> </ul>
Tail	<ul style="list-style-type: none"> <li>o Late Stage Cavity Pressure Inducing Cavity Motion and Associated Free Field Displacement</li> </ul>	<ul style="list-style-type: none"> <li>o Yield Strength in Medium Near Cavity (As Altered by Shock)</li> <li>o Water Content of Medium Near Cavity</li> <li>o Equation of State of Cavity Gas</li> </ul>
Recovery Phase	<ul style="list-style-type: none"> <li>o Elastic Recovery</li> <li>o Adiabatic Unloading</li> </ul>	<ul style="list-style-type: none"> <li>o Local Yield Strength in Free Field</li> <li>o Equation of State of Medium</li> </ul>

### I-2.3      CONDITIONING EFFECTS OF THE SHOCK WAVE

Most of the behavioral models used in past investigations provided inadequate or no treatment of the modification of material properties due to passage of the shock wave. In some models, an attempt was made to predict the occurrence of fracture, but the modeling of the material characteristics subsequent to fracture was then inadequately treated. For most of the commonly used models, a yielding mechanism (such as a flow rule in conjunction with a failure surface) has been employed to simulate fracture. This yield model is typically applied to the entire granite field and it remains unchanged during the entire calculation. A substantial amount of evidence is available, however (e.g., References 8, 9, and 10), which proves that there are significant changes to important material properties due to passage of the shock wave from a nuclear explosion. Of particular value is the petrographic study conducted by Short<sup>8</sup> of shocked granodiorite in the vicinity of the HARD HAT event.

Various zones of characteristics or behavior may be used to describe the medium as the distance from the shot point increases and correspondingly as the intensity of the shock decreases. Thus, the closest-in zone may be designated as

- a. hydrodynamic, corresponding to the region of vaporized and melted rock, followed by a
- b. plastic zone,
- c. crushed zone,
- d. cracked zone, and
- e. virgin rock or unaltered zone.

There are no sharp demarcations between these zones, but rather a gradation of properties out to the virgin rock.

Since assignment of the strength of the rock has been shown to be of critical importance in predictions of the ground motions, variations in the strength due to shock processes are particularly important. The strength can be expected to vary with range as shown in Figure 2. As an example, data for the compressive strength of small specimens taken from the HARD HAT event, as reported by Short<sup>8</sup>, is shown in Figure 3.

The rock strength is influential on at least two important mechanisms, viz.,

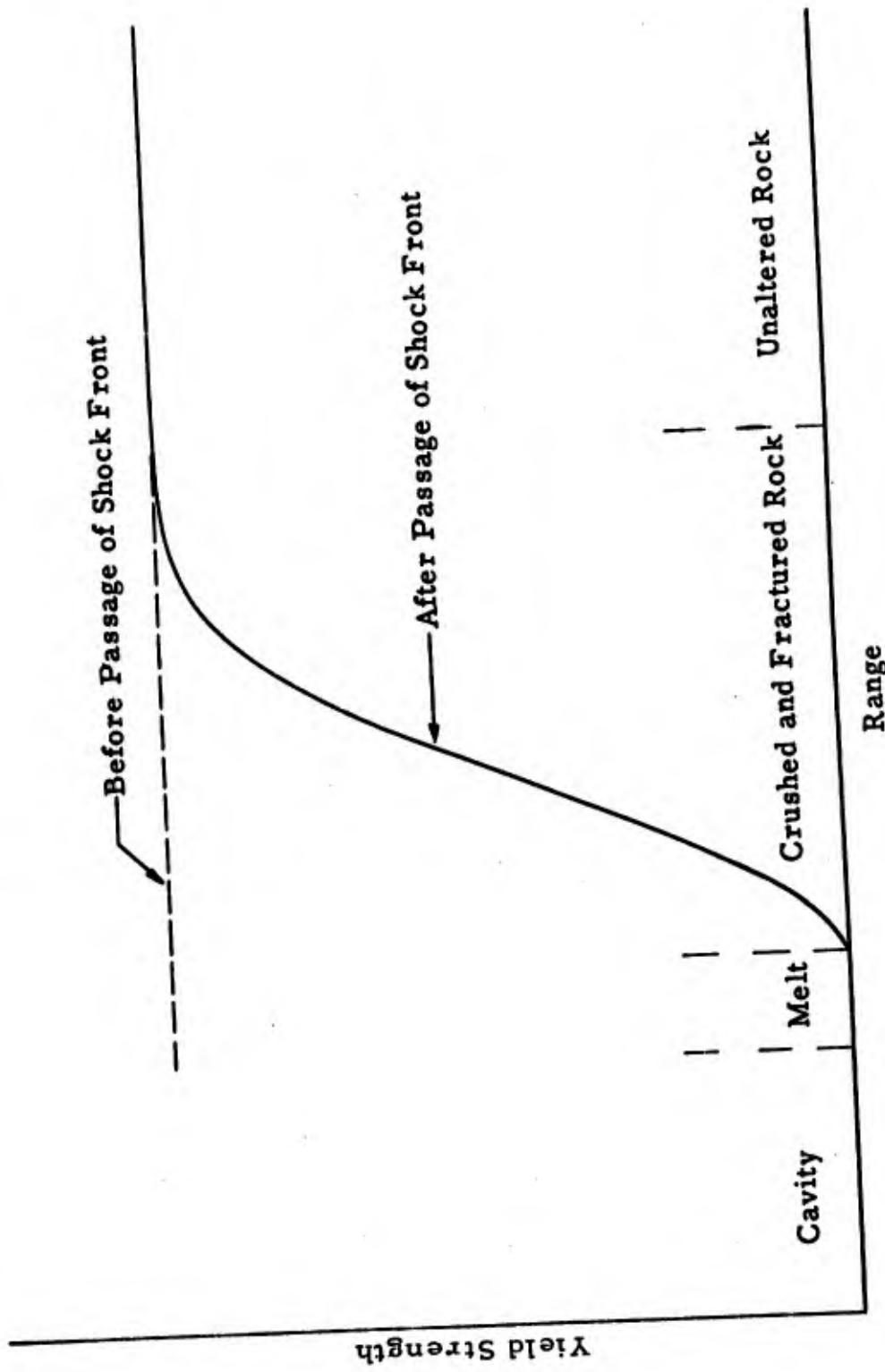


Figure 2. Schematic Variation of Strength of Rock With Range

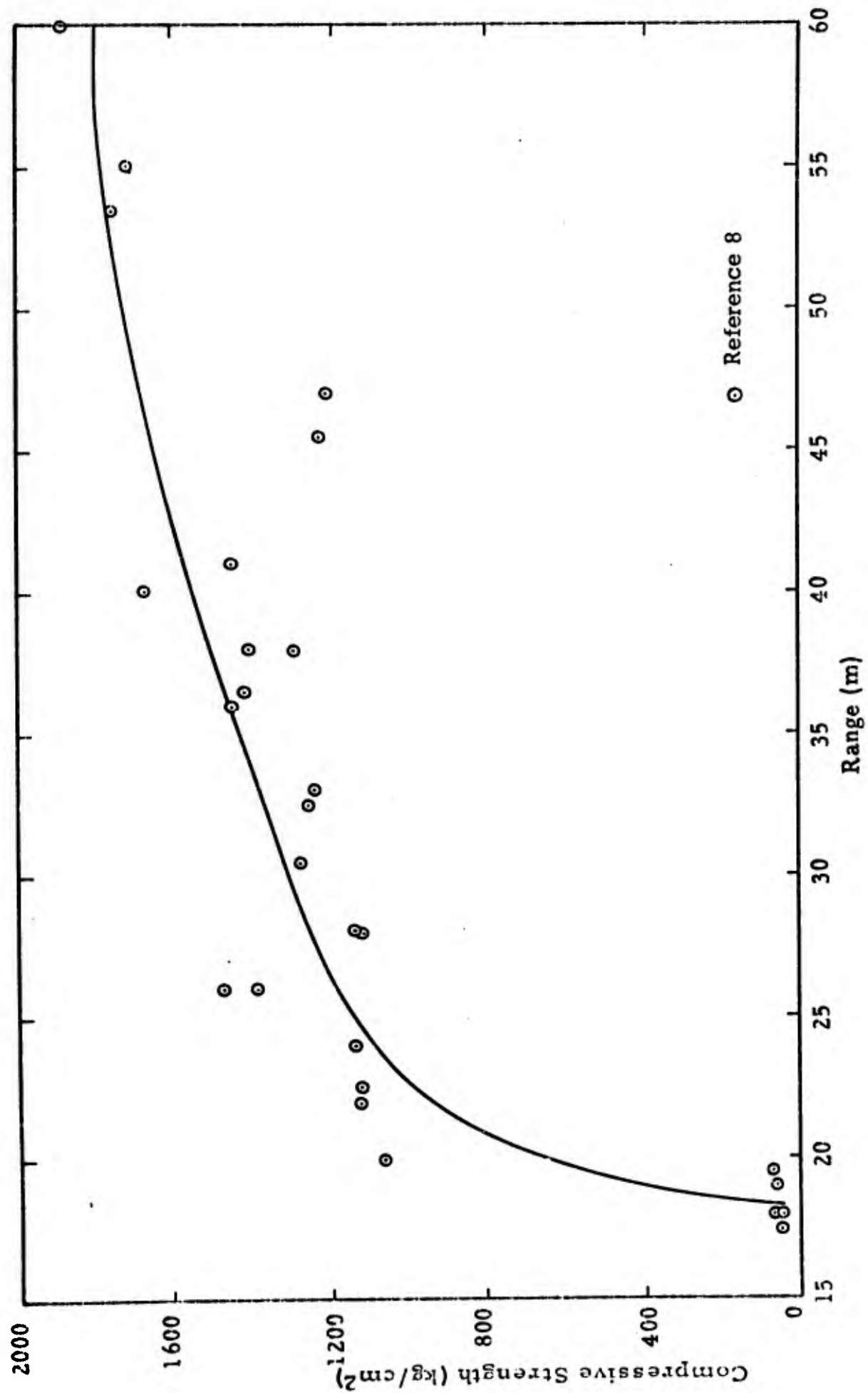


Figure 3. . Post-Shot Compressive Strength vs Range (HARD HAT)

- a. the cavity motion, due to the reduced post-shock strength of material next to the cavity, and
- b. recovery of the peak displacements in the far field, due to the weaker shock and thus higher strength remaining there.

Another important property affected by the shock is the longitudinal wave velocity, caused by the reduction of shear strength and increase of compressibility in the damaged material. A plot of Short's data for sonic velocity vs range for HARD HAT is shown in Figure 4. The sharp reduction in sonic velocity near the cavity can be attributed to the increase in porosity, also measured by Short, which reduces the bulk modulus, and thus the sound speed. At greater ranges, the decreased sonic velocity is due to the reduction in shear strength. In this region the porosity and bulk modulus are nearly constant.

The importance of the variation in longitudinal velocity is in the propagation of the rarefaction waves. In turn, these waves are responsible for the transition zone of the wave forms. Since the rarefaction waves travel more slowly through shock-conditioned rock, the stress attenuation time is greater, resulting in a broader wave profile.

The region of shock damage and thus material property alteration extends to ranges of two to three times the final cavity radius. For PILE DRIVER, the stations where the most significant data was gathered (at ranges of 688 and 1543 ft) were well beyond the aforementioned region. Thus the assignment of average or effective properties to the entire field for predictive purposes appears to be unjustified. The results of small-scale explosive experiments, wherein the entire region of interest is within the strongly shocked region, can thus be misleading, since the tendency has been to assign the properties of a large granite field on the basis of the small-scale experiment, whereas, in reality, the free-field of interest encompasses both strongly shocked and weakly shocked regions of rock.

### 1-3. PROPERTIES AND MODELING OF NTS GRANITE

The PILE DRIVER event was fired in that portion of Area 15 of the Nevada Test Site where the general geological setting is that of Climax granitic stock. The shot point and the ground motion instrumentation stations were located at a depth of approximately 1500 ft, indicating an overburden pressure of about 110 bars. The granite field was composed

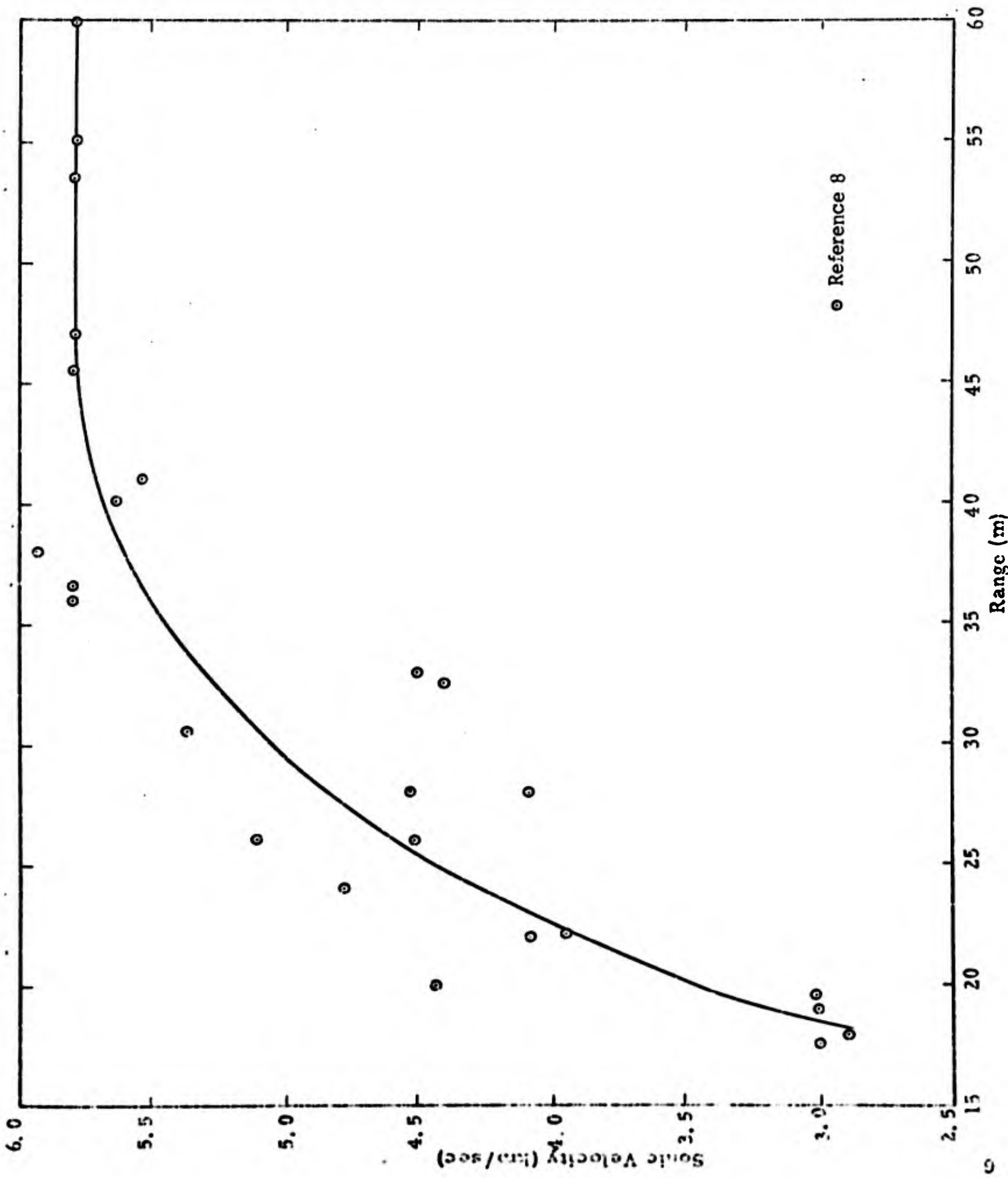


Figure 4. Post-Shot Sonic Velocity vs Range (HARD HAT)

of a granodiorite intrusive mass around the shot point in contact with a quartz monzonite intrusive mass approximately 500 ft from the shot point along the line between the shot point and the instrumentation stations. The properties of both types of granitic rocks, granodiorite and quartz monzonite, appear to be similar in most respects important to ground motion studies.

### I-3.1 PRE-SHOT PROPERTIES

The in-situ granite was assigned the following properties as being representative of its nominal state before the event:

Density:	$\rho_0 = 2.69 \text{ gm/cm}^3$
Dilatational Velocity:	$v_{d0} = .579 \text{ cm}/\mu\text{sec}$
Shear Velocity	$v_{s0} = .330 \text{ cm}/\mu\text{sec}$

The value for the density was selected from data from core samples, given in References 7, 11, 12, and 13. The elastic velocities were estimated from test data reported in References 7, 11, 12, and 14. The above values imply the following other properties:

Bulk Modulus:	$K_0 = .512 \text{ Mb}$
Shear Modulus:	$G_0 = .293 \text{ Mb}$
Poisson's Ratio	$\nu_0 = .26$

The value for Poisson's ratio is in good agreement with that reported in References 15 and 16. The subscript  $_0$  indicates that these are pre-shot, ambient-pressure values.

The variation of compressibility with pressure is accounted for in the equation of state relations. For this study, the shear modulus was not assumed to be a function of the instantaneous pressure (although variation is allowed to occur as a result of the shock passage).

### I-3.2 EQUATION OF STATE

The equation of state used for the granite medium was similar to that used in a previous program, as described in Reference 6. Some improvements were made to this formulation, specifically, to the low-pressure hydrostat and in the vapor regime.

The revised state equations are:

REGION I (Solid Phase):  $\mu e - \mu_v e_v \geq 0$

The pressure in the solid phase is given by

$$P = F(\rho) + [a + S(\rho, e)] \rho e$$

where

$$F(\rho) = [A - (A - K_0) e^{-k\mu}] \mu - B\mu^2 e^{-h\mu^6}, \quad \mu > 0$$

$$F(\rho) = K_0 \mu, \quad \mu \leq 0$$

$$S(\rho, e) = \frac{b}{\frac{e}{e_0} \eta^2 + 1}$$

REGION II (Fluid Phase):  $\mu e - \mu_v e_v < 0$

The pressure in the fluid phase is given by

$$P = a \rho (e - e_s) + \left\{ [a e_s + S(\rho, e) e] \rho + F(\rho, e) e^{\beta R(\rho, e)} \right\} e^{R(\rho, e)}$$

where

$$R(\rho, e) = \frac{-\alpha (\mu e - \mu_v e_v)^2}{\eta e^2}$$

The symbols in the above equations are defined as:

$e$  = specific internal energy,

$P$  = pressure,

$\eta = \rho/\rho_0$  relative density

$\mu = \eta - 1$  compression

$\rho$  = density

The values of the coefficients in the above equations are:

$a = .5$	$A = .611 \text{ (Mb)}$
$b = 1.6$	$B = .7 \text{ (Mb)}$
$e_o = .063 (10^{12} \text{ ergs/gm})$	$K_o = .512 \text{ (Mb)}$
$e_s = .18 (10^{12} \text{ ergs/gm})$	$\alpha = 5.$
$e_v = .035 (10^{12} \text{ ergs/gm})$	$\beta = 5.$
$h = 1.54$	$\mu_v = -.2$
$k = 50.$	$\rho_o = 2.69 \text{ (gm/cm}^3\text{)}$

The first term of the hydrostat,  $F(\mu)$ , was modified in the low-pressure regime to effectively change the bulk modulus from a constant,  $A$ , to a variable which increases smoothly from  $K_o$  at zero pressure up to  $A$ , which is representative of higher pressures. A comparison of this hydrostat with experimental compressibility data<sup>17-19</sup> is shown in Figure 5. The previously obtained<sup>6</sup> good fit to the shock Hugoniot data is unaffected by this modification.

The foregoing equations have been formulated to provide continuity of the pressure and the sound speed throughout, including transitions across the phase line separating Regions I and II. Also, the proper ideal gas behavior, given by  $P = a \rho (e - e_s)$ , is asymptotically approached for large volumes.  $e_s$  is the sublimation energy; the factor  $(e - e_s)$  is necessary since in this model the energy of the normal material state,  $V = V_o$  and  $P \approx 0$ , was chosen to be zero ( $e_o = 0$ ).

The equation of state was also modified from that used previously to give a higher, more realistic value for  $V_{cv}$  (the volume at one atmosphere corresponding to complete vaporization), equal to  $\sim 2000 \text{ cm}^3/\text{gm}$ , as estimated from comparisons with other substances. Using the above ideal gas relationship, the energy corresponding to complete vaporization at one atmosphere ( $e_{cv}$ ) can be approximated as  $1.84 \times 10^{11} \text{ ergs/gm}$ .

### I-3.3 PROPERTIES OF SHOCKED NTS GRANITE

As discussed in Section 2.3, the properties of the granite may be altered by the explosion-induced shock. For use in the computational model, a convenient and physically meaningful parameter which can be used to characterize the shock wave is the peak shock pressure. Various

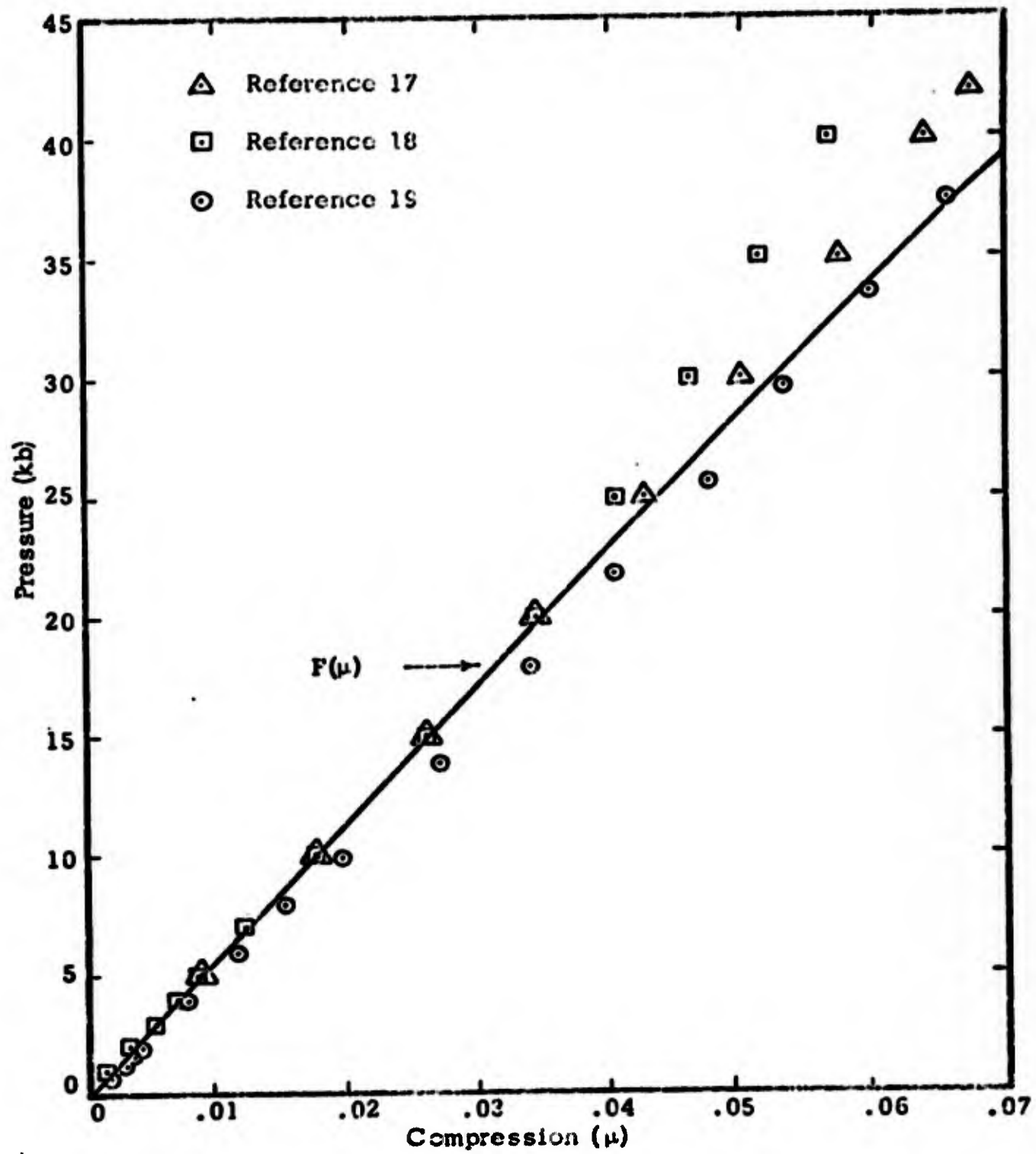


Figure 5. Low-Pressure Hydrostat for Granite

post-shot properties, including bulk density, porosity, sonic velocity, and crushing strength, of core samples taken from the HARD HAT site were examined by Short<sup>8</sup> and the data were correlated with the peak shock pressure experienced by the sample during the event. The variation of properties as a function of distance along a post-shot drill hole is shown in Figure 6, reproduced from Reference 8.

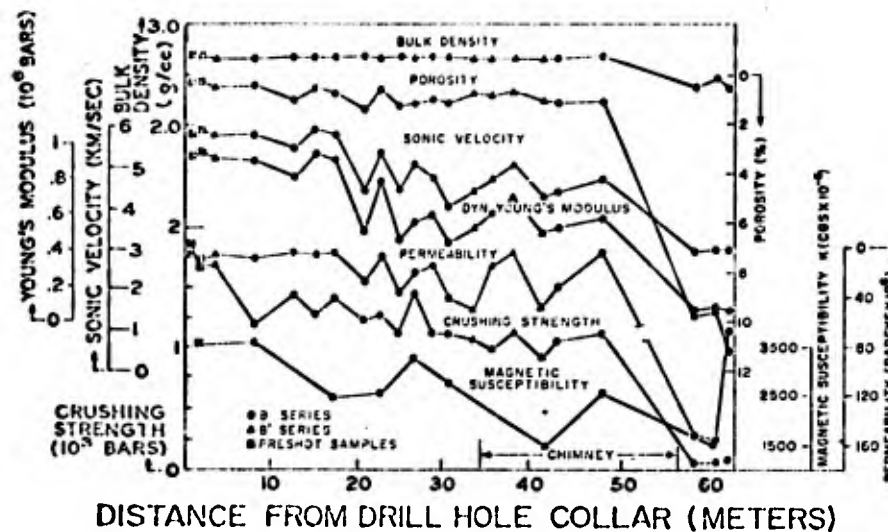


Figure 6. Variation of Properties with Distance Along Post-Shot Drill Hole (HARD HAT) (Reproduced from Reference 8)

Using the latter distance, we can calculate the distance of a sample from the shot point, and then the estimated peak pressure, except for those samples that were found in the chimney, since the rubble in the chimney originated from unknown positions. Excluding then the samples from the chimney, the property data were correlated with the peak shock pressure; the results, for the bulk density and the dilatational velocity, are shown in Figure 7. This correlation indicates that below some minimum peak shock pressure, which we will term  $P_0$ , and which is about 8 kb, there are no significant changes in the properties brought about by the shock wave; the properties in this range are assumed to remain equal to the pre-shot values, as listed in Section 3.1. Between  $P_0$  and  $P_1 = 32$  kb, the dilatational velocity decreases and the density remains nearly unchanged. Between  $P_1$  and  $P_2 = 43$  kb, all the properties were affected. For peak pressures above  $P_2$ , the evidence suggests that the fracture was severe enough to assume that the shear strength was zero and thus that a hydrodynamic model could be employed.

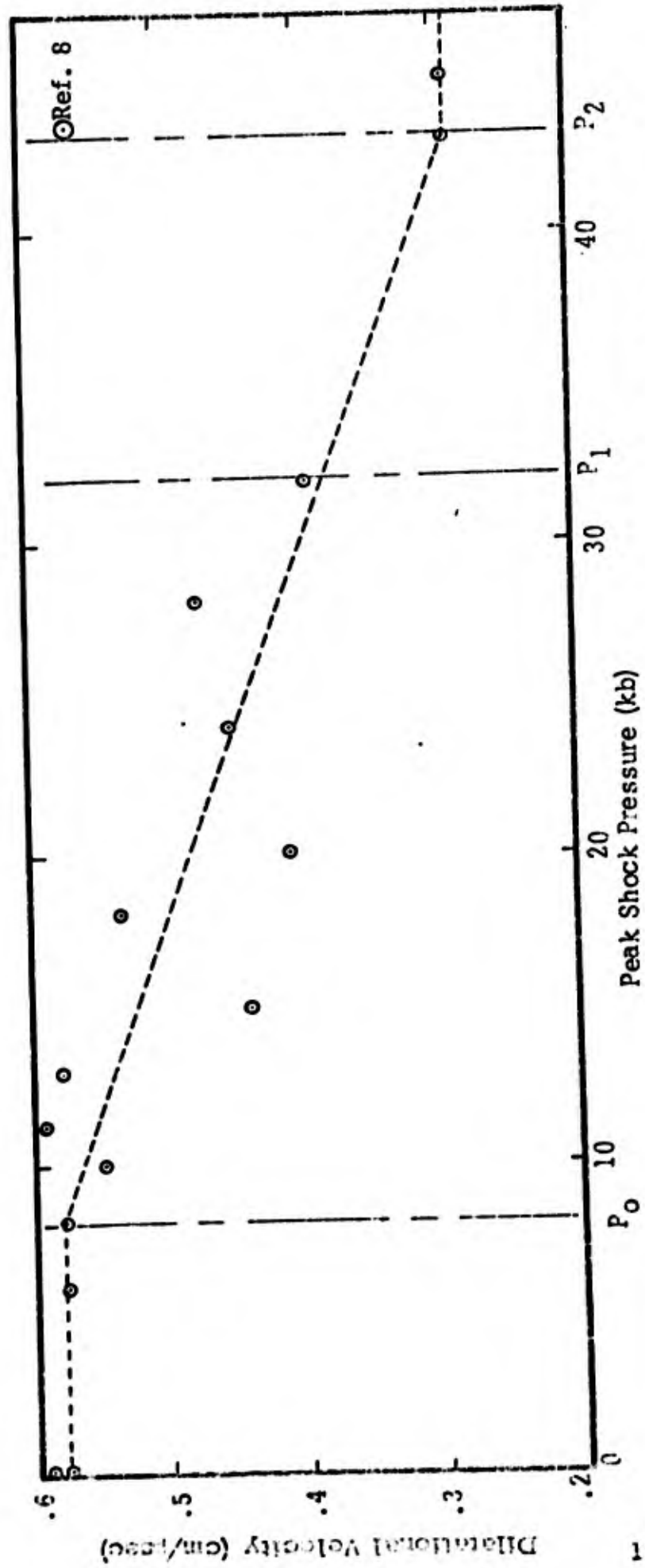
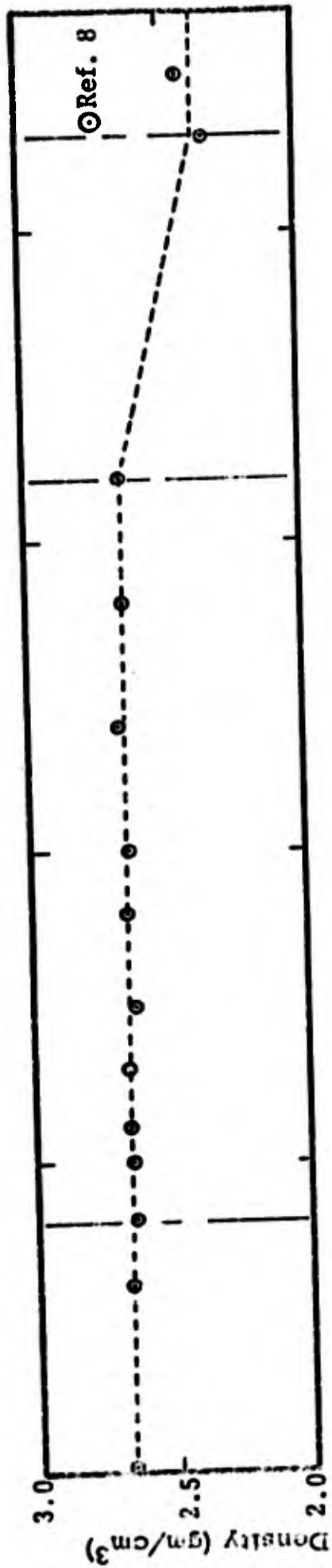


Figure 7. Density and Dilatational Velocity vs Peak Shock Pressure for Granite

From the density and dilatational velocity data, the elastic properties of the shocked granite were derived, as functions of the peak shock pressure ( $P_p$ ), as follows. The following piece-wise linear fits were assumed for the density and dilatational velocities, as indicated by the dashed lines in Figure 7.

$$\begin{cases} \rho = \rho_0 & P_p \leq P_1 \\ \rho = \rho_2 + \frac{P_p - P_2}{P_1 - P_2} (\rho_0 - \rho_2) & P_1 < P_p < P_2 \\ \rho = \rho_2 & P_p \geq P_2 \end{cases}$$

$$\begin{cases} v_d = v_{d0} & P_p \leq P_0 \\ v_d = v_{d2} + \frac{P_p - P_2}{P_0 - P_2} (v_{d0} - v_{d2}) & P_0 < P_p < P_2 \\ v_d = v_{d2} & P_p \geq P_2 \end{cases}$$

where

$$\begin{aligned} v_{d0} &= .579 \text{ cm}/\mu\text{sec} & P_2 &= .043 \text{ Mb} \\ v_{d2} &= .29 \text{ cm}/\mu\text{sec} & \rho_0 &= 2.69 \text{ gm}/\text{cm}^3 \\ P_0 &= .008 \text{ Mb} & \rho_2 &= 2.38 \text{ gm}/\text{cm}^3 \\ P_1 &= .032 \text{ Mb} \end{aligned}$$

The density referred to above is, of course, the residual or release density of the sample, not that experienced under shock compression.

To determine the other elastic properties, the variation of another parameter, such as the shear velocity, is needed. Since no data were available, a linear function for the shear velocity was assumed, similar to the form used for the dilatational velocity, as follows:

$$\left\{ \begin{array}{l} v_s = v_{so} \\ v_s = \frac{P_p - P_2}{P_1 - P_2} (v_{so}) \\ v_s = 0 \end{array} \right. \quad \begin{array}{l} P_p \leq P_0 \\ P_0 < P_p < P_2 \\ P \geq P_2 \end{array}$$

Choosing the shear velocity, as opposed to Poisson's ratio or one of the moduli, provided the most likely and self-consistent behavior of the various properties in view of the available data. Functions for the bulk modulus, shear modulus, and Poisson's ratio were then readily derivable. Curves of shear velocity and the latter variables versus peak shock pressure are shown in Figures 8 and 9.

The in-situ yield strength was assumed to equal  $Y_0$  for  $P_p \leq P_0$ , to decrease linearly from  $Y_0$  to zero between  $P_0$  and  $P_2$ , and to equal zero for  $P_p > P_2$ . This behavior is similar to that observed for the crushing strength of core samples, as reported by Short.<sup>8</sup>

#### I-3.4 SHOCK CONDITIONING MODEL

A model incorporating the properties and behavior of NTS granite, before and after shocking, as described above (Sections 3.1, 3.2, and 3.3), was formulated and incorporated into the one-dimensional SHEP code.

At the outset of a numerical solution, each cell is assigned the normal, or pre-shot, properties. The appropriate shock-conditioned properties are then assigned to a cell following passage of the peak of the shock wave, depending upon the value of peak stress reached in each cell.

Provisions for relaxing the properties over a characteristic period of time, rather than in one time step, were also coded, but it was subsequently found that this made little difference in the results.

For the constitutive model used in SHEP, the parameters specifically modified, due to shock effects, were the shear modulus, the hydrostat, and the yield strength. The shock-conditioned hydrostat, contained in the equation of state, was modified to match the release density and bulk modulus of samples that had been shocked to various stress levels. For material elements that were shocked to less than

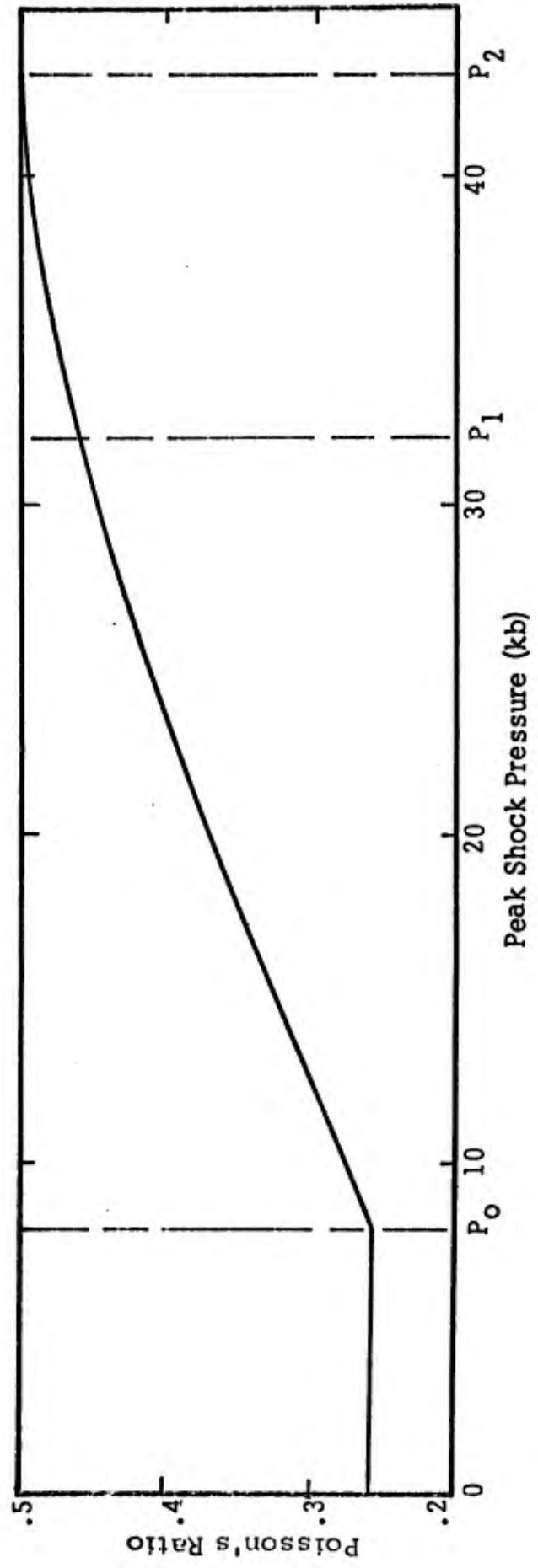
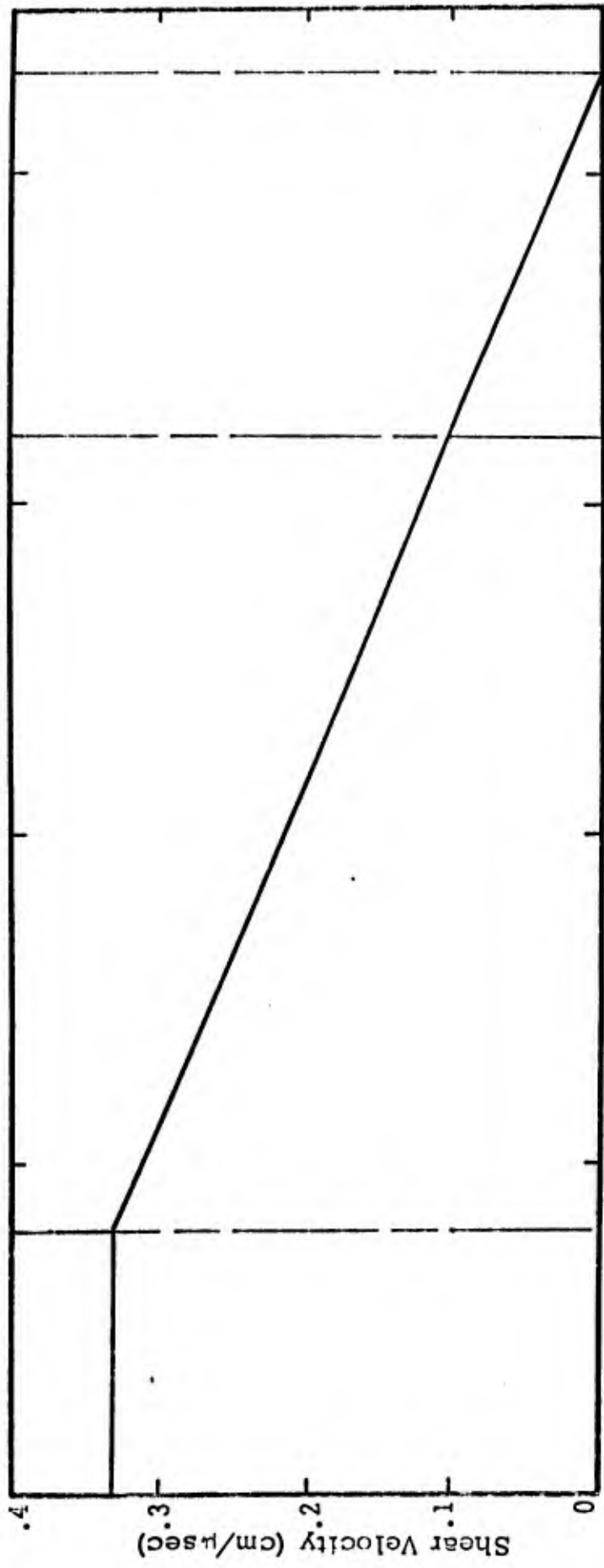


Figure 8. Shear Velocity and Poisson's Ratio vs Peak Shock Pressure for Granite

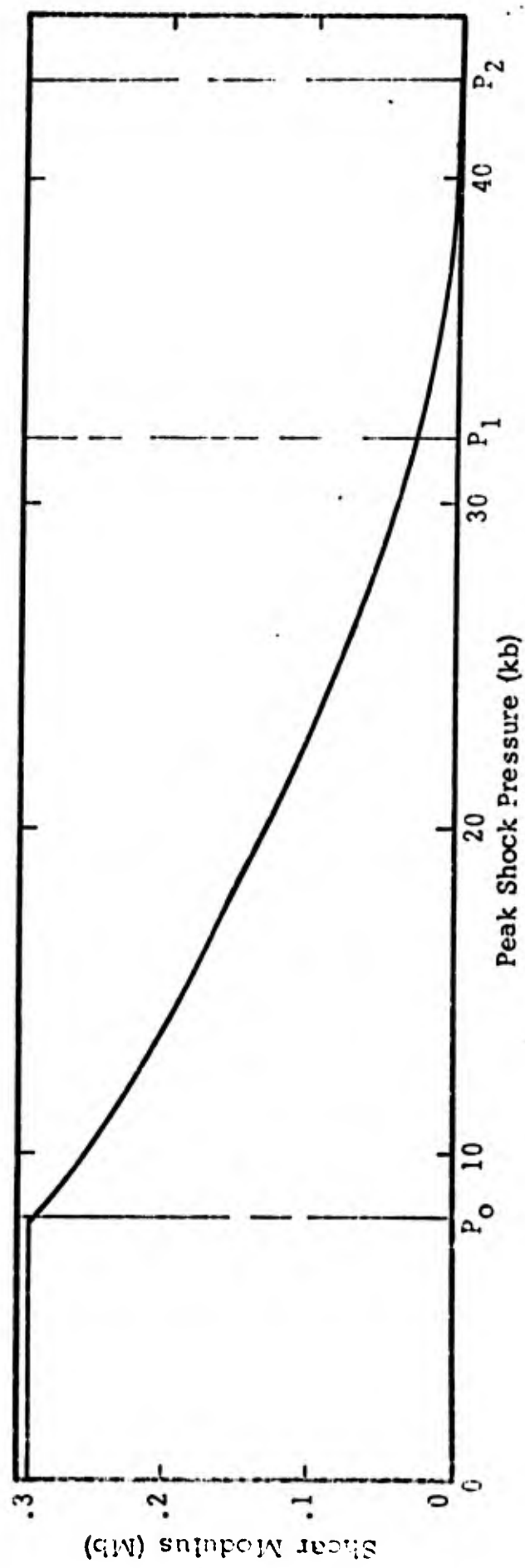
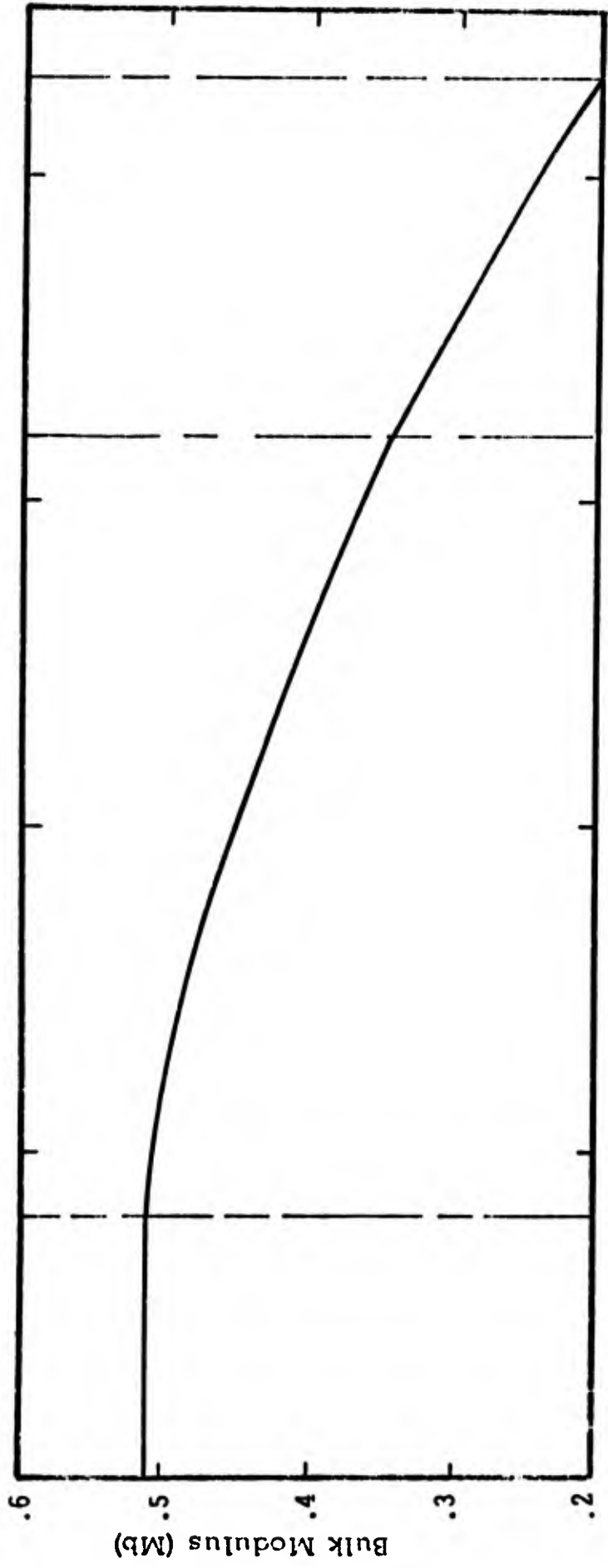


Figure 9. Bulk and Shear Moduli vs Peak Shock Pressure for Granite

8 kb ( $P_p < P_o$ ), no change was made in the hydrostat. For zones experiencing greater peak shock pressures ( $P_p > P_o$ ), the hydrostat was modified to reflect an unloading path having a slope and position upon pressure release in accordance with the residual bulk modulus and density appropriate to the original shock level. The form of the shock-conditioned hydrostat employed was:

$$P = \frac{P_s^2 - P_s [P_s^2 - 4K_s(\mu - \mu_s)(\mu_s K_s + P_s)]^{\frac{1}{2}}}{2(\mu_s K_s + P_s)} \quad \mu > \mu_s$$

$$P = K_s(\mu - \mu_s) \quad \mu \leq \mu_s$$

up to pressures where it merged with the pre-shot, or stiff, hydrostat. The hydrostat was unchanged for pressures above the merge point. In the above equations  $\mu_s(P_p)$  is the compression corresponding to the release density appropriate to the peak shock level ( $\mu_s$  varies between 0 and  $-.115$ ),  $K_s(P_p)$  is the bulk modulus, upon release, varying with increasing shock pressures from  $.512$  to  $.2$ , and  $P_s$  is a constant, equal to  $.5$  kb. The value of  $P_s$ , the hydrostatic pressure at  $\mu = 0$  on the unloading path, sets the point of transition (which is at a slightly higher pressure than  $P_s$ ) between the regular and shock-conditioned hydrostats.

Since no data on the actual release paths were available, the functional form selected was arbitrary; however, as noted above, the starting slope and position are based on the experimental data, and the constant  $P_s$  was selected to give unloading paths which are thermodynamically consistent (e.g., higher values of  $P_s$  result in energy releases greater than the available energy in the initially shocked state). Isentropic release paths from shocked states of 30, 35, 39, and 50 kb, reflecting this change to the equation of state, are shown in Figure 10. The constant  $\mu_v$  in the equation of state (the incipient vaporization point), must also be changed, to  $-.418$ , because of this modification. The value of  $\mu_v$  is determined by solving for the compression in the equation of state for  $e = e_v$ , the incipient vaporization energy, and zero pressure.

#### 1-4. NUMERICAL SOLUTIONS

##### 1-4.1 PROBLEM DESCRIPTION

A series of code solutions of the PILE DRIVER ground motions was performed to evaluate the shock-conditioning effects. All of the solutions were one-dimensional calculations in spherical geometry.

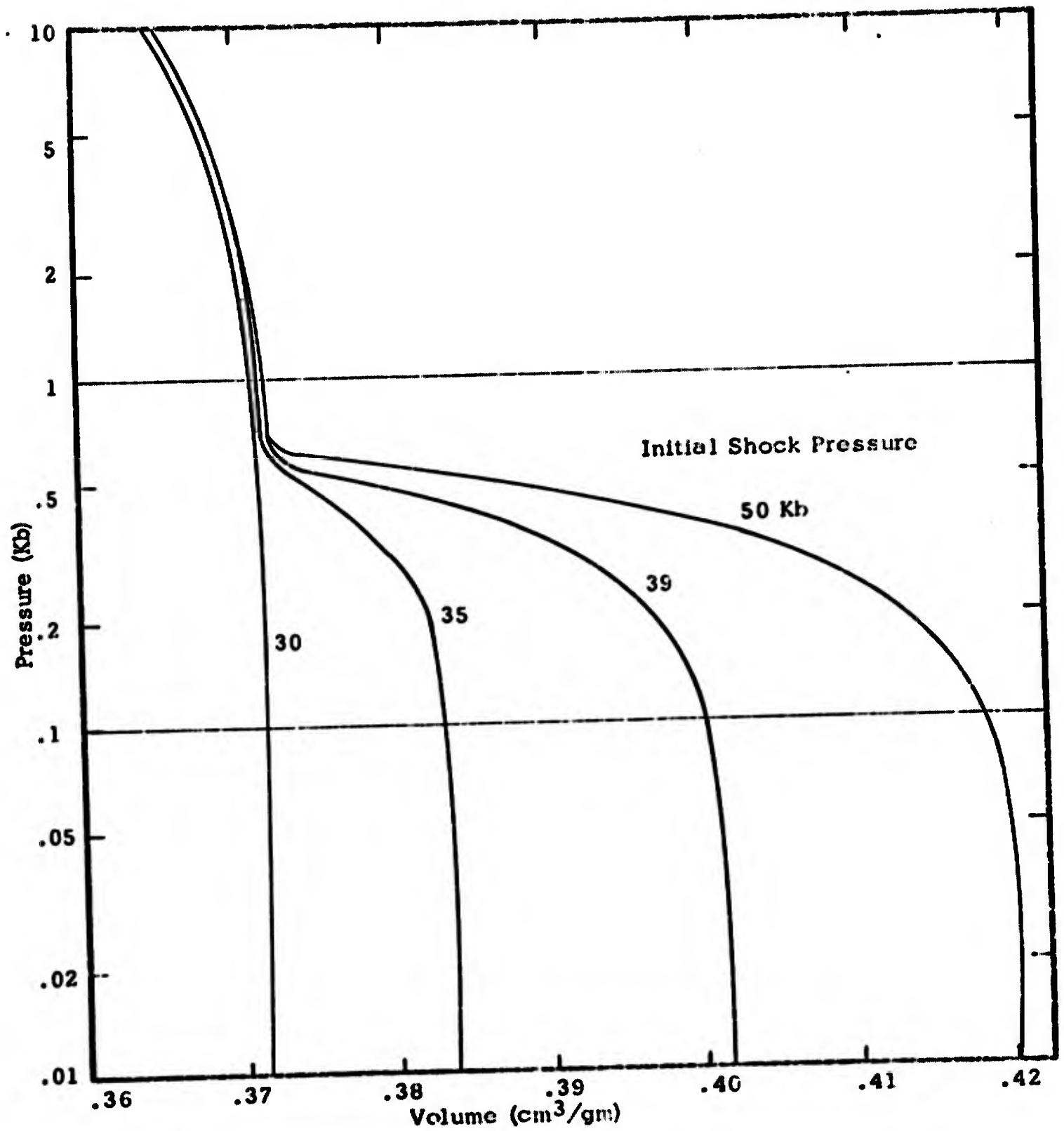


Figure 10. Release Isentropes for Shock-Conditioned Granite

The solutions were obtained with the SHEP code, a finite-difference Lagrangian program employing a hydrodynamic-elastic-plastic behavioral model. Options for various yield criteria are available. Within the chosen yield surface, the deformations are considered to be elastic. Excursions on the yield surface are made in accordance with the Prandtl-Reuss flow rule. A description of the code may be found in Reference 20.

For these solutions, the von Mises yield criterion was employed:

$$\sqrt{3J_2^*} \geq Y_0$$

where  $J_2^*$  is the second invariant of the deviatoric stress tensor and  $Y_0$  is the yield strength under uniaxial loading. A more complex failure surface was not employed, since an acceptable model for failure of the in-situ rock has not yet been established and since the primary objective of the solutions was confined to an assessment, or isolation, of the effects of shock conditioning on the free-field response. A value of .5 kb for the yield strength was selected for these solutions. This value is representative, but has no direct experimental basis; a somewhat higher value than that previously estimated<sup>6</sup> to give best agreement with the final results (.25 kb) was chosen, in view of the hypothesized effects of shock conditioning on the free-field response. Deviatoric stresses were permitted only in the solid phase of the material. In all of the solutions, no hydrostatic tension was allowed. I.e., if the pressure of an element as prescribed by the equation of state function has a negative value, this value is replaced by zero in the computations for the stress components. If the material element subsequently adiabatically expands, its path in the P-V plane will be along the zero pressure axis.

A polytropic gas source model was used in the solutions, as was previously employed.<sup>6</sup> The pre-shot cavity radius was assumed to be 1.25 meters.<sup>6</sup>

The Lagrangian grid for these solutions was zoned as follows:

For the first 25 meters beyond the cavity wall, a zone size of 50 cm was used. The zone sizes were then geometrically increased by 5% until the zone size was 200 cm, which corresponded to a range of 59 meters. Between 59 and 600 meters a constant zone size of 200 cm was used. Beyond 600 meters (and the range of interest), the zone size

was again increased by 5%, out to a range of 2500 meters, where the grid was terminated. A total of 431 grid points were employed. Portions of the grid were rezoned from time to time during the course of the solution to eliminate relatively small zone widths, which develop at close-in ranges as the cavity expands.

Comparative code solutions of PILE DRIVER were run, with and without the shock-conditioning model; in addition, a solution which included all aspects of the shock-conditioning model except for the modified equation of state (Section 3.2), which provides reduced residual densities of shocked granite, was run, to show what effects this bulking has on the free-field results.

Field test data of the velocity and displacement time histories were available at ranges of 668 and 1543 ft.<sup>7</sup> Accordingly, detailed output data were obtained at these stations to permit comparison of the code results with the observed motions. Another important experimental measurement was the post-shot cavity radius, reported to be 44.5 meters.<sup>21</sup>

## **1-4.2 SOLUTION RESULTS**

### **1-4.2.1 Case Without Shock-Conditioning Model**

This case, which did not employ the shock-conditioning model, was run to provide a basis for comparison and evaluation of the runs which did include the new model. The computed wave profile (velocity vs time) at a range of 668 ft is shown in Figure 11, along with the corresponding test results. The time history of the displacement obtained for this range is shown in Figure 12. The velocity and displacement time histories at a range of 1543 ft are shown in Figures 13 and 14. The cavity radius at the end of the solution (.395 sec), as estimated from the position of the gas/solid interface in the granite, was 47 meters.

### **1-4.2.2 Case With Shock-Conditioning Model**

Repeating the run with the shock-conditioning model included produced the waveforms for the near station shown in Figures 15 and 16. The far station results are shown in Figures 17 and 18. The estimated cavity radius at .43 sec was 48 meters and decreasing slowly.

Comparing the results for the two cases, significant improvements in all the waveforms are seen to be achieved with the shock conditioning model. E.g., at a range of 668 ft, the peak displacement

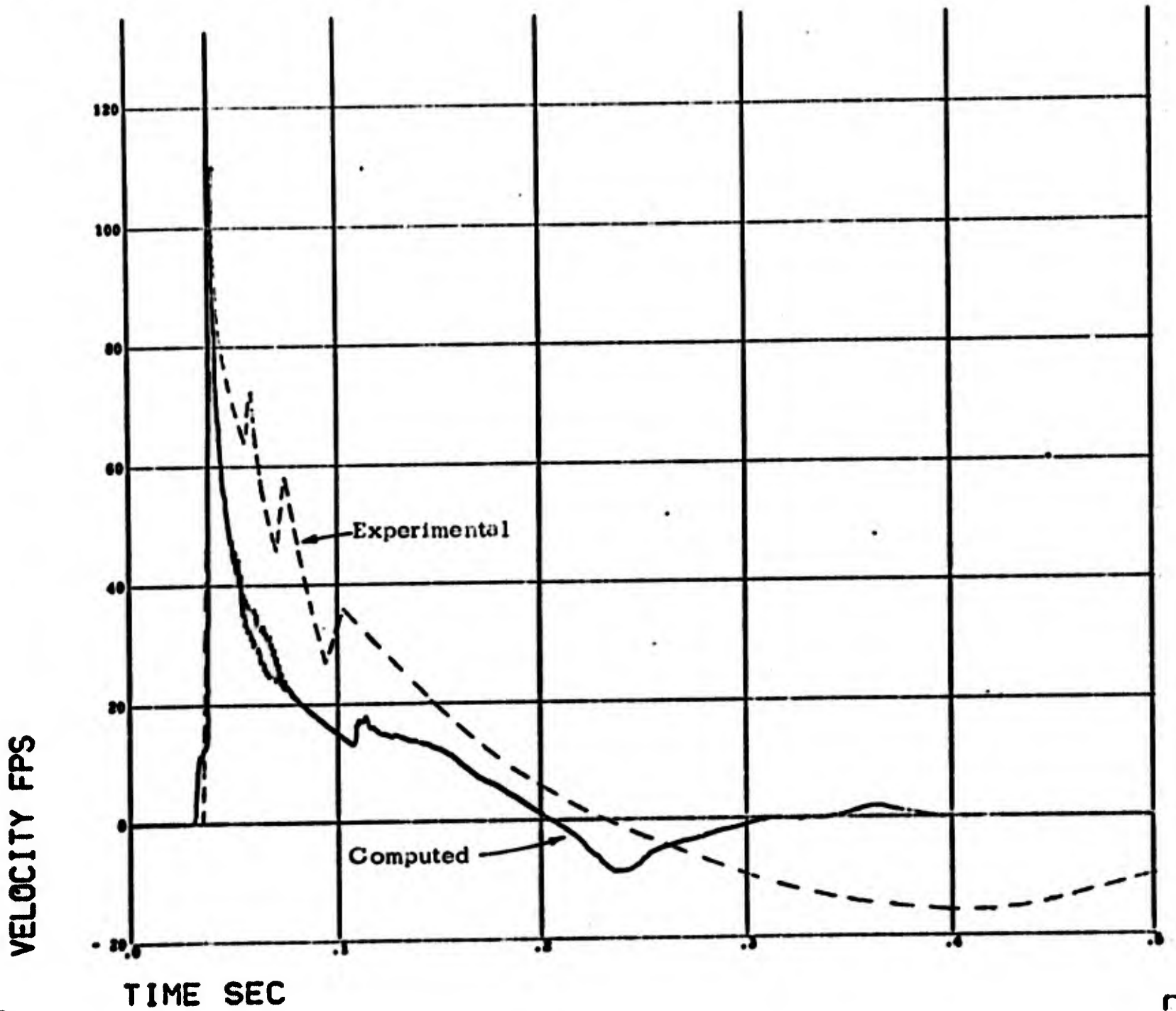


Figure 11. Radial Velocity vs Time, Range = 658 ft, Case Without Shock-Conditioning Model

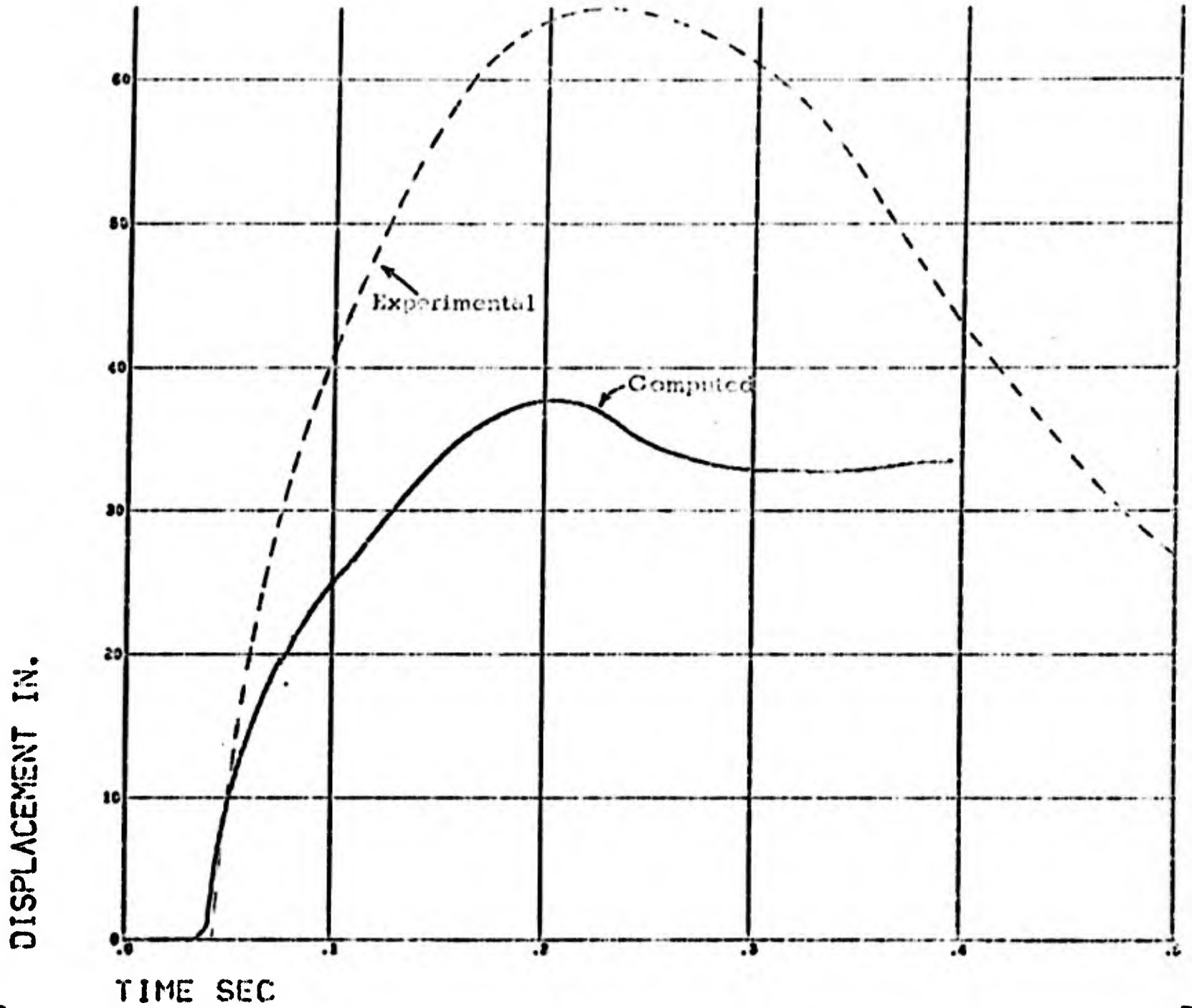


Figure 12. Radial Displacement vs Time, Range = 668 ft, Case Without Shock-Conditioning Model

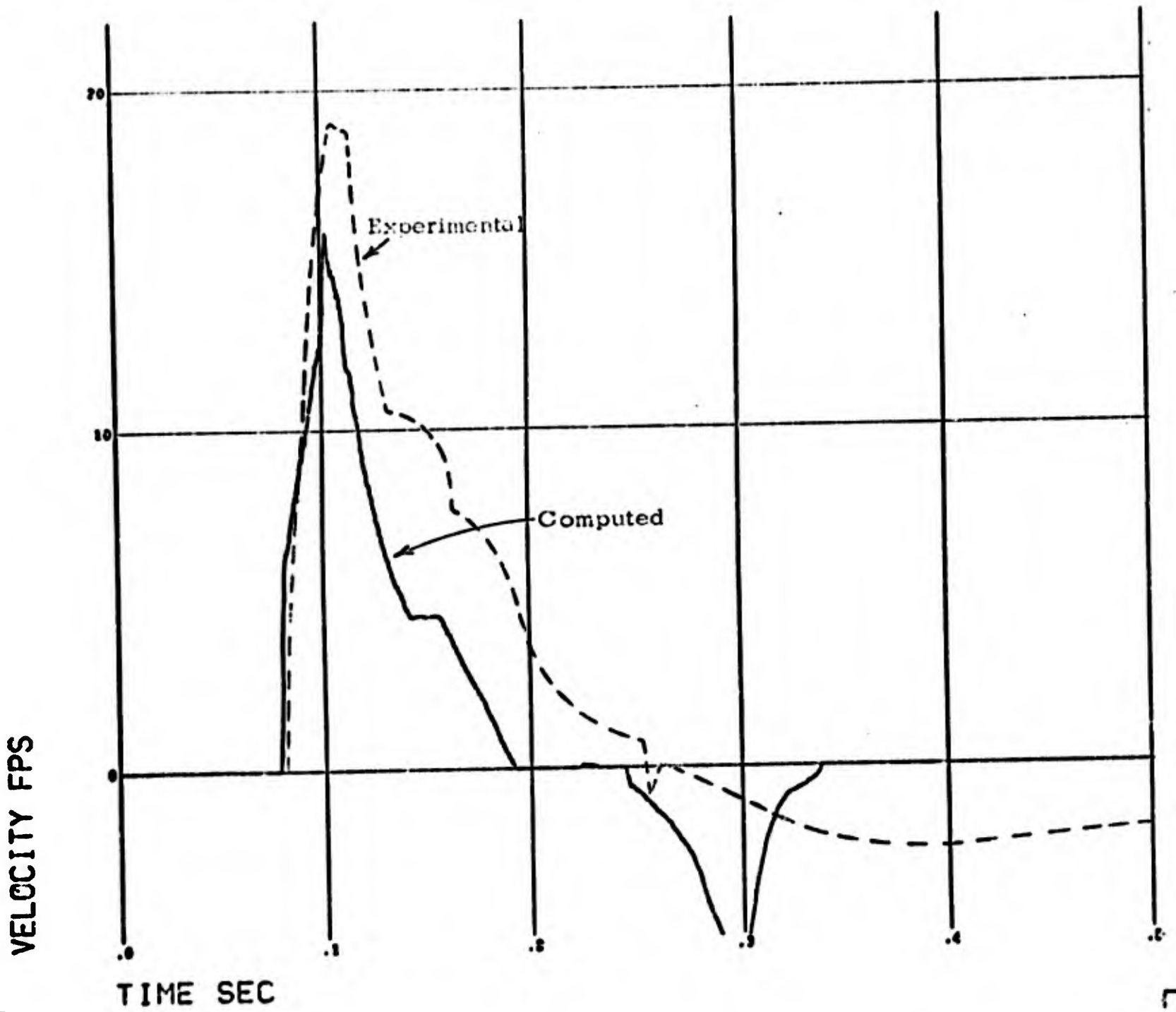


Figure 13. Radial Velocity vs Time, Range = 1543 ft, Case Without Shock-Conditioning Model

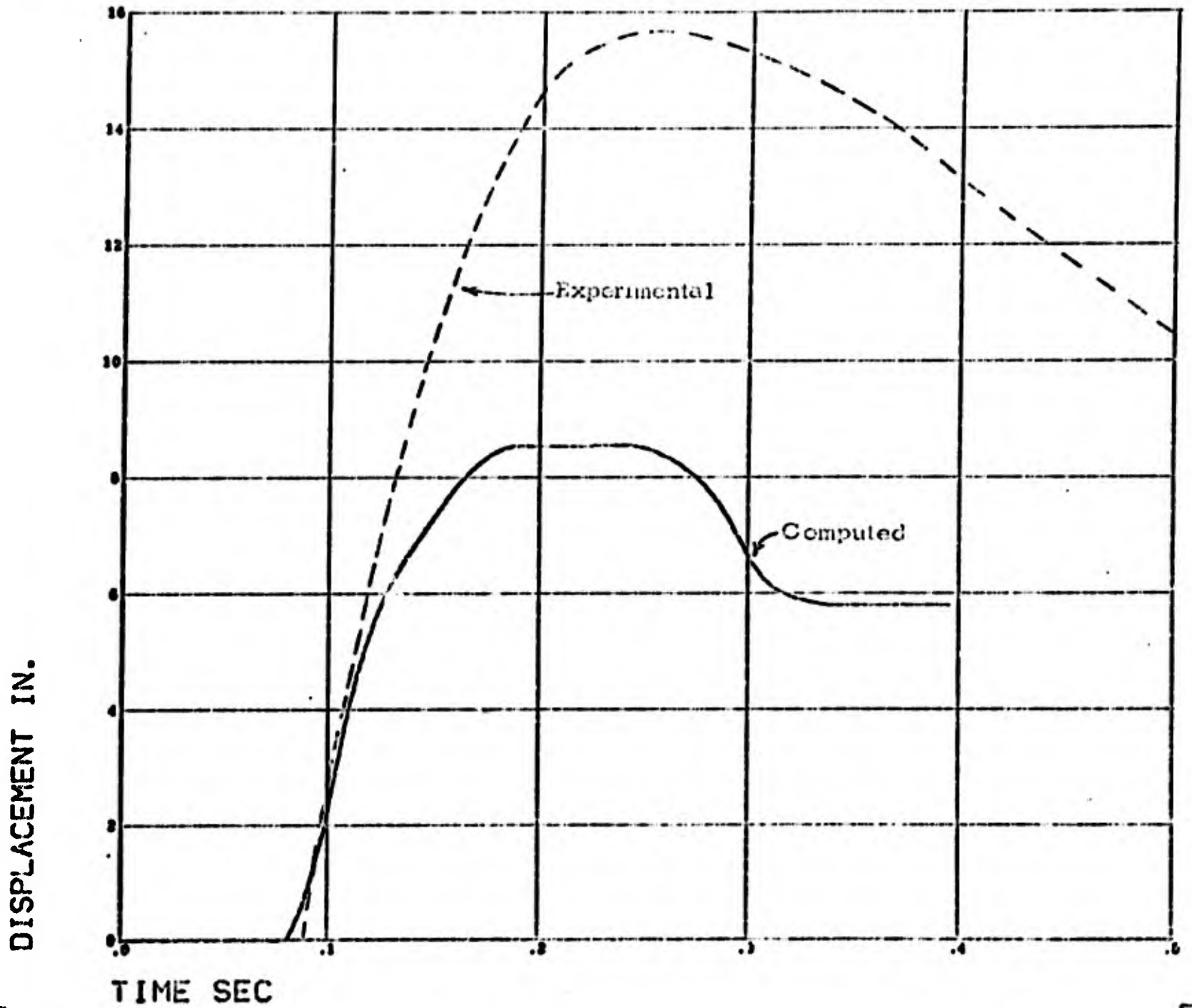


Figure 14. Radial Displacement vs Time, Range = 1543 ft, Case Without Shock-Conditioning Model

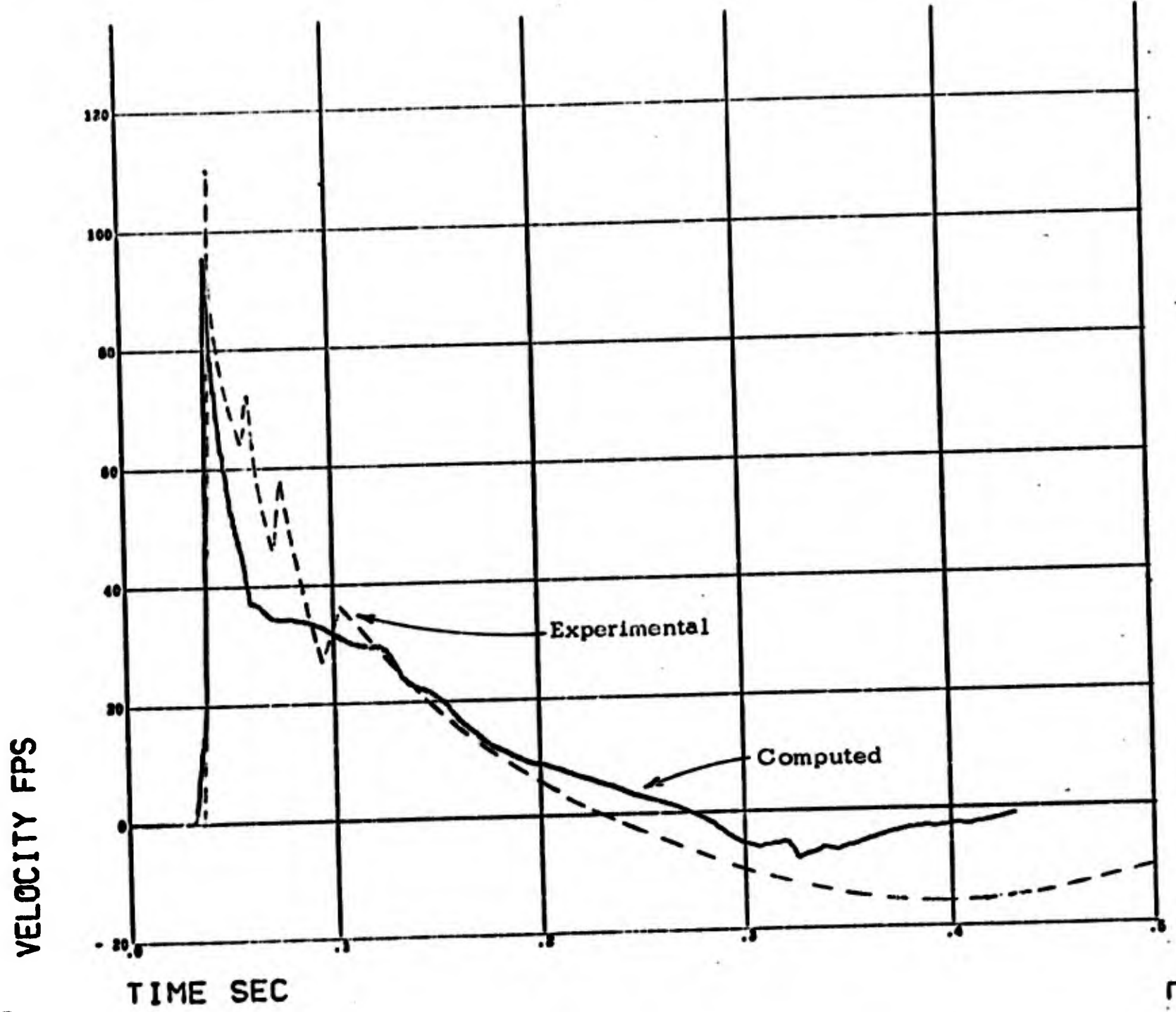


Figure 15. Radial Velocity vs Time, Range = 668 ft, Case With Shock-Conditioning Model

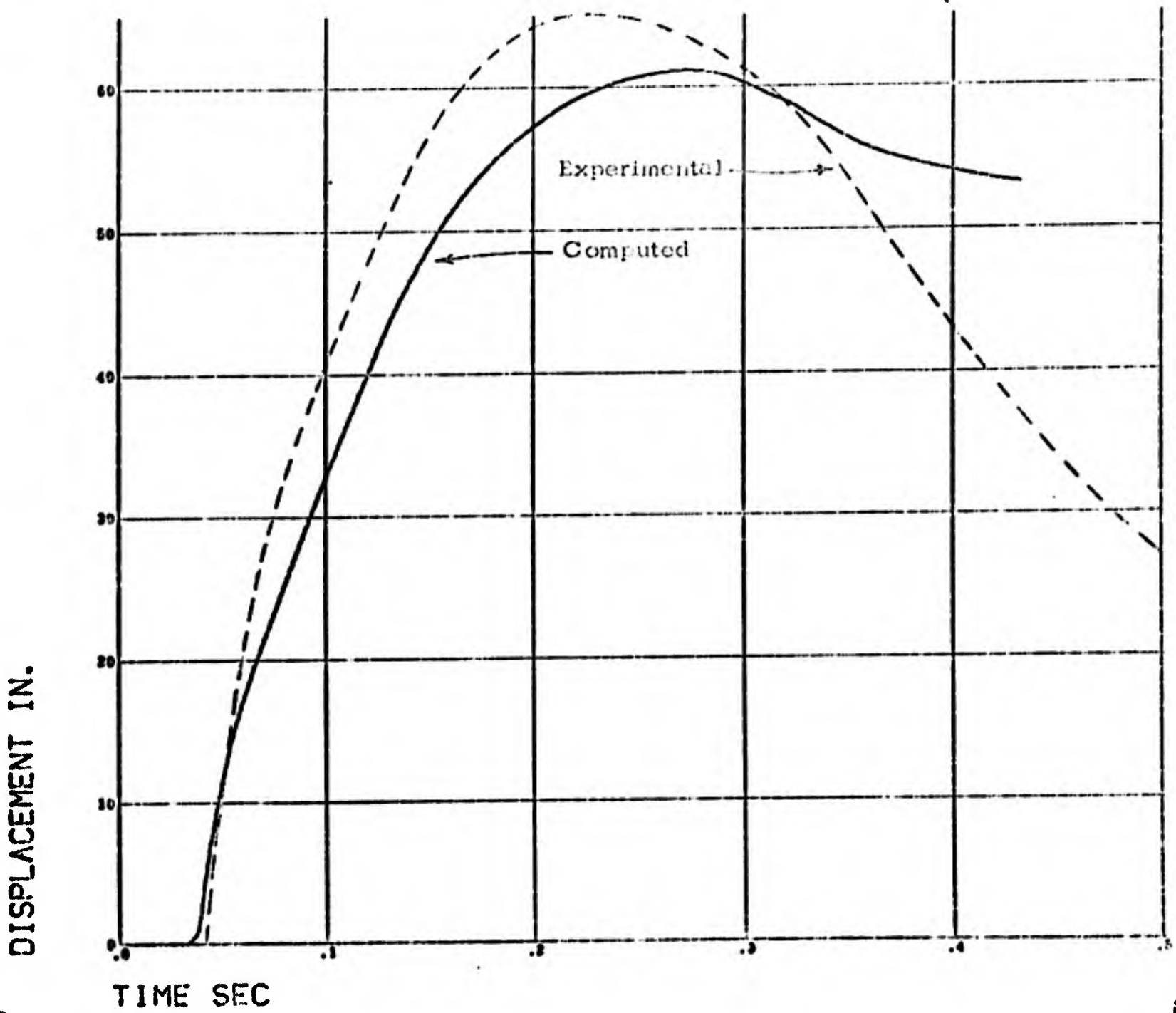


Figure 16. Radial Displacement vs Time, Range = 668 ft, Case With Shock-Conditioning Model

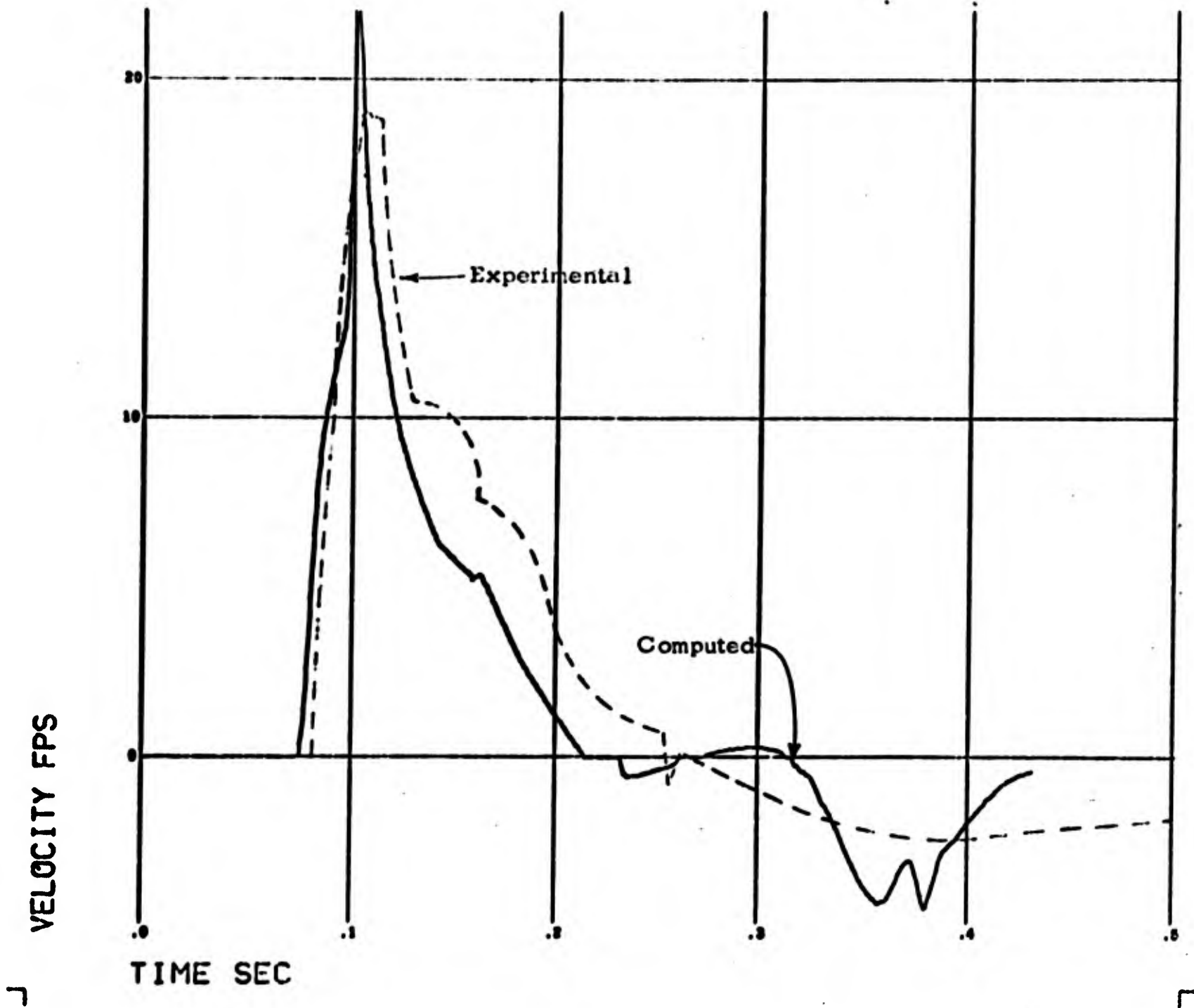


Figure 17. Radial Velocity vs Time, Range = 1543 ft, Case With Shock-Conditioning Model

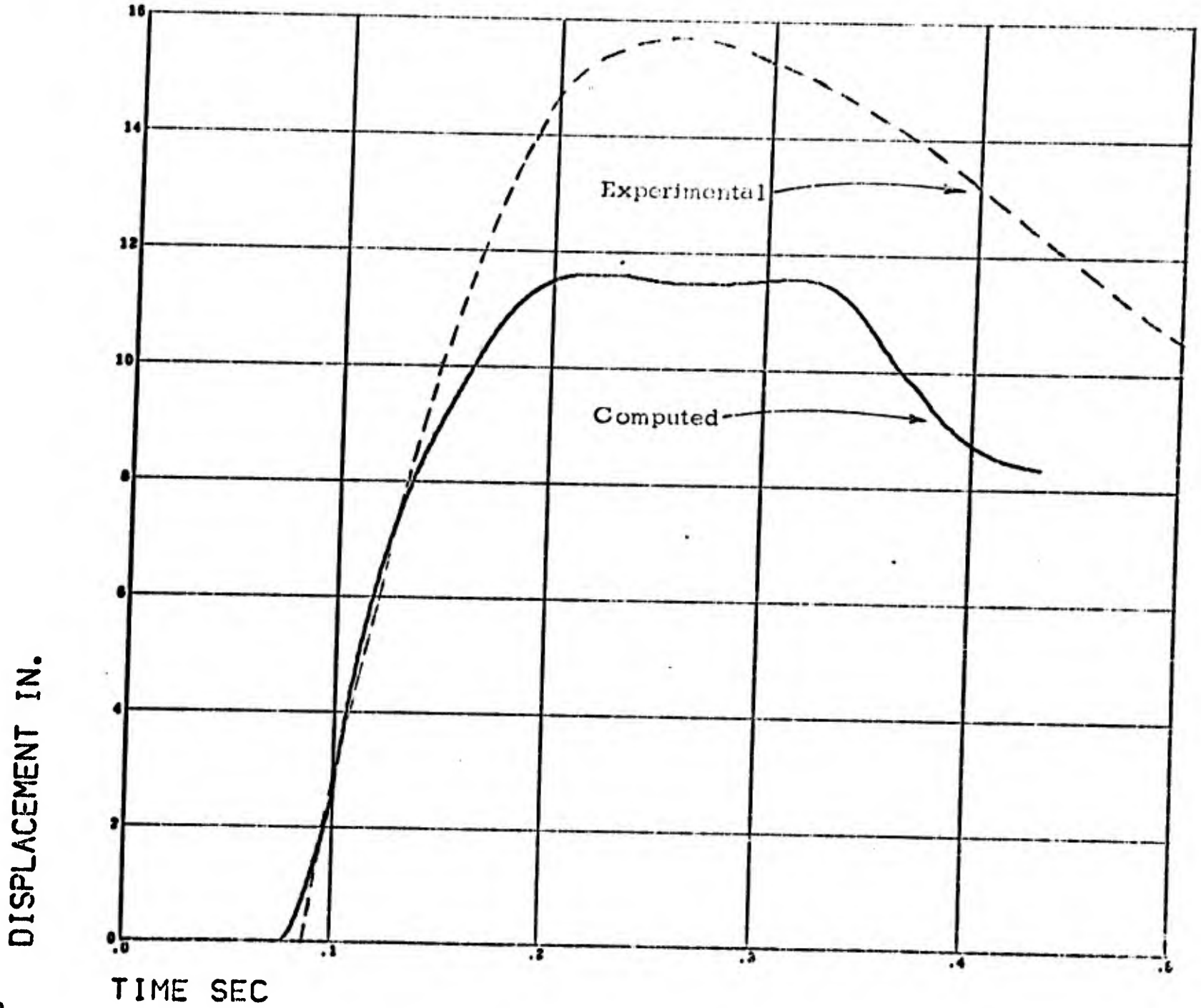


Figure 18. Radial Displacement vs Time, Range = 1543 ft, Case With Shock-Conditioning Model

was increased from 38 to 61 in., and from 8.6 to 11.6 in. at a range of 1543 ft. Such a high peak displacement may also be achieved, of course, by lowering the strength of material; however, when this is done, there is little or no recovery phase. With the strength chosen here ( $Y_0 = .5 \text{ kb}$ ), the recovery phase is still too shallow, however. Examination of the waveforms indicates that the transition phase is only slightly broadened through the shock-conditioning effects; if the observed slow decay was correctly predicted, then a larger displacement would accumulate, and therefore a higher strength could be assigned to achieve the desired recovery. It has been suggested that the occurrence of dilatancy or bulking in the granite would tend to broaden the waveform, due to the associated reduced rarefaction wave speeds. A model combining dilatant and shock conditioning effects would in that case predict most of the major characteristics of the observed wave profiles.

#### **I-4.2.3 Case Without Bulking**

To isolate the effects due to bulking, as provided by use of the shock-conditioned hydrostat, the previous solution (Section 4.2.3) was run without bulking, but including all other aspects of the shock conditioning model. The resultant waveforms, at a range of 668 ft, are shown in Figures 19 and 20. With the bulking, the decay in the velocity profile is initially the same, but then broadens after further relief (below 40 fps). The resulting peak displacement increased from 48.5 (without bulking) to 61.2 inches (with bulking) at a range of 668 ft. The broadening occurs late since the hydrostat is not substantially different until pressure relief is nearly complete. This result shows that the inclusion of dilatancy, which occurs from inelastic deformation during loading (and thus during the initial portion of the wave profile), could further improve the wave characteristics.

#### **I-5. CONCLUSIONS AND RECOMMENDATIONS**

Metamorphism in rock media due to the passage of shock waves has been well-established. The associated changes in physical properties in turn affect the propagation of waves through the media. As evaluated through a numerical model, these changes result in code predictions of events such as PILE DRIVER which have significantly improved wave shapes over that previously obtained. Use of the shock-conditioning model should also permit the adoption of a more realistic failure model for granite, in place of the extremely low strength model which up to now had been most successful in predictions, but had been suspect from the standpoint of experimental measurements of material properties.

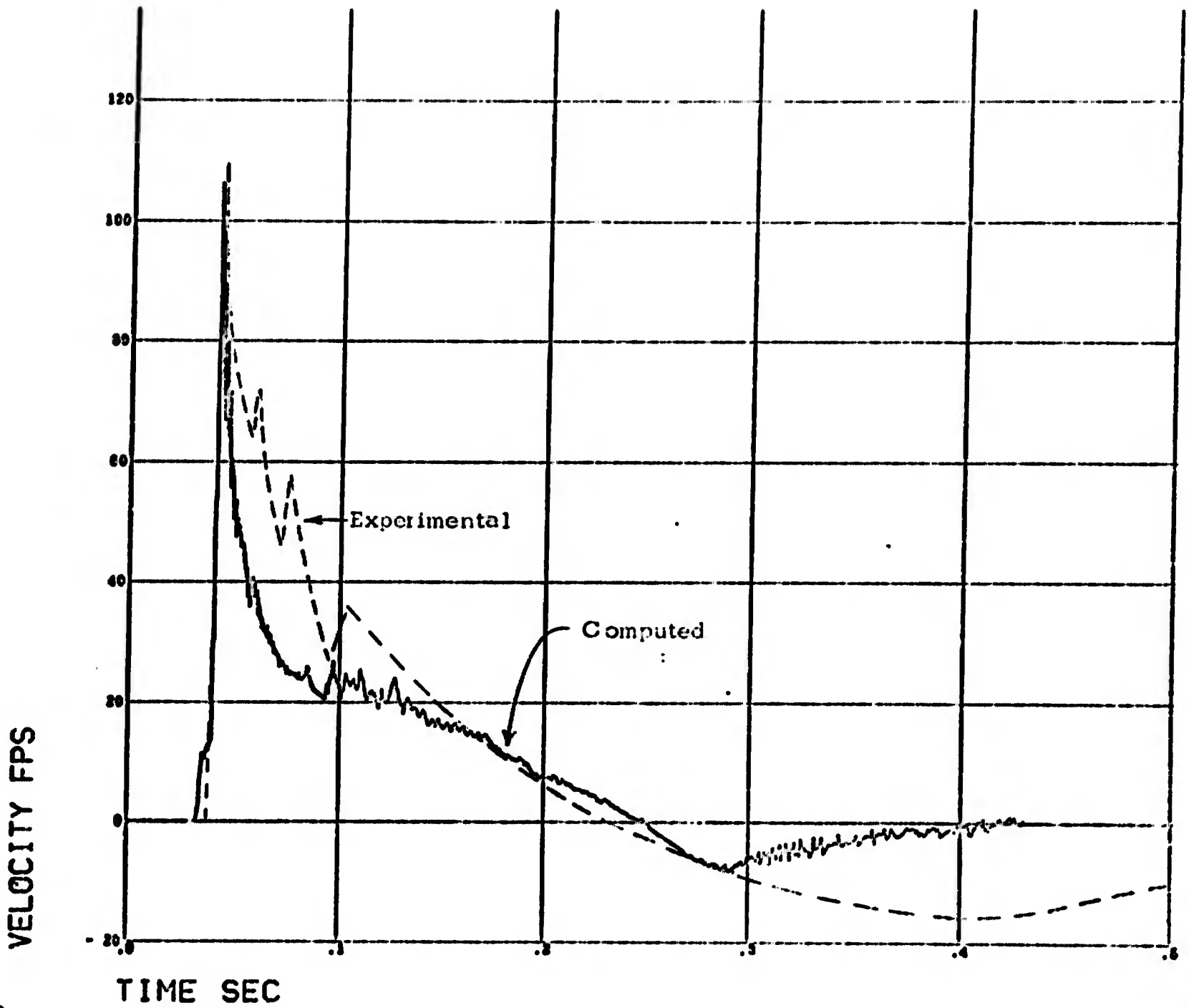


Figure 19. Radial Velocity vs Time, Range = 668 ft, Case Without Bulking

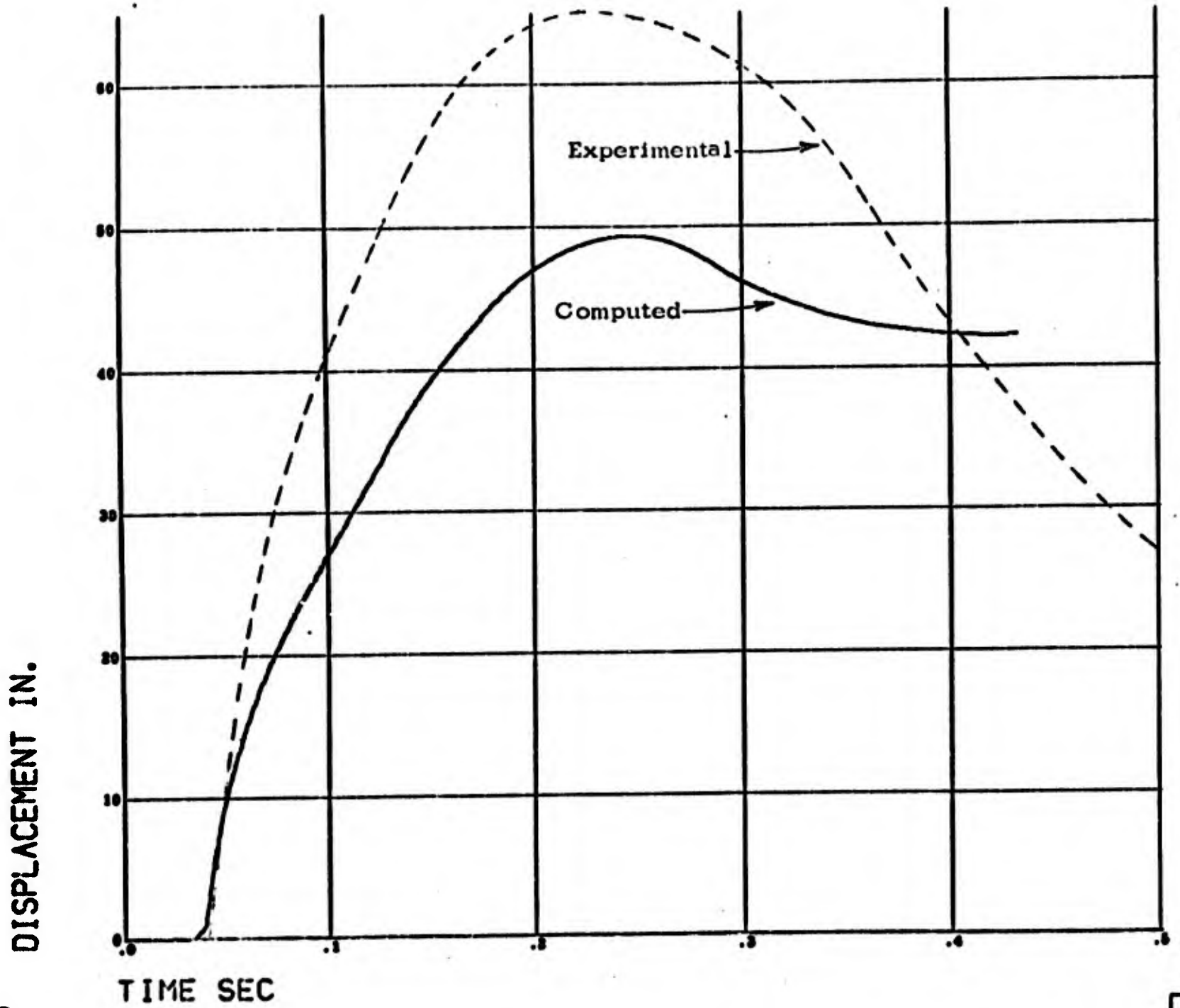


Figure 20. Radial Displacement vs Time, Range = 1543 ft, Case Without Bulking

A further modification to the overall model, to include dilatant effects, holds promise for further improvement in the predictions: The investigation of a model including

- a. Shock conditioning effects
- b. Dilatancy
- c. Improved failure model (fracture surface)

is recommended for future work. All of these have been separately formulated and coded, but as yet have never been combined into an overall model and tested in numerical solutions.

#### **ACKNOWLEDGMENTS**

The following individuals made important contributions to the program: J. Reid, who performed the computer programming, N. Louie who assisted in the analysis, and M. Rosenblatt, who modified the granite equation of state in the vapor region.

I-6.      REFERENCES

1. T. R. Butkovich, J. Geophys. Res. 70, 885 (1965).
2. J. T. Cherry, Int. J. Rock Mech. Min Sci. 4, 1 (1967).
3. J. T. Cherry and E. G. Rapp, Calculation of Free-Field Motion for the PILE DRIVER Event, Lawrence Radiation Laboratory, Livermore, UCRL-50373 (1968).
4. Beneficial Site Model Ground Motion Calculations, SAMSO-TR-68-126 (1968).
5. M. W. McKay and C. S. Godfrey, Study of Spherically Diverging Shock Waves in Earth Media, DASA Report 2223 (1969).
6. M. H. Wagner and N. A. Louie, HARD HAT/PILE DRIVER Ground Motion Calculations, SAMSO TR-69-47 (1969).
7. W. R. Perret, Free Field Ground Motion in Granite, Sandia Laboratory, POR-4001 (1968).
8. N. M. Short, J. Geophys. Res. 71, 1195 (1966).
9. C. R. Boardman, D. D. Rabb, and R. D. McArthur, J. Geophys. Res. 69, 3457 (1964).
10. B. M. French and N. M. Short, Ed., Shock Metamorphism of Natural Materials (Mono Book Corp., Baltimore, 1968).
11. J. H. Scott, R. D. Carroll, and D. R. Cunningham, Seismic Studies in PILE DRIVER Tunnels, Area 15, Nevada Test Site, Nevada, U. S. Dept. of the Interior, Geological Survey, Denver, Colorado, Tech. Ltr: PILE DRIVER-1 (1965).
12. F. N. Houser and F. G. Poole, Summary of Physical and Chemical Nature of Granite Rocks at the U15a Site, U. S. Dept. of the Interior, Geological Survey, Denver, Colorado, Tech. Ltr.: Area 15-1 (1961).
13. E. J. Deklotz and W. J. Heck, Strengthening of Rock Against Shock Effects, U. S. Army Corps of Engineers, Missouri River Div. Laboratory, Report No. 64/90 (1964).

14. M. M. Mehta, V. S. Gupta, and W. H. Somerton, Changes in Physical Properties of Rocks in the Vicinity of an Underground Nuclear Explosion, Inst. of Engr. Res., Univ. of Calif., Project UCX-2315 (1964).
15. W. R. Perret, Free-Field Ground Motion Studies in Granite, Sandia Corp., POR-1803 (1963).
16. S. P. Clark, Jr., Ed., Handbook of Physical Constants, Rev. Ed. (The Geological Society of America, Inc., New York, 1966).
17. D. R. Stephens, J. Geoph. Res. 69, 2967 (1964).
18. D. R. Stephens and E. M. Lilly, Static PV Curves of Cracked and Consolidated Earth Materials, Lawrence Radiation Laboratory, Livermore, UCRL-14711 (1966).
19. P. N. LaMori, Compressibility of Three Rocks: (A) Westerly Granite and Solenhofen Limestone to 40 KB and 300 C, (B) Cedar City Tonalite to 40 KB at Room Temperature, Proceedings: Strategic Structures Research, Vulnerability/Hardening Long Range Planning Meeting, Volume I, DASA Report 2288-I (1969).
20. N. B. Brooks and R. L. Lansdale, SHAPE-II Code, Hardening Technology Studies - III, SAMSO-TR-68-69 (1968).
21. C. R. Boardman, Results of an Exploration into the Top of the PILE DRIVER Chimney, Lawrence Radiation Laboratory, Livermore, UCRL-50385 (1967).

**BLANK PAGE**

PART II  
A SET OF CONSTITUTIVE RELATIONS FOR ROCKS AND SOILS  
by M. Rosenblatt

II-1. INTRODUCTION

A phenomenological model for rocks and soils is presented. The model includes the following general features.

1. The inelastic shear deformation depends on the proximity of the current stress state to the static failure surface.
2. Dilatancy is controlled by the amount of inelastic shear deformation. Thus, the inelastic shear deformation due to slippage and crack propagation is treated as the cause of dilatancy.
3. Hysteresis is included by permitting the equation of state to be a function of the peak density experienced by a material element up to the present time.
4. The inelastic deformation is sensitive to the total deformation rate. Thus, the model is "strain rate sensitive".

In Section 2, the proposed constitutive relations are presented in their general form. In Section 3, some of the similarities and differences between the proposed model and the elastic-plastic model are discussed. In Section 4, the model is specialized to the case of triaxial loads with  $\sigma_2 = \sigma_3$ ; and the model is applied to quasi-static experimental data generated for granite. The method of choosing the material parameters in the model given the experimental data is also discussed in Section 4. In Section 5, the model is shown to satisfy the uniqueness of solution requirement. A table of symbols for Part II appears on page 79.

II-2. CONSTITUTIVE EQUATIONS

The proposed constitutive relations can be conveniently separated into deviatoric and non-deviatoric equations. (The deviator of the tensor  $T_j^i$  is  $T_j^{i*} = T_j^i - \frac{T_k^k}{3} \delta_j^i$ ). The deviatoric equations are of a form proposed by Piotr Perzyna for viscoplastic materials.<sup>1,2\*</sup> The non-deviatoric equation is analogous to a hydrodynamic equation of state. In the proposed model, however, the equation of state depends on the amount of inelastic deformation and on the peak density which has been experienced. The equation of state of a material element therefore depends upon its history.

\*Superscripts are reference numbers. The Reference List for Part II is on page 81.

A material element which has experienced a large amount of inelastic deformation thus will have a different equation of state than a material element which has been thus far undisturbed. Similarly, a material element which has been severely compressed may show a hysteretic effect due to a change in the material equation of state resulting from irreversible compaction.

The complete set of proposed constitutive relations in terms of the stress ( $\sigma_{ij}$ ), the deformation rate ( $d_{ij} = \frac{1}{2} (u_{i,j} + u_{j,i})$ ), the spin tensor ( $\omega_{ij} = \frac{1}{2} (u_{i,j} - u_{j,i})$ ), the density ( $\rho$ ), and the specific internal energy ( $e$ ) are given below:

$$\frac{\dot{\Lambda}}{2G} \frac{\sigma_{ij}^*}{\sigma_{ij}^*} = d_{ij}^* - \gamma \bar{\phi}(F) \frac{\sigma_{ij}^*}{\sqrt{J_2^*}} \quad (1)$$

$$\frac{\sigma_k^k}{3} = \Pi(\rho, e, I, \rho_m) = P \quad (2)$$

where

$$\dot{\Lambda} \frac{\sigma_j^i}{\sigma_j^i} = \dot{\sigma}_j^i + \sigma_k^i \omega_j^k - \omega_k^i \sigma_j^k \quad \text{Jaumann Stress Rate} \quad (3)$$

$$\dot{i} = \gamma \bar{\phi} = \sqrt{1/2 \left( d_{ij}^* - \frac{\Lambda}{2G} \frac{\sigma_{ij}^*}{\sigma_{ij}^*} \right) \left( d_{ij}^* - \frac{\Lambda}{2G} \frac{\sigma_{ij}^*}{\sigma_{ij}^*} \right)} \quad (4)$$

$$\rho_m = \text{Max} \{ \rho(\tau) \}, \text{ where } \tau \leq t \quad (t \text{ is time}) \quad (5)$$

$$F = F(J_2', \alpha, I, e, P) \quad (6)$$

$$\alpha = \frac{\sigma_1 - \sigma_3}{H} \quad \text{where } \sigma_1 - \sigma_3 = H(P, \sigma_2) \quad (7)$$

is the static failure surface  
( $\sigma_1 \geq \sigma_2 \geq \sigma_3$ )

$$\bar{\phi}(F) = \begin{cases} 0 & \text{for } F \leq 0 \\ \phi(F) & \text{for } F \geq 0 \end{cases} \quad (8)$$

$$\gamma \quad \text{Material constant with dimensions of } \left[ \frac{1}{\text{time}} \right] \quad (9)$$

G Shear modulus, can depend on e, I, or P if dependence is known.

Equation (1) is the deviatoric portion of the constitutive relations. Equation (3) is the Jaumann definition of stress rate, used to satisfy the principal of objectivity. This is not the only choice which satisfies the principal of objectivity. However, as pointed out by Prager<sup>3</sup>, the Jaumann stress rate does possess the desirable property that all the time derivatives of the invariants of the stress will vanish when the Jaumann stress rate vanishes. Prager<sup>3</sup> mentions three objective stress rates (the Cotter-Rivlin, Oldroyd, and Truesdell definitions of stress rate) which upon vanishing do not imply stationary behavior of the stress invariants.

The second term on the right hand side of Eqn. (1) controls the inelastic and rate sensitive behavior of the material. Thus,

$$\dot{\sigma}_{ij} = \gamma \bar{\phi}(F) \frac{\sigma_{ij}^*}{\sqrt{J_2'}} \quad (10)$$

where

$$J_2' = \frac{\sigma_{ij}^* \sigma_{ij}^*}{2}$$

Note that Eqn. (1) shows that the inelastic behavior is always in the direction to reduce  $\sigma_{ij}^*$ . The function  $\bar{\phi}(F)$  and the parameter  $\gamma$  control the amount and rate of inelastic relaxation. Inelastic relaxation of stress will occur as long as  $F > 0$ . Thus  $F(J_2', \alpha, I, e, P) = 0$  is the equation which describes the maximum  $J_2'$  which the material can support in a quasi-static state.  $F = 0$  is the equation analogous to the "Yield Condition" in the theory of plasticity. Note, however, that dynamically  $F$  and  $J_2'$  can exceed the quasi-static limits. The amount of excess deviatoric stress, i.e., that above the quasi-static limit, is determined by  $\gamma$  and  $\bar{\phi}(F)$ . In particular, Eqns. (4) and (10) show that

$$\sqrt{\frac{\dot{\sigma}_{ij} \dot{\sigma}_{ij}}{2}} = \dot{f} = \gamma \bar{\phi}(F) \quad (11)$$

and

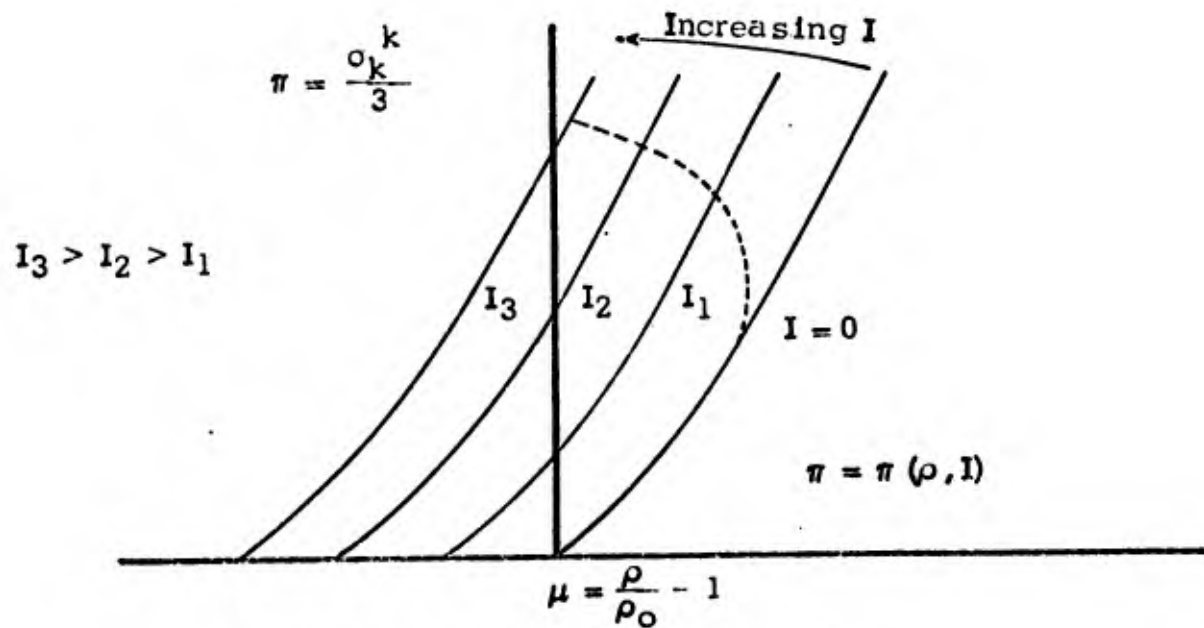
$$F = \bar{\phi}^{-1} \left( \frac{\dot{f}}{\gamma} \right) \quad (12)$$

where  $\bar{\phi}^{-1}$  is the inverse function of  $\bar{\phi}$ . Thus the extent to which  $F$  can be greater than zero is controlled by the choice of  $\bar{\phi}^{-1}$  and  $\gamma$ .

$F$  has been made a function of the variable  $\alpha$ .  $\alpha$  (Eqn. (7)) is a measure of the proximity of the current state of stress to the static failure surface,  $\sigma_1 - \sigma_3 = H$ . For unstressed states,  $\alpha = 0$ . For stress states on the static failure surface,  $\alpha = 1$ . The variable  $\alpha$  has been included in the formulation because rocks and soils exhibit inelastic behavior

before reaching the failure surface. The use of the variable  $\alpha$  in the function  $F$  permits the amount of inelastic deviatoric strain to be controlled in a very physically meaningful fashion, i.e., the amount of inelastic strain will, in part, depend on how close we are to the static failure surface. Thus in this model, inelastic deformation is due to mechanisms such as slippage and/or crack propagation which occur as the failure surface is approached.

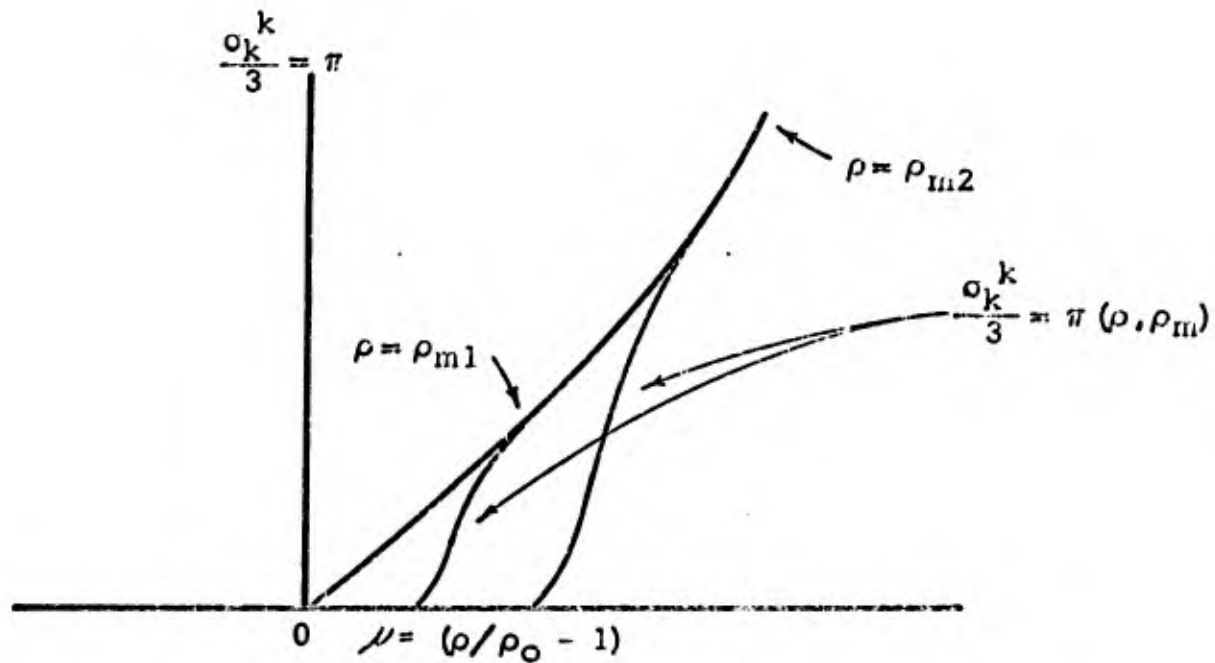
Equation (2) relates the mean stress to the density, specific internal energy, inelastic strain, and the maximum density experienced by the material element up to the present time  $t$ . The inelastic strain measure,  $I$ , is used in Eqn. (2) to describe dilatancy. The following sketch qualitatively illustrates the dependence of the function  $\pi$  on the variable  $I$ . (The effects of  $e$  and  $\rho_m$  are ignored.)



Qualitative Sketch of  $\pi$  versus  $\rho$  and  $I$

The sketch shows that if there is no inelastic behavior ( $I = 0$ ), then the mean stress versus compression ( $\mu = \rho/\rho_0 - 1$ ) curve will be specified by  $\frac{\sigma_j}{3} = \pi(\rho, 0)$ . If inelastic deformation does occur ( $I > 0$ ), then the mean stress versus compression curve is shifted to the left. Thus, the density for  $I > 0$  is lower than for  $I = 0$  at the same mean stress. The dashed line in the sketch illustrates a possible stress-density path if the inelastic deformation, as measured by  $I$ , increases during the stress loading.

In a similar fashion, the degree of hysteresis is controlled by the dependence of the function  $\pi$  on  $\rho_m$  ( $\rho_m$  is the maximum density experienced by a material element up to the present time). If a material element has been compressed to a large density, the relationship between mean stress and density may change. The following sketch illustrates the dependence of  $\sigma_k^{1/3} = \pi$  on  $\rho_m$ . The dependence of  $\pi$  on  $e$  and  $I$  has been ignored in this sketch.



Qualitative Sketch of  $\pi$  versus  $\rho$  and  $\rho_m$

Note that it may be possible for a material to exhibit both dilatancy and hysteretic effects. In any case, dilatancy and hysteretic effects are accounted for in the model by permitting the function  $\pi$  to depend on  $I$  and  $\rho_m$  as well as  $\rho$  and  $e$ .

### II-3. SOME COMPARISONS OF THE PROPOSED MODEL AND THE ELASTIC-PLASTIC MODEL

The primary differences between the proposed model and the elastic-plastic model are due to the nature and consequences of the "Yield Condition." In the elastic-plastic theory a yield condition is written such that

$$F_{e-p} = F_{e-p}(J_2', P, I, e, \dots) \leq 0 \quad (13)$$

When  $F_{e-p} < 0$ , then the equations of elasticity (in the deformation rate form) are applicable. If at any instant, however, there is any tendency for  $F_{e-p}$  to become greater than zero, then a plastic flow rule is applied which forces  $F_{e-p} = 0$ .

In the proposed model, the function  $F = F(J_2', \alpha, I, e, P)$  is analogous to the function  $F_{e-p}$ . The condition  $F_{e-p} < 0$  is exactly equivalent to  $F < 0$  in terms of the incremental material behavior. This correspondence results from the fact that  $\phi(F) = 0$  if  $F \leq 0$ , and  $\phi(F) = 0$  implies that the constitutive relations reduce to an elastic model. One important difference between the models is that in the rate sensitive model  $F$  can be greater than zero. When  $F$  is greater than zero, inelastic deformation takes place causing a tendency to relax toward  $F = 0$  (See Eqn. (1)). The amount of inelastic relaxation is a function of the deformation rate and  $\gamma \phi(F)$ . Thus  $F > 0$  is possible under dynamic loadings. Quasi-static loadings are treated as the limiting case of  $d_{ij}d^{ij} \rightarrow 0$ . In quasi-static loadings,  $F$  can only become infinitesimally greater than zero, i.e.,  $F \leq 0^+$ .

The inclusion of rate sensitivity in the proposed model permits uniqueness of solution to be demonstrated. This is done in Section 5 by showing that the governing partial differential equations are hyperbolic in nature. The rate sensitivity is observed in experiments on rock materials<sup>4,5</sup>. However, if the rate sensitivity is considered negligible, then  $\gamma \phi(F)$  can be chosen as a very steep function and  $F$  will never become much greater than 0 due to very rapid relaxation toward the condition  $F = 0$ . It is important to note that the proposed model is not more complicated than the usual hydro-elastic-plastic models employed in large 2-D computer codes. The rate sensitive portion of the model has been programmed into our 2-D Eulerian code called STEEP, and numerical solutions have been conducted using the model<sup>6</sup>. In reference 6, the model was used to describe 2024-T3 aluminum and therefore the dilatancy and hysteretic effects were not included in the functional form of  $\sigma_1/3 = \pi$ . Also a yield surface was specified in place of a failure surface.

The elastic-plastic formulations have not, in general, used the mean stress relationship ( $\sigma_1/3 = \pi$ ) to account for the dilatancy and hysteretic effects observed in rocks and soils. The proposed model incorporates these effects directly in the mean stress versus density and energy relationship. Thus, the functional relationship between  $\sigma_1/3$ ,  $\rho_0$ , and  $e$  depend on the magnitude of the inelastic deformation ( $I$ ) and/or on the peak density which has been experienced by a material element ( $\rho_m$ ).

#### II-4. FITTING THE MODEL TO EXPERIMENTAL DATA.

So far, the model has been discussed in its general form. The functional forms for  $H$ ,  $F$ ,  $\pi$ , and  $\phi$  have been left arbitrary. These functions are, in general, chosen to fit the available experimental data. However, since the data are invariably incomplete, the functional forms are rarely determined uniquely.

These functions  $H$ ,  $F$ , and  $\pi$  can be determined from quasi-static loading and unloading tests conducted to failure.  $H = \sigma_1 - \sigma_3$  describes the failure locus in stress space,  $F = 0^+$  describes the amount of inelastic deformation which occurs as the failure locus is approached, and  $\pi = \alpha/3$  describes the amount of dilatancy and hysteresis. The variable  $\alpha$  has been introduced into the functional form for  $F$  because inelastic deformation depends on the proximity of the current stress state to the failure locus.

$\alpha = \frac{\sigma_1 - \sigma_3}{H}$  is one measure of this proximity. Also since  $\alpha = 1$  implies that a stress state is on the static failure surface, the relationship between inelastic deformation and failure can be easily specified in the function  $F = F(J_2', \alpha, I, e, P)$ . This point will be illustrated in Section 4.

The function  $\phi$  and the parameter  $\gamma$  are determined from high deformation rate experimental data. A technique for fitting  $\phi$  and  $\gamma$  to dynamic rate sensitive stress strain data has been developed and applied to aluminum in reference 6. This technique is currently being applied to rate sensitive data generated for granite. Equations (11) and (12) indicate the general nature of the rate sensitive dependence of  $F$ . For example, if  $\phi = e^{F/c_1} - 1$ , then Eqns. (11) and (12) show that

$$F = c_1 \ln \left( 1 + \frac{\dot{I}}{\gamma} \right). \quad (14)$$

Thus, in this example, the choice of the constants  $c_1$  and  $\gamma$  determine the rate sensitivity of  $F$  and thus of  $J_2'$ .

In dynamic problems,  $F > 0$  implies that  $J_2'$  can exceed the observed quasi-static limits on  $J_2'$  for a given amount of inelastic deformation. Similarly,  $\alpha = \frac{\sigma_1 - \sigma_3}{H}$  can exceed 1 before failure in dynamic problems. The conditions for failure under dynamic loads must be investigated further before a dynamic failure condition can be chosen. One possible form relating  $\alpha$  and failure follows:

$$\int_0^t \bar{f}(\alpha - 1) dt = \text{constant for failure}$$

where  $\bar{f}(\alpha - 1) = 0$  if  $\alpha < 1$   
 $f(\alpha - 1)$  if  $\alpha \geq 1$ .

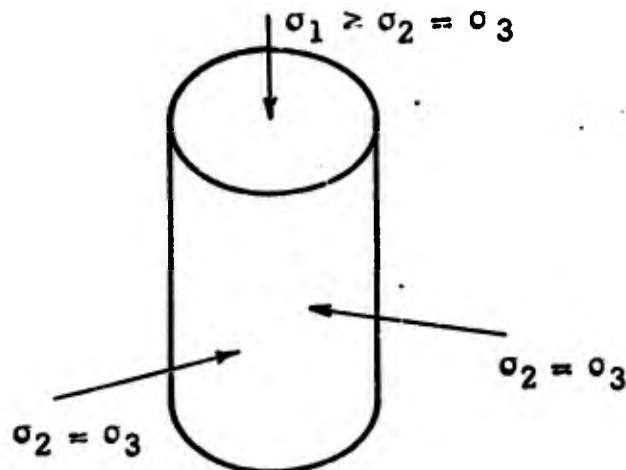
Thus,  $\alpha$  can be greater than the quasi-static limit of 1 for a short duration of time, depending on the above integral. The function  $f(\alpha - 1)$  must be found experimentally.

The rate sensitive aspects of the model will not be discussed further at this time due to the sparseness of the available data. However, note that when rate sensitive data becomes available for rocks and soils, these data can be incorporated into the proposed model. Until then, the rate sensitive parameters can be chosen in a very preliminary fashion to give agreement with the data which are available.

#### II-4.1 AN EXAMPLE OF THE TECHNIQUE FOR DETERMINING THE MATERIAL PARAMETERS IN THE PROPOSED MODEL

In this section, the choice of  $H$ ,  $F$ , and  $\pi$  are illustrated through the use of an example involving quasi-static tests on granite.<sup>7</sup>

The quasi-static tests involved granite loaded under triaxial compression ( $\sigma_1 \geq \sigma_2 = \sigma_3 \geq 0$ , where  $\sigma > 0$  implies compression). The following sketch illustrates the loading geometry.



The experimental failure curve from reference 7 is shown in Figure 1. A simple fit to these data is also shown in Figure 1. Note, however, that this failure curve includes only triaxial compression data. Triaxial extension and torsion failure data would be expected to fall below this curve. (For example, see reference 8.) In fact, one of the reasons for introducing the functions  $H$  and  $\alpha$  into the model is to account for the non-symmetrical behavior of the failure surface in the so called "Pi plane". In the present example, however, only triaxial compression data were obtained and therefore only a fit to the data in Figure 1 is necessary. It would be useful to obtain data similar to that of reference 7 for the case of triaxial extension ( $\sigma_1 = \sigma_2 > \sigma_3$ ).

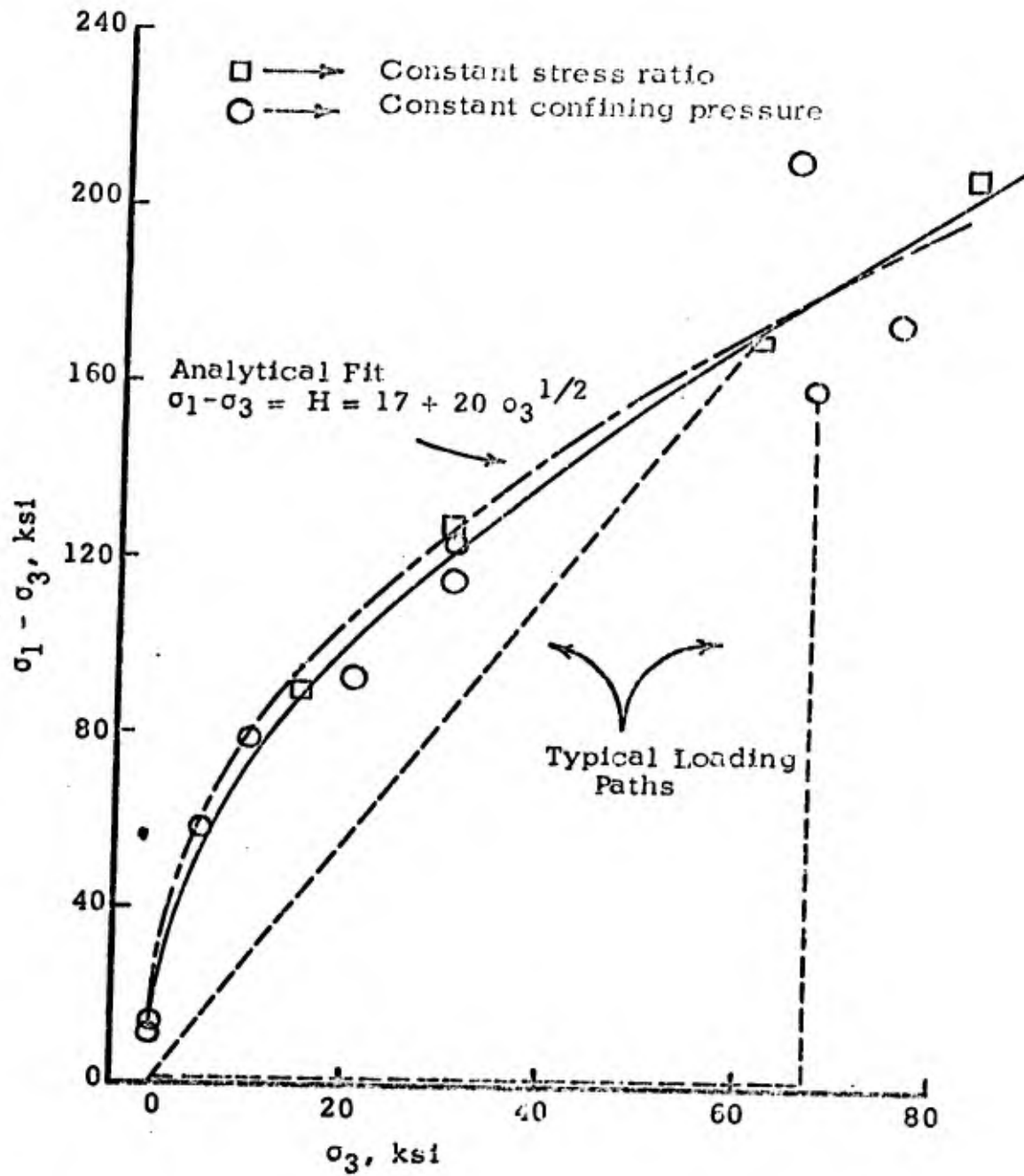


Figure 1. Failure Data<sup>7</sup> and Analytical Fit for Cedar City Granite in Constant Confining Pressure and Constant Stress Ratio Tests.

The fit to the failure surface is specified by the following equation

$$\sigma_1 - \sigma_3 = H = 17 + 20 \sigma_3^{1/2} \text{ (ksi)} \quad (15)$$

Thus  $\alpha$  is found to be

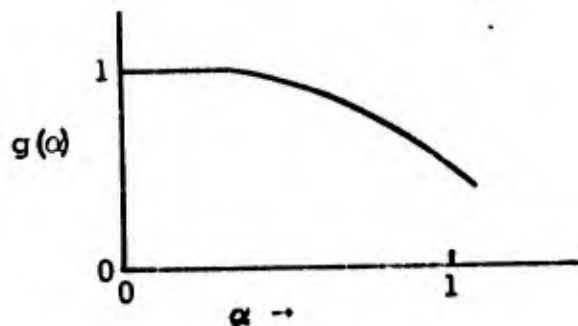
$$\alpha = \frac{\sigma_1 - \sigma_3}{H} = \frac{\sigma_1 - \sigma_3}{17 + 20 \sigma_3^{1/2}} \quad (16)$$

The important feature of Eqn. (16) is that  $\alpha = 0$  for the unstressed state, and  $\alpha = 1$  for states on the static failure surface.

The functional form for  $F$  cannot be uniquely defined from the data currently available. The following form, however, seems satisfactory for fitting the low stress granite data.

$$F = \frac{\sqrt{J_2'}}{2G} - g(\alpha) \left( \frac{\sqrt{J_2'}}{2G} + I \right) \quad (17)$$

$g(\alpha)$  is the function which controls the amount of inelastic deformation which the material experiences as the static failure surface is approached. Qualitatively,  $g(\alpha)$  will behave as indicated in the following sketch.



To illustrate the relationship between  $J_2'$ ,  $g(\alpha)$ , and  $I$ , consider a quasi-static loading path from the unstressed state to the failure surface. Initially,  $\alpha = 0$ ,  $J_2' = 0$ ,  $g(\alpha) = 1$ , and  $I = 0$ . As the stress is increased,  $\alpha$  and  $J_2'$  will increase, but  $g(\alpha)$  will remain at its initial value of 1 for a portion of the loading. As long as  $g(\alpha) = 1$ ,  $F$  will equal 0 (since  $I = 0$ ) and there will be no tendency for  $I$  to increase. Thus  $g(\alpha) = 1$  implies purely elastic deformation. When  $J_2'$  and  $\alpha$  are increased to the point where  $g(\alpha) < 1$ , then  $F$  would be greater than zero if  $I = 0$ . The condition  $F > 0$  causes inelastic deformation to occur until the condition  $F = 0$  is achieved. Equation (17) shows that  $F = 0$  implies

$$I = \frac{\sqrt{J_2'}}{2\mu} \frac{(1 - g(\alpha))}{g(\alpha)} \quad (18)$$

Thus as  $J_2'$  and  $\alpha$  are increased,  $g(\alpha)$  will decrease below 1, and therefore inelastic deformation ( $I > 0$ ) will develop such that Eqn. (18) is satisfied.

The functional form for  $F$  in Eqn. (17) was chosen because this form reduces to a simple expression for triaxial loadings. Under triaxial loadings, say  $\sigma_1 > \sigma_2 = \sigma_3 \geq 0$ ,

$$\sigma_1^* = 2/3 (\sigma_1 - \sigma_3), \quad \sigma_2^* = \sigma_3^* = -1/2 \sigma_1^*$$

$$\sqrt{J_2'} = \frac{\sqrt{3}}{2} \sigma_1^* = \frac{\sqrt{3}}{3} (\sigma_1 - \sigma_3)$$

and

$$I = \frac{\sqrt{3}}{2} \ln \epsilon_1^* \quad (19)$$

where

$\ln \epsilon_p$  is the inelastic strain.

Therefore,

$$F = \frac{\sqrt{3}}{2} \left\{ \frac{\sigma_1^*}{2G} - g(\alpha) \left( \frac{\sigma_1^*}{2G} + \ln \epsilon_1^* \right) \right\} \quad (20)$$

where

$$\sigma_1^* \geq 0.$$

Equation (20) can be further simplified by noting that Eqns. (1) and (10) imply

$$\epsilon_1^* = \frac{\sigma_1^*}{2G} + \ln \epsilon_1^* \quad (21)$$

where

$\epsilon_1^*$  is the first component of the total deviatoric strain. Thus,

$$F = \frac{\sqrt{3}}{2} \left( \frac{\sigma_1^*}{2G} - g(\alpha) \epsilon_1^* \right) \quad (22)$$

where

$$\sigma_1^* \geq 0$$

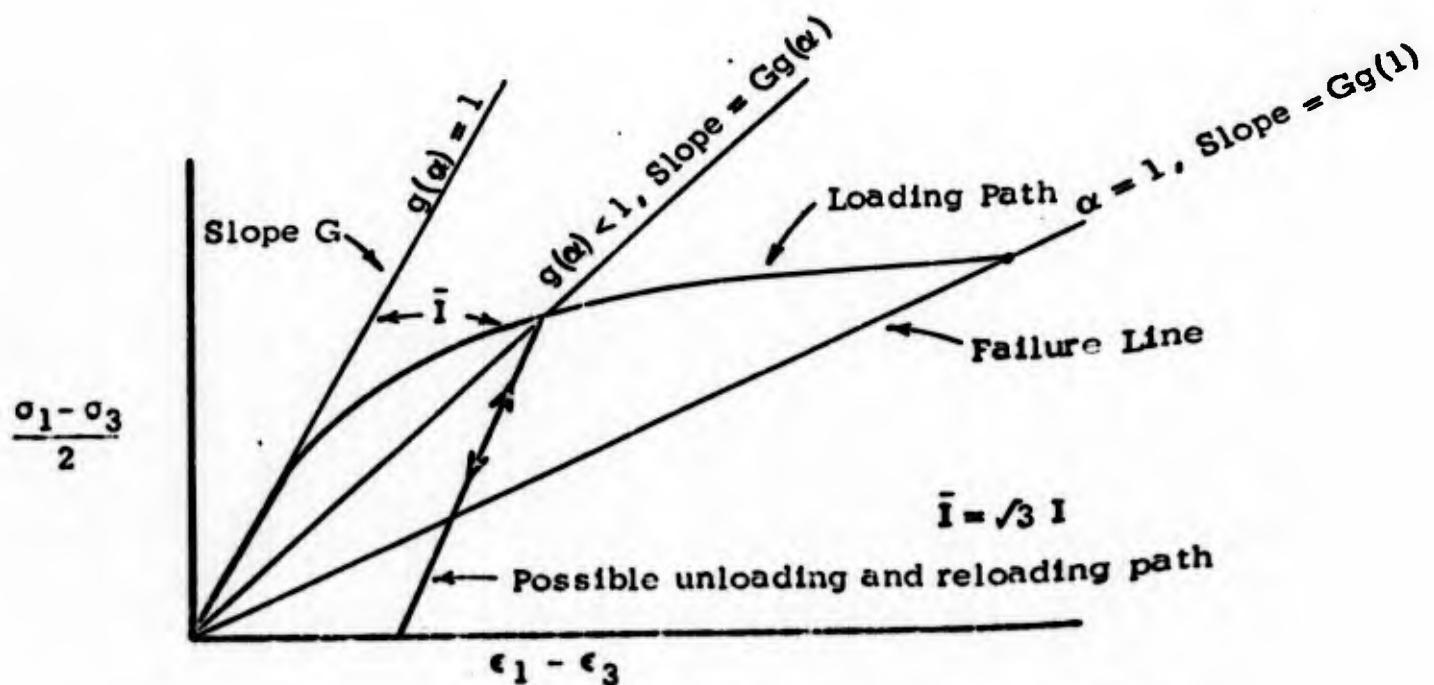
For triaxial loadings with  $\sigma_1^* \geq 0$ , Eqns. (22) and (1) are the fundamental relationships governing the deviatoric stress and strain. Under quasi-static loadings,  $F \leq 0^+$ . Thus, the equation  $F = 0$  describes the maximum deviatoric stress allowed for a given deviatoric strain under quasi-static loadings. For triaxial compression,  $F = 0$  implies

$$\sigma_1^* = 2G g(\alpha) \epsilon_1^* \quad (23a)$$

or

$$\frac{\sigma_1 - \sigma_3}{2} = G g(\alpha) (\epsilon_1 - \epsilon_3) \quad (23b)$$

The significance of Eqn. (23) is illustrated in the following sketch.



Sketch of Possible Loading Path in  $\frac{\sigma_1 - \sigma_3}{2}$  vs  $\epsilon_1 - \epsilon_3$  Space.

Three lines of constant  $g(\alpha)$  are shown on this sketch.  $g(\alpha) = 1$  corresponds to the linear elastic stress-strain relationship. A typical stress loading path will reach a stress state where  $g(\alpha) < 1$ . At this point, inelastic deformation occurs until the stress and strain lie on the line with slope  $G g(\alpha)$ . The details of the loading stress determine the exact location on the line. However, it is important to note that as long as  $F = 0$ , the stress-strain point will lie somewhere along the line

$$\frac{\sigma_1 - \sigma_3}{2} = G g(\alpha) (\epsilon_1 - \epsilon_3). \text{ This is a very useful}$$

feature of the model because failure always occurs in quasi-static loadings when  $\alpha = 1$ . Therefore  $g(1)$  can be chosen to fit the locus of the failure data in deviatoric stress-strain space. (The proposed form for  $F$  requires that failure occur along a straight line passing through the origin in stress-strain space. This seems to fit the data satisfactorily for granite. However, other experimentally observed relationships for the failure curve in stress-strain space can be incorporated in the model by an appropriate choice of the functional form of  $F$ .)

Figure 2 (from reference 7) shows stress-strain paths under various loadings for granite. The location of the failure points on this figure are approximately fit by a line with slope 1400 ksi passing through the origin. (The failure of specimen 11 occurred at a much higher stress level than the fit to the failure surface would predict. The failure data from this test was ignored in choosing the failure line on Figure 2.) Thus  $g(\alpha)$  for  $\alpha = 1$  can be determined once the elastic shear modulus,  $G$ , is determined. From Figure 2, an approximate value of  $G$  was chosen as

$$G = 3500 \text{ ksi.}$$

Using this value of  $G$ , it follows that the slope of the failure line in  $\frac{\sigma_1 - \sigma_3}{2}$  vs  $\epsilon_1 - \epsilon_3$  space is given by

$$\text{slope } (\alpha = 1) = G g(\alpha = 1) \tag{24}$$

Therefore,

$$g(1) = \frac{1400}{3500} = .4 \tag{25}$$

(Note that the failure line is the locus of failure points of all possible loading paths in stress-strain space.)

Figure 2 also indicates that the material remained essentially elastic until  $\alpha$  attained a value of approximately .4. Thus it was assumed that  $g(\alpha) = 1$  for  $\alpha \leq .4$ . This means that the material behaves elastically until the stress state is such that  $\alpha = .4$ . The rest of  $g(\alpha)$  was chosen as a quadratic form which passes through  $g(.4) = 1$  and  $g(1) = .4$ . The

- B - Specimen No. 22, One-dimensional strain,  $\epsilon_2 = \epsilon_3 = 0$
- C - Specimen No. 10, Unconfined compression
- D - Specimen No. 8, Constant pressure  $P = 5$  KSI
- E - Specimen No. 7, Constant pressure  $P = 10$  KSI
- F - Specimen No. 6, Constant pressure  $P = 20$  KSI
- G - Specimen No. 5, Constant pressure  $P = 30$  KSI
- H - Specimen No. 11, Constant pressure  $P = 67$  KSI
- I - Specimen No. 12, Constant stress-ratio,  $\sigma_3/\sigma_1 = 0.132$
- J - Specimen No. 13, Constant stress-ratio,  $\sigma_3/\sigma_1 = 0.186$
- K - Specimen No. 15, Constant stress-ratio,  $\sigma_3/\sigma_1 = 0.254$
- L - Specimen No. 17, Constant stress-ratio,  $\sigma_3/\sigma_1 = 0.282$

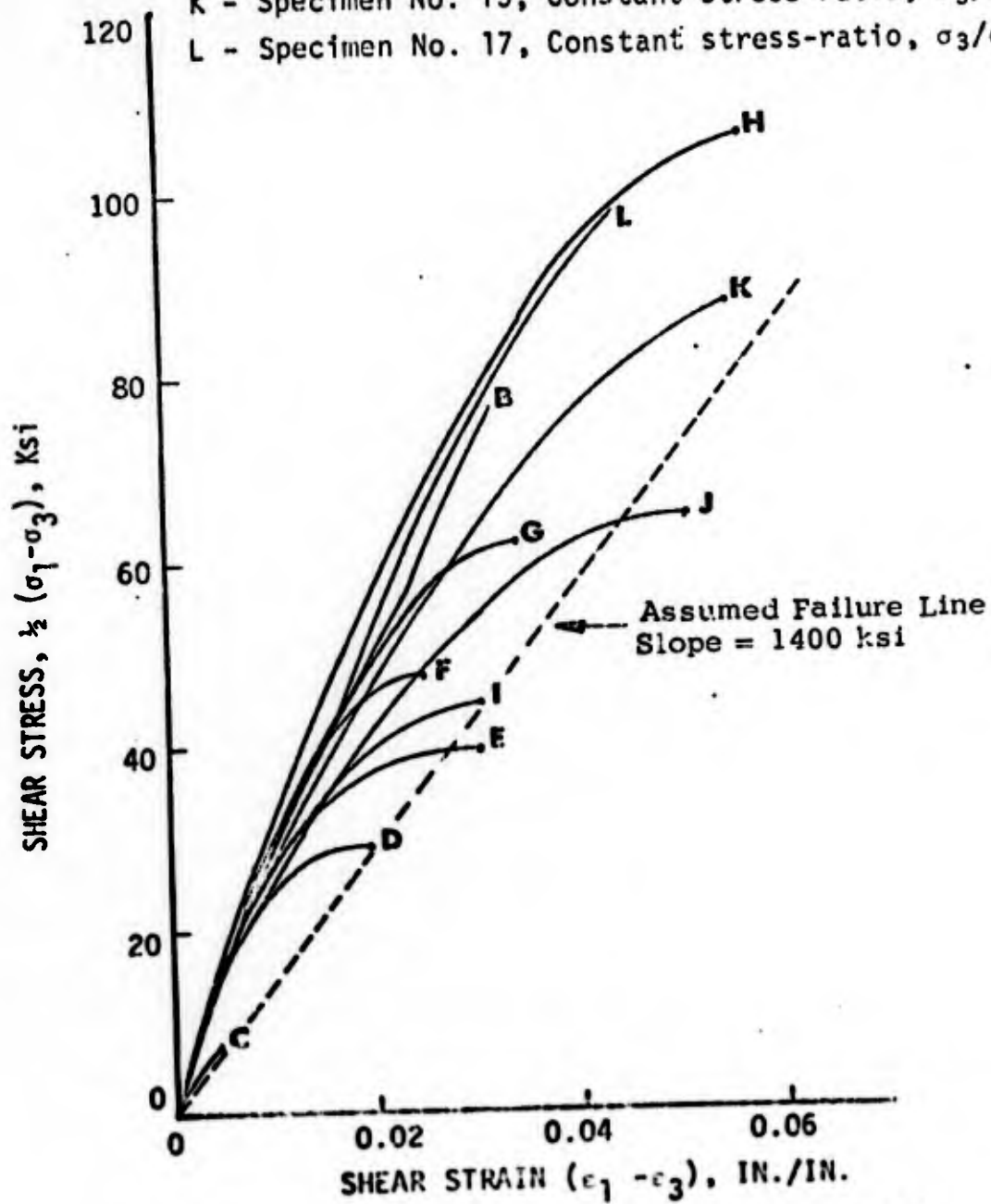
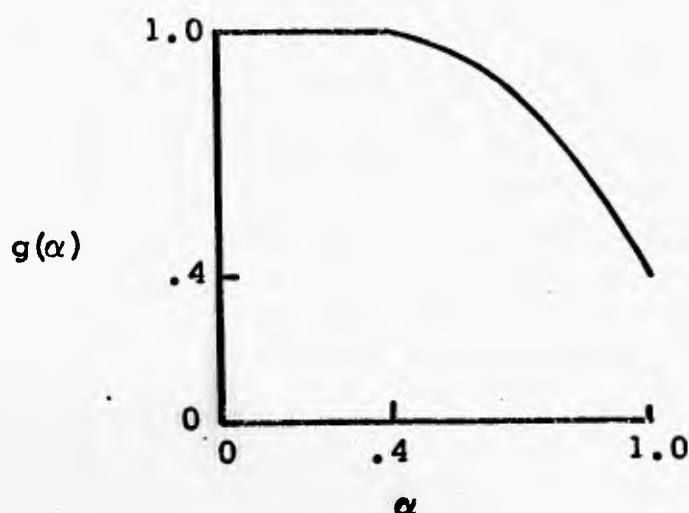


FIGURE 2. Shear stress-strain curves for Cedar City granite

quadratic form was chosen because it was the simplest form which would permit  $dg/d\alpha$  to be continuous at  $\alpha = .4$ . The functional form of  $g(\alpha)$  for values of  $\alpha$  between .4 and 1. will determine how the transition in stress-strain space is made from the elastic line to the failure line.

The final form chosen for  $g(\alpha)$  is indicated below.

$$\begin{aligned}
 g(\alpha) &= 1 & , \alpha \leq .4 \\
 g(\alpha) &= 1 - \frac{(\alpha - .4)^2}{.6} & , .4 \leq \alpha \leq 1
 \end{aligned}
 \tag{26}$$



The expressions defining the failure surface (Eqn. (16)), the function  $F$  (Eqn. (22)), and the function  $g$  (Eqn. (26)) are sufficient for predicting the deviatoric stress-strain behavior of the modeled granite. Figures 3 and 4 show the experimental data of Figure 2 versus the model predictions for the constant confining pressure tests ( $\sigma_3 = P = \text{constant}$ ) and for the constant stress ratio tests ( $\sigma_3/\sigma_1 = \text{constant}$ ). Considering the variation between the various rock specimens, the model fit appears good. Also, note that a large effort was not spent on getting a "best fit". The primary purpose of the current fit was to demonstrate that the model can reasonably predict the observed experimental data.

Figure 5 shows the dilatancy effect in granite as measured in reference 6. In the model, dilatancy is a function of the inelastic deformation parameter  $I$ . For low stresses, and for non-hysteretic materials, dilatancy is controlled by an expression of the following form.

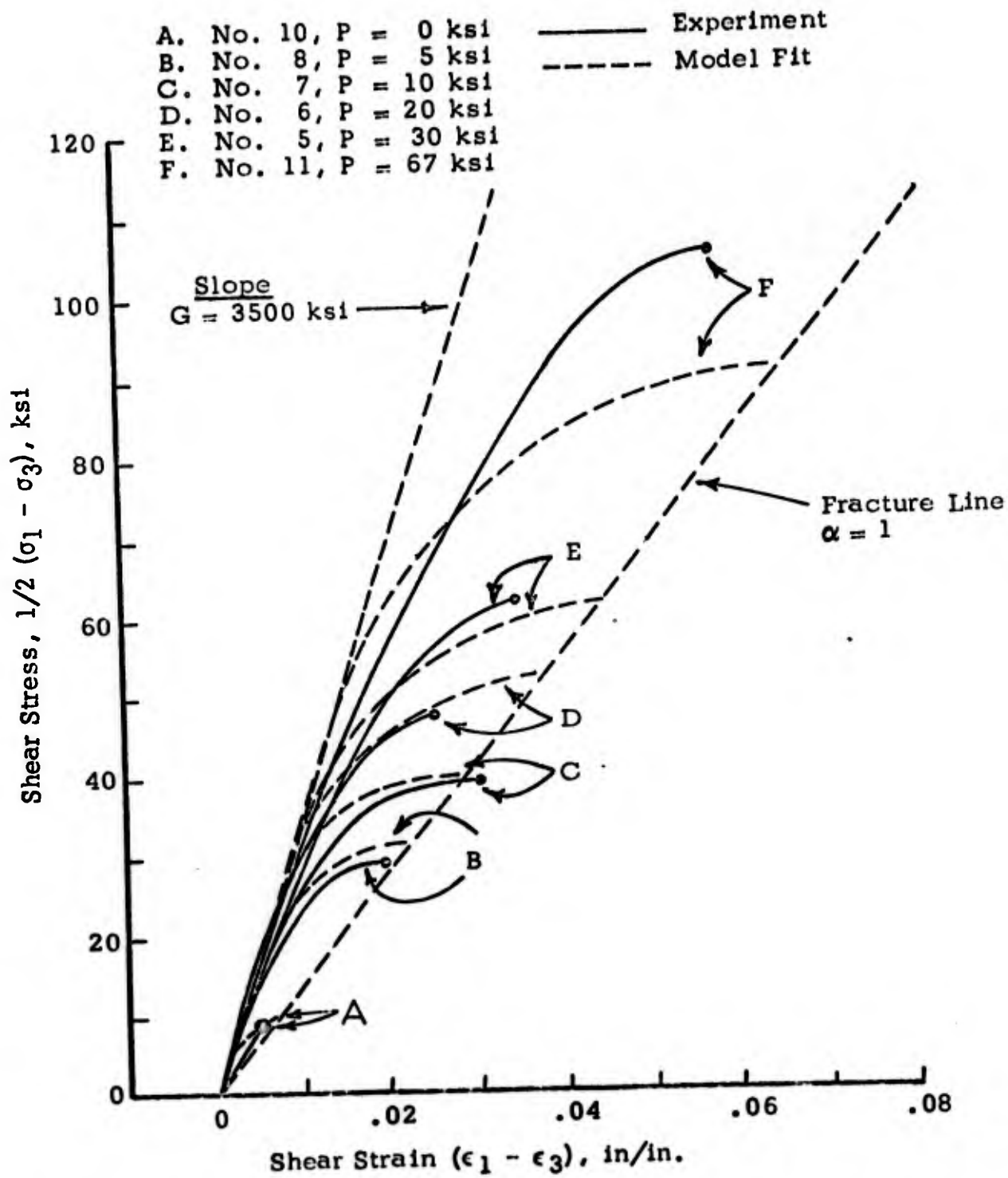


Figure 3. Shear Stress-Strain Curves for Six-inch Core Cedar City Granite, Triaxial Stress.

A.	Specimen No.	12,	$\sigma_3/\sigma_1 =$	0.132	
B.	"	"	13,	"	0.186
C.	"	"	15,	"	0.254
D.	"	"	17,	"	0.282

————— Experimental

- - - - - Model Fit

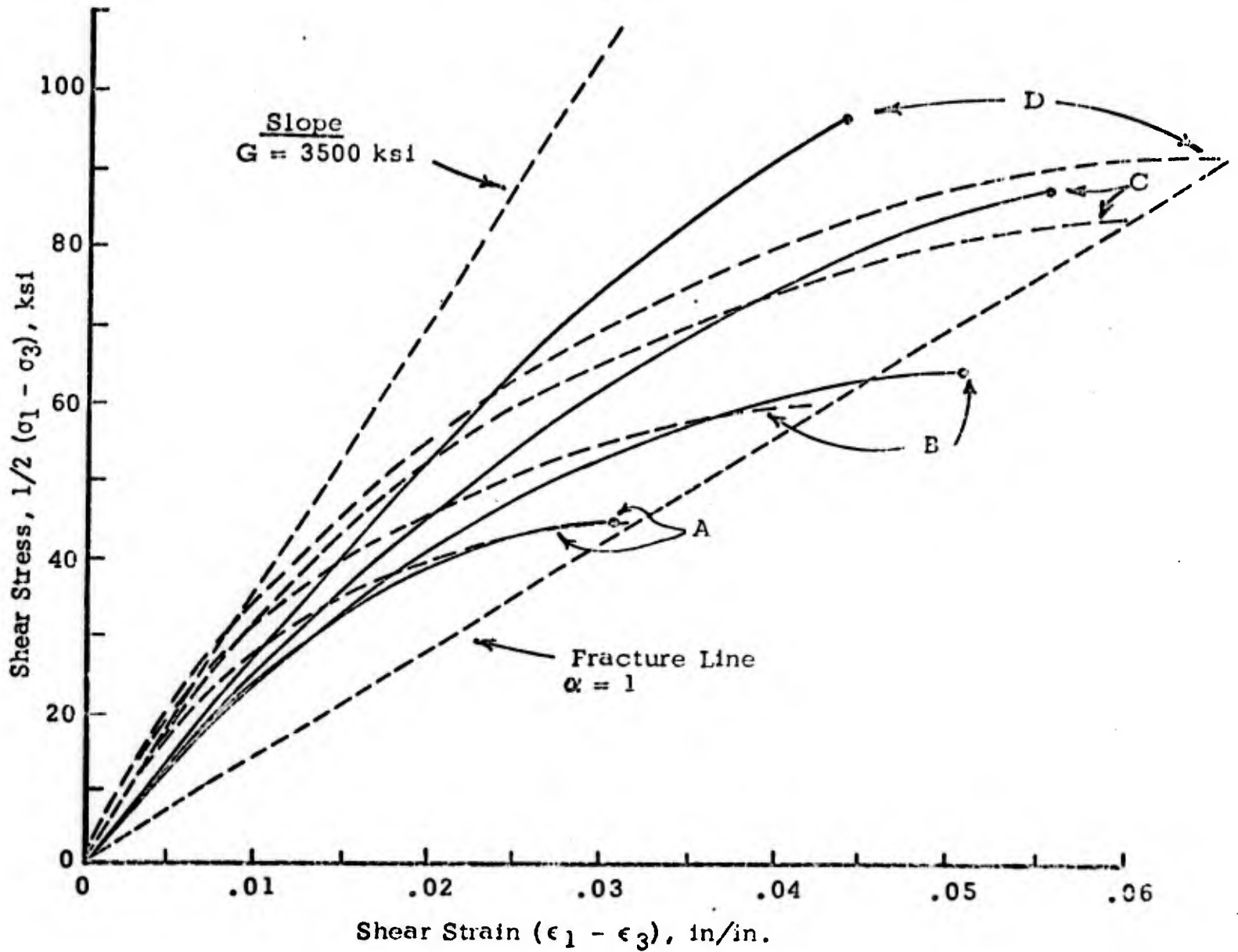


Figure 4. Shear Stress-Strain Curves for Six-inch Core Cedar City Granite, Constant Stress Ratio Tests.

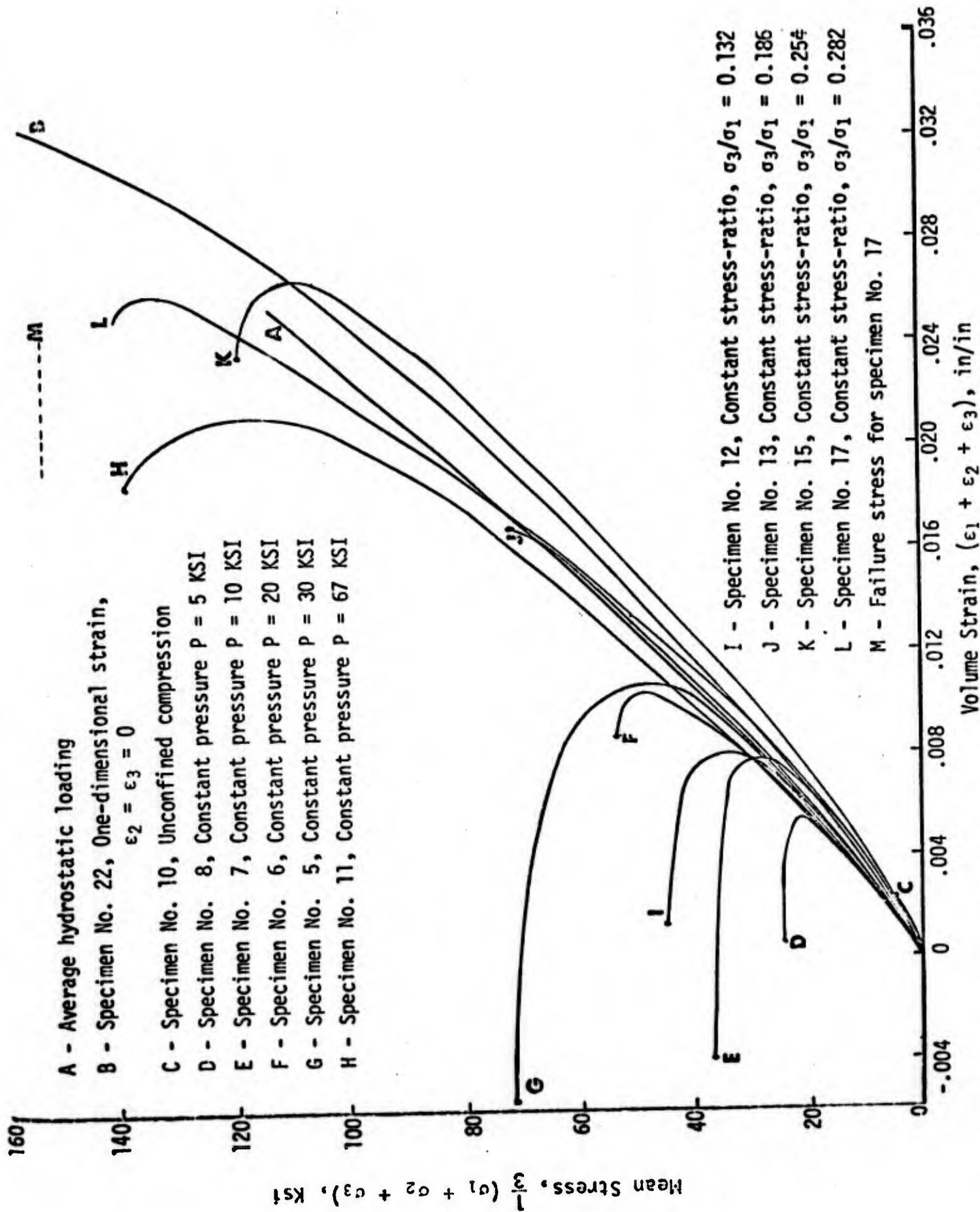


Figure 5. Dilatation stress-strain curves for Cedar City 6" core granite, constant pressure, constant stress ratio, one-dimensional strain, and hydrostatic tests. (From Reference 6)

$$\frac{\sigma_j^j}{3} = \pi (\epsilon_j^j, I) \quad (27)$$

where  $\epsilon_j^j$  has been used as the measure of volume change in place of the density,  $\rho$ . To first order  $\epsilon_j^j = \frac{\rho}{\rho_0} - 1$ . A very simple example of Eqn. (27) is

$$\frac{\sigma_j^j}{3} = K (\epsilon_j^j + \beta I) \quad (28)$$

where  $\beta \geq 0$  is a constant to be fit to the experimental data. A nominal bulk modulus value of  $K = 3900$  ksi was chosen from Figure 5.  $I$  is evaluated in the triaxial compression tests from

$$I = \frac{\sqrt{3}}{2} \ln \epsilon_I^* = \frac{\sqrt{3}}{2} (\epsilon_1^* - \frac{\sigma_1^*}{2G}) = \frac{\sqrt{3}}{2} \epsilon^* (1 - g(\alpha))$$

or

$$I = \frac{\sqrt{3}}{3} (\epsilon_1 - \epsilon_3) (1 - g(\alpha)) = \frac{\sqrt{3}}{3} \bar{I} \quad (29)$$

where

$$\bar{I} = (\epsilon_1 - \epsilon_3) (1 - g(\alpha)) = \frac{\sigma_1 - \sigma_3}{2G} \frac{1 - g(\alpha)}{g(\alpha)} = \sqrt{3} I$$

$\bar{I}$  is the inelastic strain component in  $\frac{\sigma_1 - \sigma_3}{2}$  versus  $\epsilon_1 - \epsilon_3$  space (see sketch below Eqn. 23). In terms of the deformation parameter  $\bar{I}$ , Eqn. (28) can be rewritten as

$$\frac{\sigma_j^j}{3} = K (\epsilon_j^j + \bar{\beta} \bar{I}) \quad (30)$$

where

$$\bar{\beta} = \frac{\sqrt{3}}{3} \beta$$

This form (Eqn. (30)) was used to fit the experimental data of Figure 5.  $\bar{\beta}$  was chosen to be .3.

Figures 6 and 7 show the details of the model fit versus the experimental data using  $\bar{\beta} = .3$  which implies  $\beta = (\sqrt{3})(.3) = .52$ . These figures demonstrate that the model predicts dilatancy effects generally equivalent to those experimentally observed.

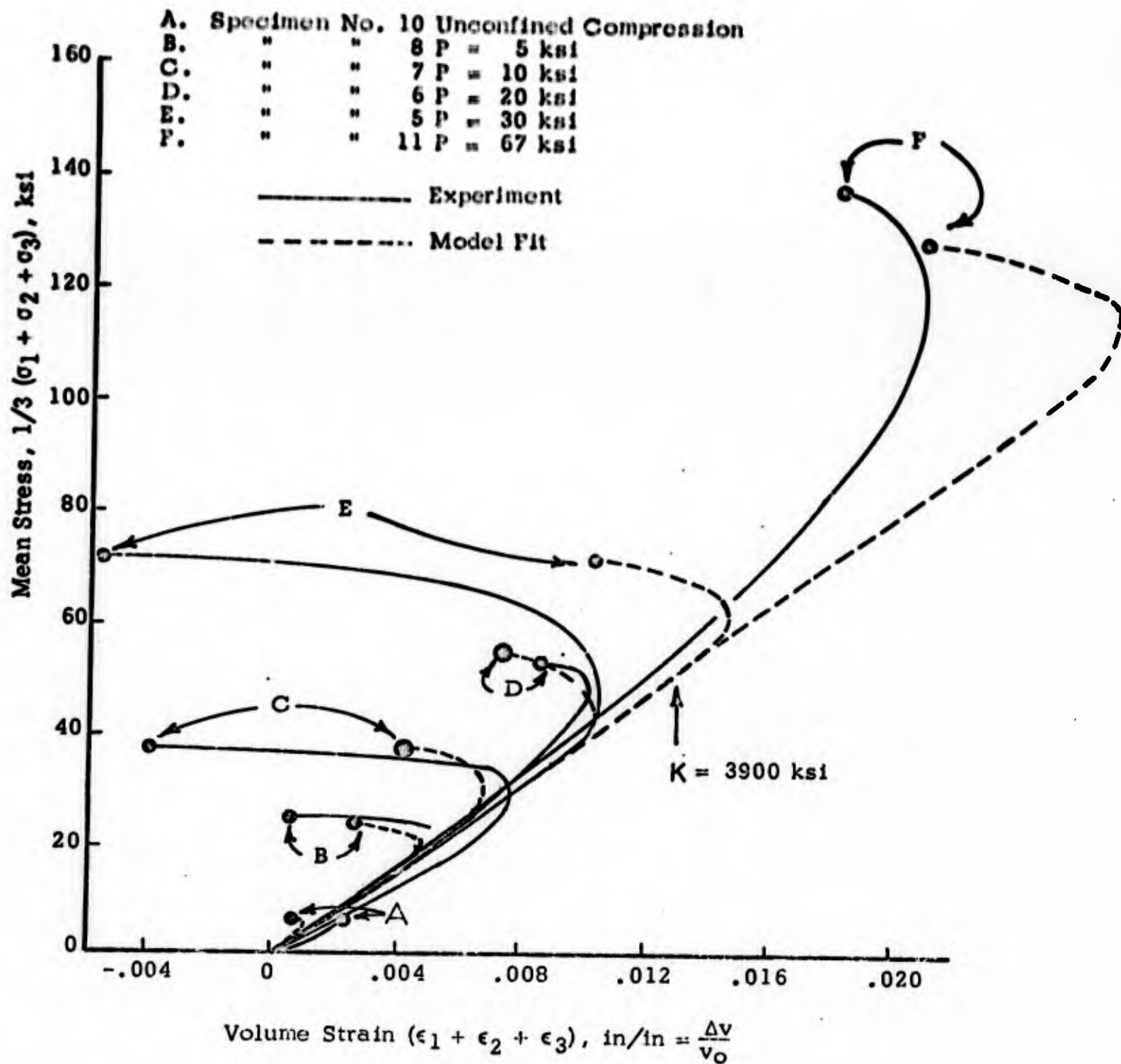


Figure 6. Comparison of Dilatation Stress-Strain Curves for Six-inch Core Cedar City Granite.

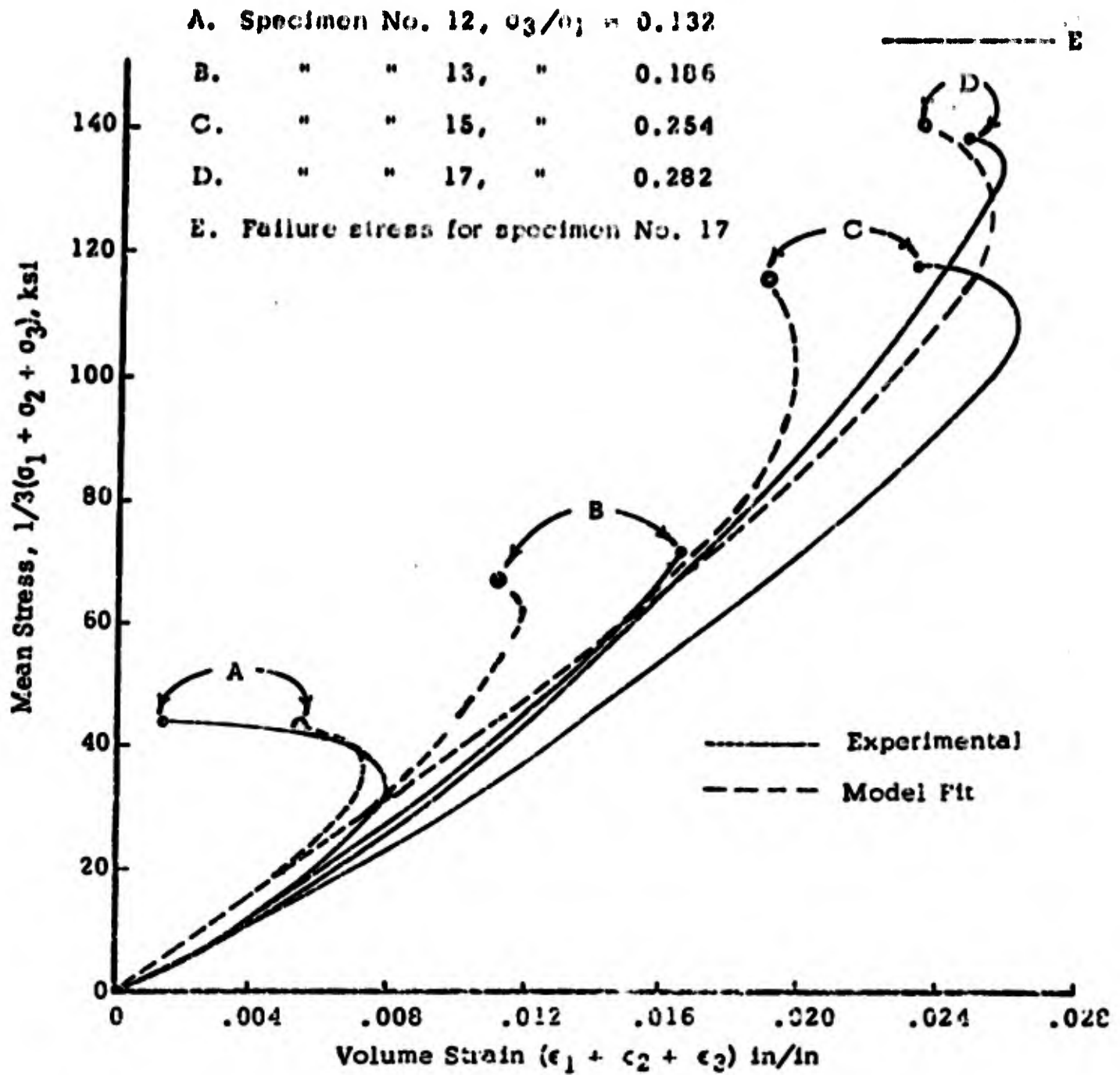


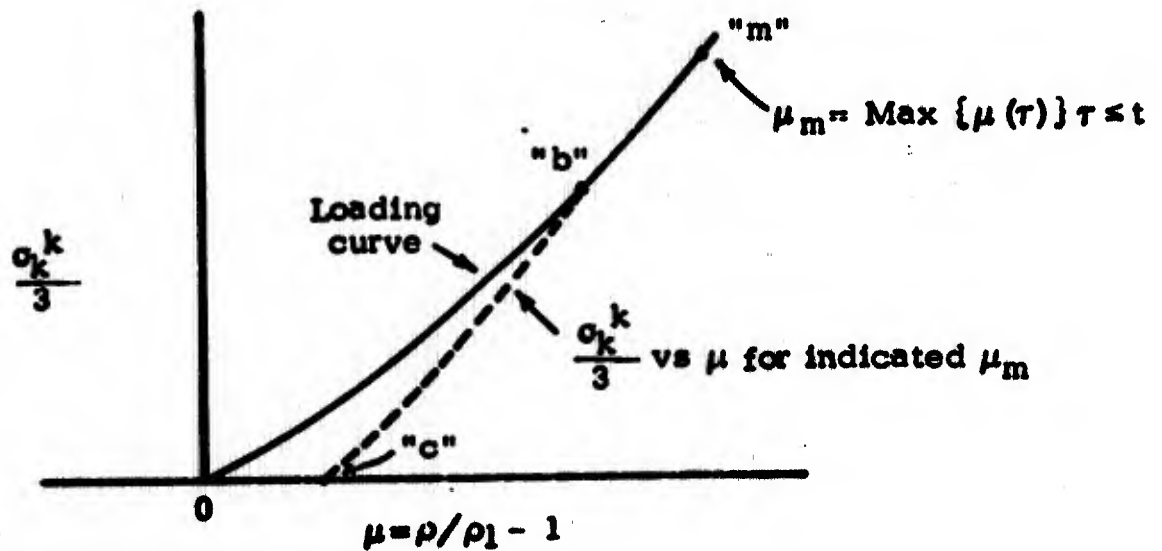
Figure 7. Dilatation Stress-Strain Curves for Six-inch Core Cedar City Granite, Constant Stress Ratio Tests.

Note that the forms used to fit the experimental data of reference 7 must be modified before being applied to problems involving high stresses. For example, specific internal energy effects must be included in  $\pi$ .

#### II-4.1.1 Hysteretic Effects

In Section 4.1, most of the important features of the model were illustrated using experimental data on granite. However, granite exhibits only a small amount of hysteresis at low pressures, and therefore the hysteretic effect was not included in the granite example. A method of including the hysteretic effect into the constitutive relations will now be discussed.

Loosely speaking, the approach permits the mean stress equation of state,  $\sigma/3$  versus  $\rho$  and  $e$ , to vary as a function of the maximum density experienced up to the present time. This concept is illustrated in the following sketch. In the sketch, the compression ( $\mu = \rho/\rho_0 - 1$ ) is used in place of the density, and the effects of internal energy and  $I$  are ignored.

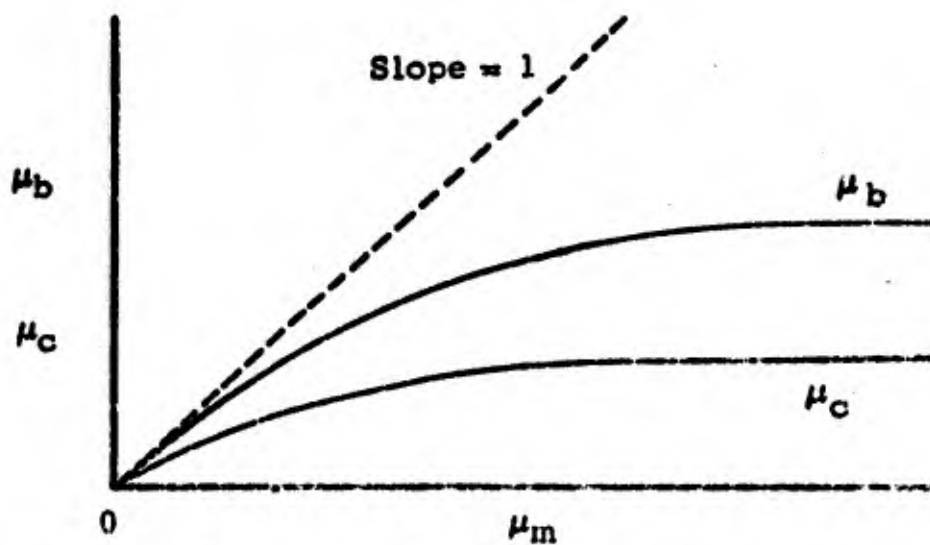


$\frac{\sigma_k}{3} = \pi(\mu, \mu_m)$ , Hysteretic Effect as a Function of Maximum Compression ( $\mu_m$ ) on Material Element.

In the sketch, the loading curve is shown. This curve describes the behavior of the material if only loading is permitted to occur, i.e.,  $\dot{\mu} \geq 0$ . However, once the material element has been loaded, the relationship between  $\sigma_v^j/3$  and  $\mu$  may change for  $\mu < \mu_m$ , where  $\mu_m = \text{Max} \{ \mu(\tau) \} \tau \leq t$  where  $t$  is the present time. An example of the change in the mean stress versus compression relationship is illustrated in the above sketch. The material element was loaded to a maximum compression value of  $\mu_m$  (point "m" on the sketch). As long as this compression value is not exceeded, the dashed curve describes the stress-compression relationship. The new relationship illustrates the irreversible compaction which occurs in hysteretic materials. For example, point "c" on the sketch shows the compaction (as measured by  $\mu$ ) when the mean stress is entirely relaxed. Point "b" on the sketch illustrates the fact that part of the loading curve (between points "m" and "b") may be retraced for the unloading and reloading paths. For small values of  $\mu_m$  the points "m" and "b" may be nearly coincident. However, for very large values of  $\mu_m$ , the points "m" and "b" may be far apart. A large separation of "m" and "b" will occur, in general, after the hysteretic material has essentially reached a completely compacted state.

The approach just outlined appears sufficiently general to fit most of the observed hysteretic characteristics in rocks and soils. The function  $\pi(\mu, \mu_m)$  is chosen to fit the experimental data. A convenient approach for fitting  $\pi(\mu, \mu_m)$  to the data will now be described.

1. From the experimental data, determine the relationship between  $\mu_m$ ,  $\mu_b$ , and  $\mu_c$ .  $\mu_b$  and  $\mu_c$  are the compression values at points "b" and "c" in the above sketch.  $\mu_b$  and  $\mu_c$  are both function of  $\mu_m$ , and the dependence is qualitatively illustrated below.



Qualitative Dependence of  $\mu_b$  and  $\mu_c$  on  $\mu_m$

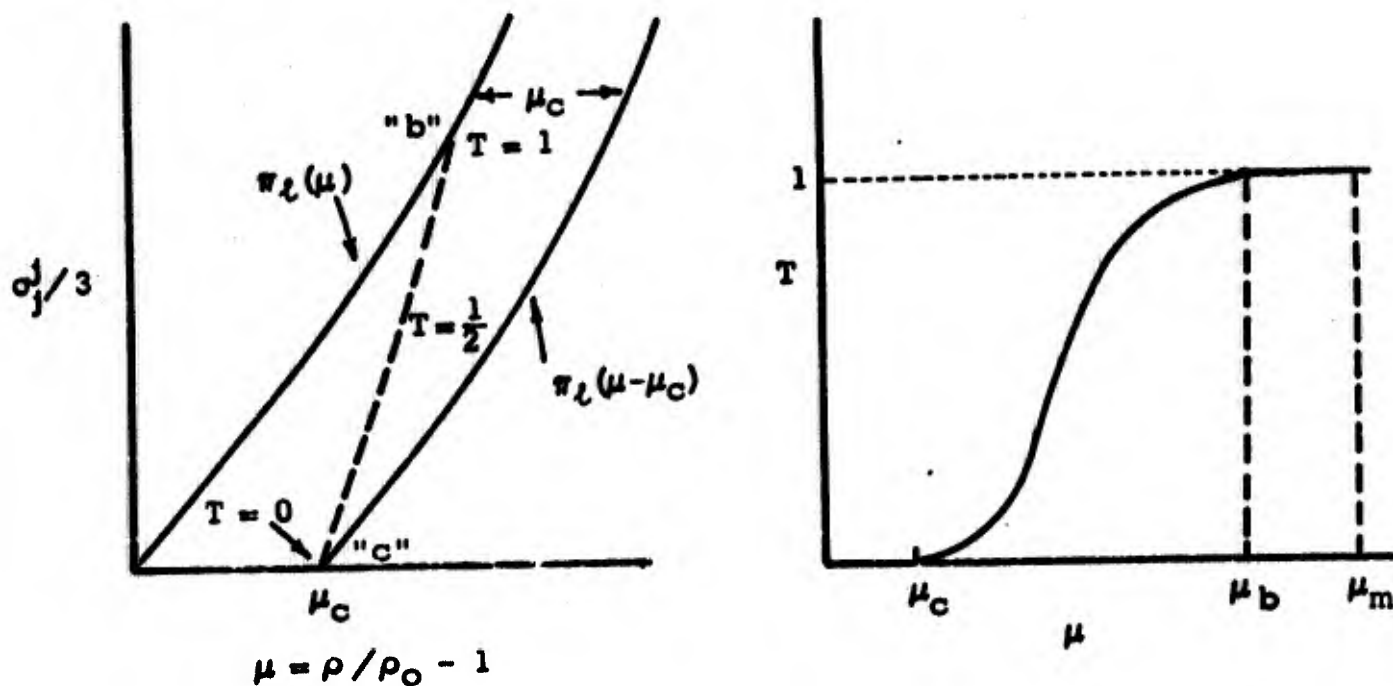
The line with slope 1 corresponds to the condition  $\mu_b = \mu_m$ , i.e., the point "m" and "b" are coincident. The sketch shows that  $\mu_b$  eventually becomes less than  $\mu_m$ .  $\mu_b$  will probably approach an asymptotic value.  $\mu_c$  is, of course, less than  $\mu_b$ .  $\mu_c$  is also expected to have an asymptotic value corresponding to the maximum irreversible compaction upon release to  $\sigma_j^i = 0$ .

2. Find a form,  $\sigma_j^i/3 = \pi(\mu, \mu_m)$  which properly describes the smooth transition between the points "b" and "c". This form must also describe the pure loading curve which corresponds to the condition  $\mu = \mu_m$ .

A possible form for  $\pi(\mu, \mu_m)$  is

$$\pi(\mu, \mu_m) = \pi_L(\mu) T + \pi_L(\mu - \mu_c) [1 - T] \quad (31)$$

where  $\pi_L(\mu)$  is the function describing the loading curve, and  $T$  is a function which goes from 1 to 0, as  $\mu$  goes from  $\mu_b$  to  $\mu_c$ .  $T$  causes a transition to be made from the curve  $\pi_L(\mu)$  to the curve  $\pi_L(\mu - \mu_c)$ . This is illustrated in the following sketch.



Qualitative Illustrations of  $\pi(\mu, \mu_m) = \pi_L(\mu) T + \pi_L(\mu - \mu_c)[1 - T]$  and the Function  $T$ .

Note that the transitional function must satisfy

$$\begin{aligned}
 T &= 0 && \text{for } \mu \leq \mu_c \\
 T &= 1 && \text{for } \mu \geq \mu_b \\
 \frac{\partial T}{\partial \mu} &= 0 && \text{for } \mu = \mu_c \text{ and } \mu = \mu_b
 \end{aligned}
 \tag{32}$$

Also note that  $T$  is only a function of  $\mu$  and  $\mu_m$  since  $\mu_c$  and  $\mu_b$  are known functions of  $\mu_m$ . Detailed investigations of experimental data have not yet been performed to determine  $T$ . An example of an expression for  $T$  which satisfies the conditions of Eqn. (32) is

$$\begin{aligned}
 T &= 0 && \text{for } \mu \leq \mu_c \\
 T &= 1 && \text{for } \mu \geq \mu_b \\
 T &= \sin^2 \left[ \frac{\mu - \mu_c}{\mu_b - \mu_c} \cdot \frac{\pi}{2} \right] && \text{for } \mu_c \leq \mu \leq \mu_b
 \end{aligned}
 \tag{33}$$

The function  $T$  is a mathematical convenience permitting the experimentally observed relationship between  $\mu_c$ ,  $\mu_b$  and  $\mu_m$  to be fit analytically. The form of Eqn. (33) will fit  $\mu_c = \mu_c(\mu_m)$  and  $\mu_b = \mu_b(\mu_m)$  exactly. Whether or not Eqn. (33) gives satisfactory results for the unloading curve between  $\mu = \mu_c$  and  $\mu = \mu_b$  will have to be determined. However, if Eqn. (33) is not satisfactory, another form for  $T$  can be chosen on the basis of the experimental data.

To clarify the approach, two examples will now be described. In the first example, the data of reference 9 (on Solenhofen Limestone at 24.5°C) is used to roughly set the physical scale. In reference 9, a hydrostatic loading and unloading stress-compression path was performed for a peak pressure of 37.4 kb. The corresponding peak compression (point "m") was  $\mu_m = .117$ . Upon unloading it was observed that the residual compression at  $P \approx 0$  was approximately  $\mu_c = .013$  for  $\mu_m = .117$ . Also,  $\mu_b$  was observed to be very close to  $\mu_m$ .

For purposes of illustration, it was assumed that the loading curve satisfied

$$P = \frac{\sigma_j}{3} = \pi_l(\mu) = 180 \mu + 1210 \mu^2 \text{ (kb)}
 \tag{34}$$

and that  $\mu_c$  and  $\mu_b$  are given by

$$\mu_c(\mu_m) = .05 (1 - e^{-4\mu_m}) \quad (35)$$

$$\begin{aligned} \mu_b(\mu_m) &= \mu_m & \mu_m \leq .1 \\ &= .1 + .1 (1 - e^{-10(\mu_m - .1)}) & \mu_m \geq .1 \end{aligned} \quad (36)$$

$\mu_c$  and  $\mu_b$  as functions of  $\mu_m$  are illustrated in Figure 8a. Note that  $\mu_c$  has an asymptotic value of .05 and  $\mu_b$  has an asymptotic value of .2. These values were arbitrarily chosen.

Using these forms for  $\sigma_j/3$ ,  $\mu_c$ , and  $\mu_b$ , the mean stress versus compression behavior is determined from Eqns. (31) and (33). Figure 9 shows several loading and unloading paths for this example. The Limestone data from reference 9 is also included on this graph. But note that no effort was made to accurately simulate the behavior of the Limestone.

Figure 9 shows only a small amount of hysteresis. This is typical of rocks. On the other hand, soils may exhibit a large amount of hysteresis. To illustrate this, consider a hypothetical soil material whose loading curve is given by

$$\pi_L(\mu) = 5\mu + 10\mu^2 \quad (kb) \quad (37)$$

Also assume that  $\mu_c$  and  $\mu_b$  are given by

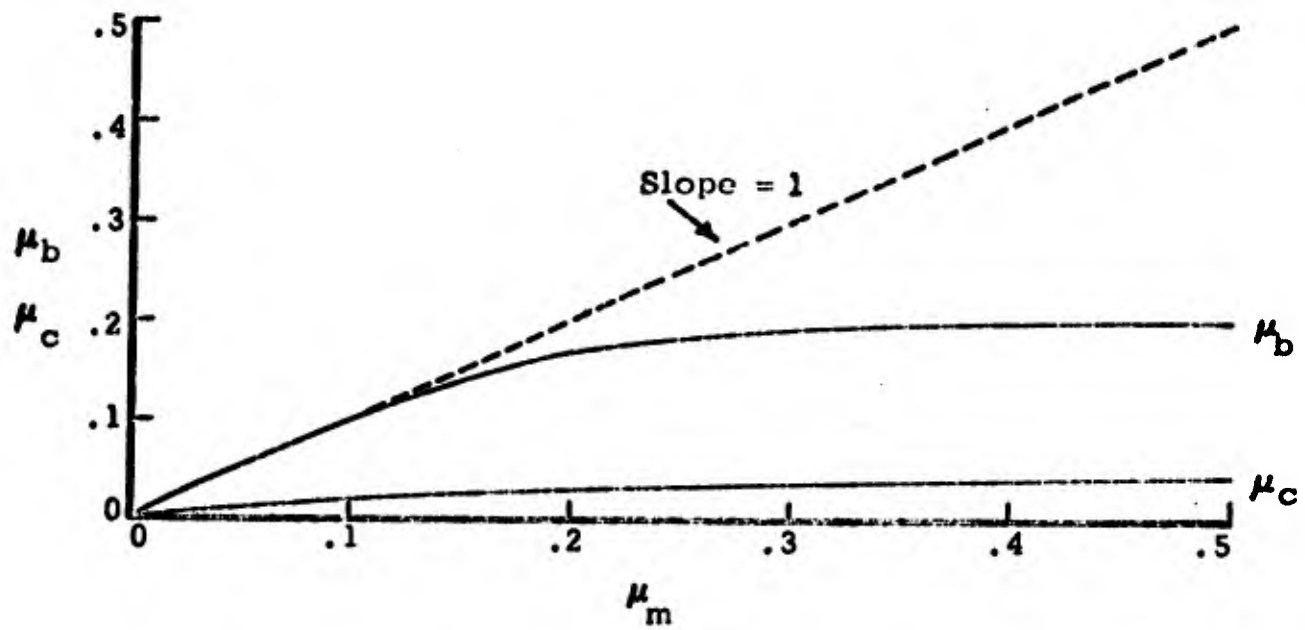
$$\mu_c = .4 (1 - e^{-2.4\mu_m}) \quad (38)$$

$$\mu_b = \mu_m \quad \mu_m \leq .3$$

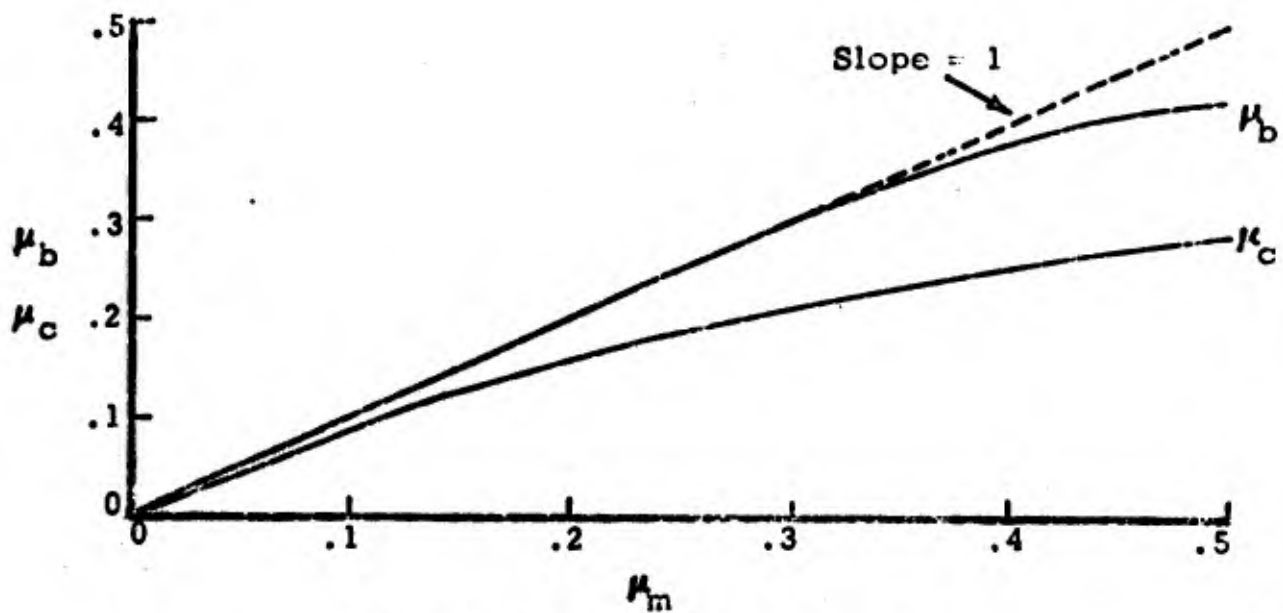
$$= .3 + .2 (1 - e^{-5(\mu_m - .1)})$$

Figure 8b shows  $\mu_c$  and  $\mu_b$  as functions of  $\mu_m$ .

The same form for  $\pi_L$ ,  $\mu_c$ , and  $\mu_b$  are used in the example as was used in the first example. However Figure 10 shows the large hysteresis effect which results in the second example. The reason for the pronounced hysteresis effect is that the asymptotic value of  $\mu_c$  has been set at .4 and  $\frac{\mu_b - \mu_c}{\mu_b}$  has been kept small thereby keeping the recoverable compression relatively small.



Example 1 - "Rock Like" Material



Example 2 - "Soil Like" Material

Figure 8. Two Examples of the Dependence of  $\mu_b$  and  $\mu_c$  on  $\mu_m$ .

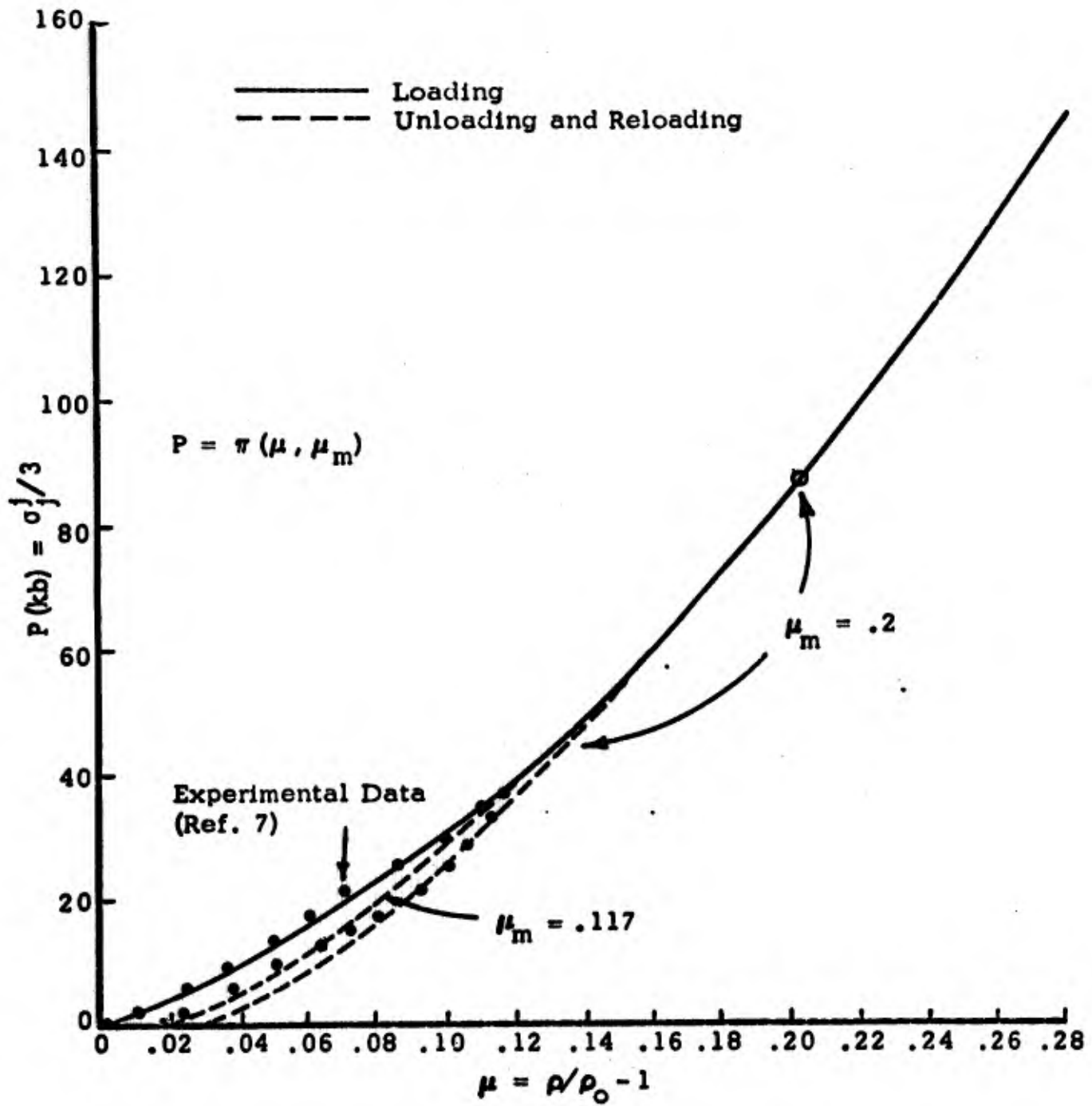


Figure 9. Example 1 of the Hysteretic Effect in a "Rock Like" Material

Finally, note that other forms for  $\mu_c$  and  $\mu_b$  can be chosen to simulate a phase change or a region of rapid transition in the hysteretic characteristics. For example, if the mean stress versus compression behavior is as indicated in Figure 11a, then Figure 11b qualitatively shows the  $\mu_c$  and  $\mu_b$  behavior.

The loading and unloading curves discussed in Sections 4.1 and 4.1.1 ignored the effects of specific internal energy ( $e$ ) on the constitutive properties. At low stress levels, the effects of specific internal energy are small. However, if high stress levels are of interest, the influence of specific internal energy on the constitutive properties must be considered. For example if the material is in a melted state, the shear modulus and shear stresses should nearly vanish. The specific internal energy must also be put into the relationship  $\sigma_j/3 = \pi(\rho, e, I, \rho_m)$  to provide the proper behavior of release adiabats emanating from elevated stress states.

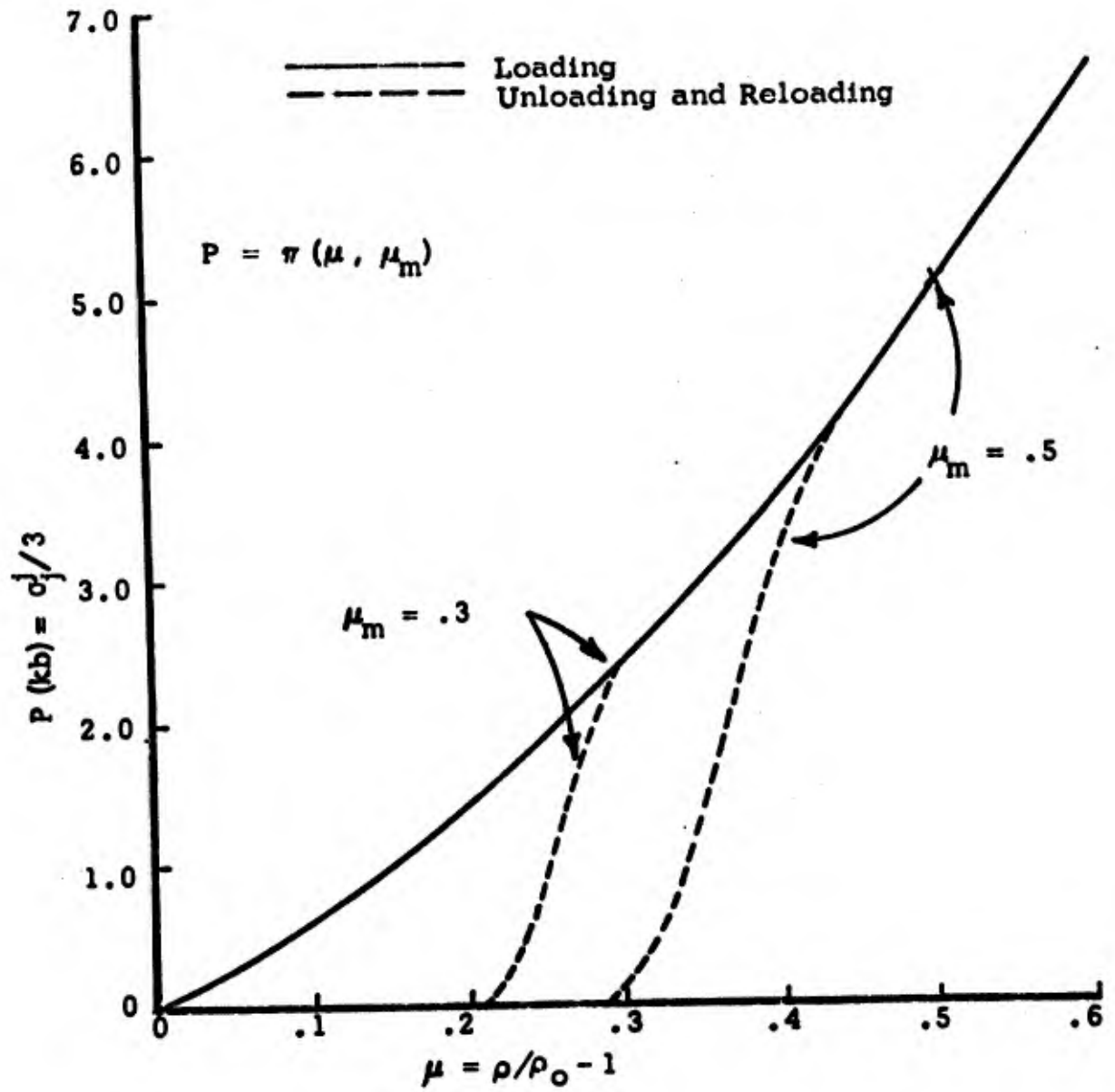


Figure 10. Example 2 of the Hysteretic Effect in a "Soil Like" Material.

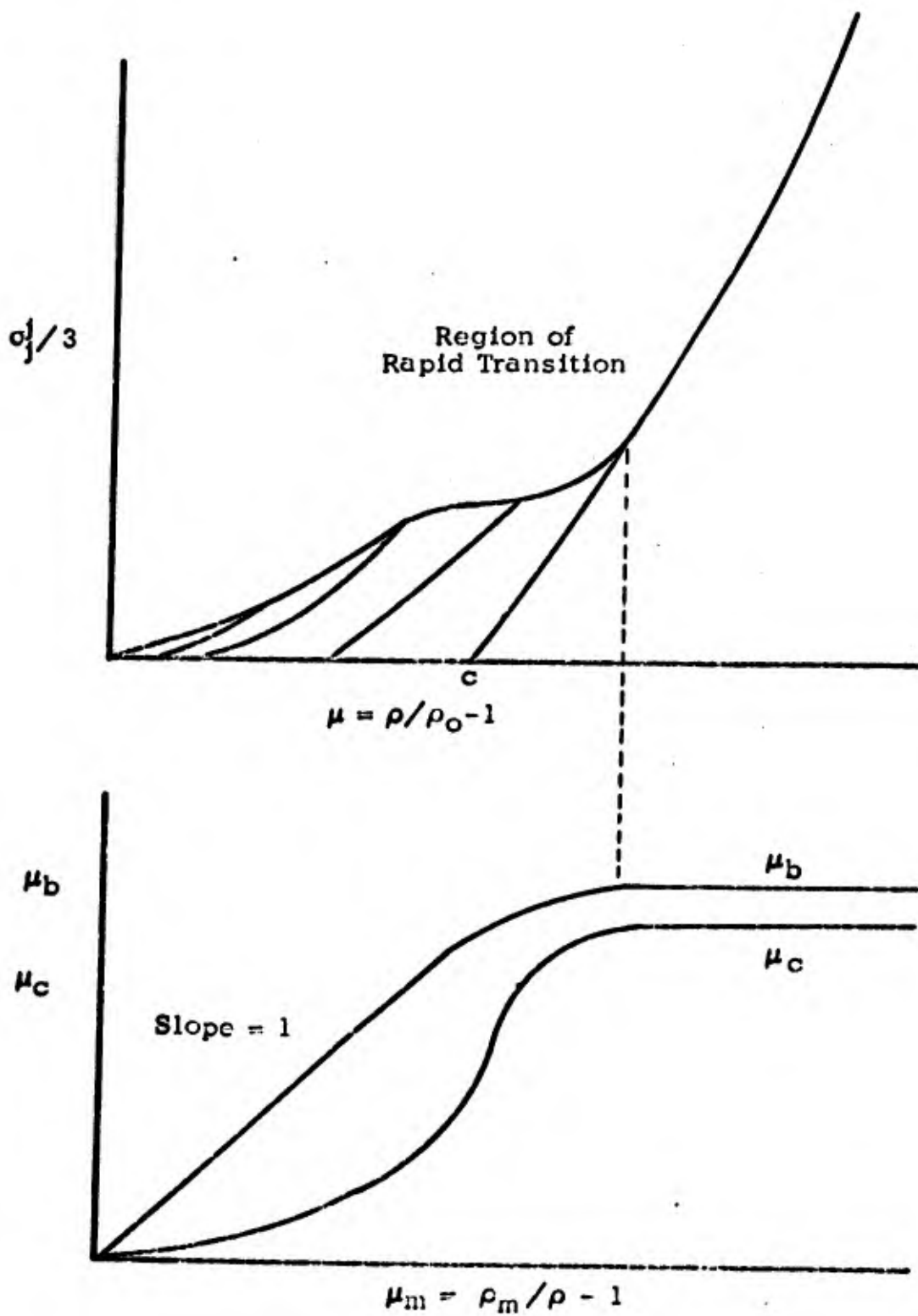


Figure 11. Hypothetical Material with Rapidly Varying Hysteretic Properties.

## II-5. UNIQUENESS OF SOLUTIONS

In this section, we will demonstrate that the differential equations defining the rock and soil model are hyperbolic. The hyperbolic form of the governing differential equations guarantees uniqueness of solution for well-posed boundary value problems. First, a very brief discussion of the method of characteristics will serve to define terminology. (A detailed discussion of the method of characteristics and of systems of hyperbolic differential equations is given in Reference 10.)

A general system of  $k$  first order differential equations in  $k$  dependent variables  $u_j$  with  $n$  independent variables  $x_\alpha$  may be written in the form

$$a_{ij}^\alpha \frac{\partial u_j}{\partial x_\alpha} + b_i \equiv L_i(u_j) = 0 \quad (39)$$

$$i, j = 1, k \text{ and } \alpha = 1, n$$

or in matrix notation

$$A^\alpha \frac{\partial U}{\partial x_\alpha} + B \equiv L(U) = 0 \quad (40)$$

where  $A^\alpha$  are  $k \times k$  matrices  $(a_{ij}^\alpha)$  and the quasi-linear operator  $L$  and  $B$  are vectors. Also,  $X$  will denote the vector  $x_\alpha$ .  $L(U)$  is considered quasi-linear since the coefficients  $A^\alpha$  and  $B$  may depend on  $U$ .

Consider a  $(n-1)$  dimensional surface specified by the equation  $\phi(X) = 0$  with  $|\text{grad } \phi| = \left| \frac{\partial \phi}{\partial x_\alpha} \right| = |\phi_\alpha| \neq 0$ . On this surface we define the characteristic matrix

$$A_{ij} \equiv A = A^\alpha \phi_\alpha \quad (41)$$

and the characteristic determinant or characteristic form

$$Q(\phi_1, \phi_2, \dots, \phi_n) = ||A|| \quad (42)$$

where  $||A||$  is the determinant of  $A$ .

If  $Q(\phi_\alpha) = 0$  on the surface  $\phi = 0$ , then  $\phi = 0$  is a characteristic surface. Also, there exist characteristic linear combinations of the  $L_i$

$$\iota L(U) = \iota^i L_i(u_j) \equiv \Lambda(U) = 0 \quad (43A)$$

such that derivatives of the dependent variables  $U$  need be taken only in the characteristic surface  $\phi = 0$ . Thus  $\Lambda(U) = 0$  establishes a relationship between the initial data, and these data cannot be chosen arbitrarily. (If  $Q \neq 0$ , then  $\phi = 0$  is called a free surface and  $U$  can be chosen arbitrarily on  $\phi = 0$ .)

The vector  $\ell$  in Eqn. (43) is a "left null vector" defined by

$$\ell A = \ell^i A_{ij} = 0 \quad (\text{when } ||A_{ij}|| = Q = 0) \quad (43B)$$

Using this terminology, the conditions for Eqns. (39) to be hyperbolic can now be defined. Equations (39) are hyperbolic if for arbitrarily prescribed values of  $\phi_1, \phi_2, \dots, \phi_{n-1}$  (assuming  $\phi_n \neq 0$ ),

- a) there exists  $k$  real roots for  $\phi_n$  in the determinant  $Q = 0$ , and
- b) there exist  $k$  linearly independent left null vectors  $\ell_1, \ell_2, \dots, \ell_k$

which satisfy Eqn. (43).

Note that if the  $k$  real roots mentioned above are distinct, then the system of differential equations are called "totally hyperbolic" because the existence of  $k$  linearly independent left null vectors is guaranteed (i.e., one null vector for each of the distinct roots of  $Q = 0$ ). However, if there are multiple roots, a more detailed examination of the existence of independent null vectors is necessary. In particular, consider

$$Q(\phi_1, \dots, \phi_n) = (Q_A)^s Q_B = 0 \quad (44)$$

where  $Q_A$  is a form containing  $\phi_n$ , and  $Q_B = 0$  contains  $k-s$  real and distinct roots for  $\phi_n$ . Then, the system of partial differential equations will be hyperbolic if  $s$  linearly independent left null vectors can be found for the condition  $Q_A = 0$ .

For the rock and soil model, the determinant  $Q(\phi_1, \phi_n)$  was explicitly calculated for the two dimensional planar case. (This case is sufficiently general to illustrate the important features of the model).  $Q = 0$  does have the multiple solution form of Eqn. (44) and therefore the left null vectors corresponding to  $Q_A$  were explicitly determined. A summary of the calculations will now be presented.

The constitutive relations (Eqns. (1) and (2) in Section 2) can be combined as follows:

$$\dot{\sigma}_1^j = 2G d_1^j + (\dot{\nu} - \frac{2}{3} G d_\beta^\beta) \delta_1^j - \gamma \bar{\phi} (F) \frac{\sigma_1^{j*}}{\sqrt{J_2^{\prime\prime}}} \quad (45)$$

If we put all the terms containing derivatives of the dependent variables on the left, then Eqn. (45) becomes

$$\begin{aligned} \dot{\sigma}_1^j + \sigma_1^k \omega_k^j - \omega_1^k \sigma_k^j \\ - 2G d_1^j - (\pi_\rho \dot{\rho} + \pi_e \dot{e} - \frac{2}{3} G d_\beta^\beta) \delta_1^j = \gamma \bar{\phi} \frac{\sigma_1^{j*}}{\sqrt{J_2^{\prime\prime}}} + \pi_1 \gamma \bar{\phi} \delta_1^j \end{aligned} \quad (46)$$

where the dot denotes the material time derivative and

$$\pi_\rho = \frac{\partial \pi}{\partial \rho}, \quad \pi_e = \frac{\partial \pi}{\partial e}, \quad \text{and} \quad \pi_1 = \frac{\partial \pi}{\partial I}$$

The fact that  $\dot{I}_1 = \gamma \phi$  has been used to eliminate the time derivative in the term  $\pi_1 \dot{I}_1 \delta_1^j$ . Also, note that  $\pi_{\rho_m} \dot{\rho}_m = 0$  due to either

$$\dot{\rho}_m = 0, \quad \text{for } \rho < \rho_m$$

or

$$\pi_{\rho_m} = 0, \quad \text{for } \rho = \rho_m \text{ (see Eqns. (31))}$$

Note that the left hand side of the constitutive relations (Eqn. (46)) are in a form similar to that of linear elasticity. The expression  $\pi_\rho \dot{\rho} + \pi_e \dot{e}$  is somewhat analogous to  $K d_\beta^\beta$  where  $K$  is the bulk modulus in elasticity theory. The inelastic behavior of the model is included in terms which do not contain any derivatives and therefore do not affect the characteristic form  $Q = 0$ . Also, it is important to note that Eqns. (46) are valid in both the elastic and inelastic regime. In classical elastic-plastic theory, different constitutive equations are used for the elastic and inelastic regimes.

The complete set of partial differential equations is obtained once the conservation of momentum, mass, and energy are added to the constitutive Eqns. (46). The complete set is recorded in Table 1. In these equations, the engineering convention of  $\sigma > 0$  implying compression has been used.

TABLE 1. COMPLETE SET OF GOVERNING DIFFERENTIAL EQUATIONS FOR THE ROCK AND SOIL MODEL IN 2-D PLANAR GEOMETRY.

$$1) \quad \frac{\partial \sigma_{11}}{\partial t} + u \frac{\partial \sigma_{11}}{\partial x} + v \frac{\partial \sigma_{11}}{\partial y} - \sigma_{12} \frac{\partial u}{\partial y} + \sigma_{12} \frac{\partial v}{\partial x} + \frac{4}{3} G \frac{\partial u}{\partial x}$$

$$- \frac{2}{3} G \frac{\partial v}{\partial y} - \pi_{\rho} \left[ \frac{\partial \rho}{\partial t} + u \frac{\partial \rho}{\partial x} + v \frac{\partial \rho}{\partial y} \right] - \pi_e \left[ \frac{\partial e}{\partial t} + u \frac{\partial e}{\partial x} + v \frac{\partial e}{\partial y} \right] = b_1$$


---

$$2) \quad \frac{\partial \sigma_{22}}{\partial t} + u \frac{\partial \sigma_{22}}{\partial x} + v \frac{\partial \sigma_{22}}{\partial y} + \sigma_{12} \frac{\partial u}{\partial y} - \sigma_{12} \frac{\partial v}{\partial x} + \frac{4}{3} G \frac{\partial v}{\partial y}$$

$$- \frac{2}{3} G \frac{\partial u}{\partial x} - \pi_{\rho} \left[ \frac{\partial \rho}{\partial t} + u \frac{\partial \rho}{\partial x} + v \frac{\partial \rho}{\partial y} \right] - \pi_e \left[ \frac{\partial e}{\partial t} + u \frac{\partial e}{\partial x} + v \frac{\partial e}{\partial y} \right] = b_2$$


---

$$3) \quad \frac{\partial \sigma_{12}}{\partial t} + u \frac{\partial \sigma_{12}}{\partial x} + v \frac{\partial \sigma_{12}}{\partial y} + \left( \frac{\sigma_{11} - \sigma_{22}}{2} \right) \frac{\partial u}{\partial y} - \left( \frac{\sigma_{11} - \sigma_{22}}{2} \right) \frac{\partial v}{\partial x} + G \frac{\partial u}{\partial y} + G \frac{\partial v}{\partial x} = b_3$$


---

$$4) \quad \frac{\partial \sigma_{11}}{\partial x} + \frac{\partial \sigma_{12}}{\partial y} + \rho \frac{\partial u}{\partial t} + \rho u \frac{\partial u}{\partial x} + \rho v \frac{\partial u}{\partial y} = 0$$


---

$$5) \quad \frac{\partial \sigma_{21}}{\partial x} + \frac{\partial \sigma_{22}}{\partial y} + \rho \frac{\partial v}{\partial t} + \rho u \frac{\partial v}{\partial x} + \rho v \frac{\partial v}{\partial y} = 0$$


---

$$6) \quad \frac{\partial \rho}{\partial t} + u \frac{\partial \rho}{\partial x} + v \frac{\partial \rho}{\partial y} + \rho \frac{\partial u}{\partial x} + \rho \frac{\partial v}{\partial y} = 0$$


---

$$7) \quad \rho \frac{\partial e}{\partial t} + \rho u \frac{\partial e}{\partial x} + \rho v \frac{\partial e}{\partial y} + \sigma_{11} \frac{\partial u}{\partial x} + \sigma_{12} \frac{\partial u}{\partial y} + \sigma_{12} \frac{\partial v}{\partial x} + \sigma_{22} \frac{\partial v}{\partial y} = 0$$


---

$$8) \quad \frac{\partial I}{\partial t} + u \frac{\partial I}{\partial x} + v \frac{\partial I}{\partial y} = b_8$$


---

TABLE 2. CHARACTERISTIC MATRIX  $A_{ij} = A_{ij}^{\alpha} \phi_{\alpha}$  FOR ROCK AND SOIL MODEL.

$$A_{ij} = \begin{pmatrix} \dot{\phi} & 0 & 0 & 4/3G \phi_1 & -2/3G \phi_2 & -\pi_{\rho} \dot{\phi} & -\pi_e \dot{\phi} & 0 \\ 0 & \dot{\phi} & 0 & -2/3G \phi_1 & 4/3G \phi_2 & -\pi_{\rho} \dot{\phi} & -\pi_e \dot{\phi} & 0 \\ 0 & 0 & \dot{\phi} & (G+\tau) \phi_2 & (G-\tau) \phi_1 & 0 & 0 & 0 \\ \phi_1 & 0 & \phi_2 & \rho \dot{\phi} & 0 & 0 & 0 & 0 \\ 0 & \phi_2 & \phi_1 & 0 & \rho \dot{\phi} & 0 & 0 & 0 \\ 0 & 0 & 0 & \rho \phi_1 & \rho \phi_2 & \dot{\phi} & 0 & 0 \\ 0 & 0 & 0 & \sigma_{11} \phi_1 & \sigma_{22} \phi_2 & 0 & \rho \dot{\phi} & 0 \\ 0 & 0 & 0 & 0 & 0 & 0 & 0 & \dot{\phi} \end{pmatrix}$$

The dependent variables form the 8 component vector

$$U = \begin{pmatrix} \sigma_{11} \\ \sigma_{22} \\ \sigma_{12} \\ u \\ v \\ \rho \\ e \\ I \end{pmatrix} = u_j$$

The independent variables are ordered

$$x_\alpha = (t, x, y), \alpha = 0, 1, 2$$

and the following notation is used

$$\phi_0 = \frac{\partial \phi}{\partial t}, \phi_1 = \frac{\partial \phi}{\partial x}, \phi_2 = \frac{\partial \phi}{\partial y} \quad \text{and} \quad (47)$$

$$\dot{\phi} = \phi_0 + \phi_1 u + \phi_2 v$$

Then, the 8x8 matrix  $A = A^\alpha \phi_\alpha$  is given in Table 2. In this table we have assumed, without any loss in generality, that the coordinate system is oriented so that  $\sigma_{12} = 0$  at the typical point  $(t, x, y)$  under investigation.

The determinant of A is the characteristic form, Q. Q is given by

$$Q = \rho^3 (Q_A)^4 Q_B$$

where

$$Q_A = \dot{\phi}$$

$$Q_B = \{ \dot{\phi}^2 - [(C_{D1})^2 \phi_1^2 + (C_{D2})^2 \phi_2^2] \} \{ \dot{\phi}^2 - [(C_{S1})^2 \phi_1^2 + (C_{S2})^2 \phi_2^2] \}$$

$$= \{ \quad \}_D \{ \quad \}_S$$

where

$$\begin{aligned}
 (C_{D1})^2 &= \pi_\rho + \frac{\sigma_{11} \pi_e}{\rho^2} + 4/3 G/\rho \\
 (C_{D2})^2 &= \pi_\rho + \frac{\sigma_{22} \pi_e}{\rho^2} + 4/3 G/\rho \\
 (C_{S1})^2 &= \frac{G - (\frac{\sigma_{11} - \sigma_{22}}{2})}{\rho} \quad (o > 0 \rightarrow \text{compression}) \\
 (C_{S2})^2 &= \frac{G + (\frac{\sigma_{11} - \sigma_{22}}{2})}{\rho}
 \end{aligned} \tag{48}$$

The form for  $Q = 0$  shows a multiplicity of 4 in  $Q_A = 0$ , and the existence of 4 real and distinct roots in  $Q_B = 0$ . (We assume  $C_{D1}$ ,  $C_{D2}$ ,  $C_{S1}$ , and  $C_{S2}$  are real.) Therefore to complete the proof, we must show that when  $Q_A = 0$ , there exists four independent left null vectors such that

$$\iota A = 0. \tag{49}$$

Four independent vectors satisfying Eqn. (49) when  $Q_A = 0$  ( $\dot{\phi} = 0$ ) are

$$\begin{aligned}
 \iota_1 &= (0, 0, 0, -\frac{2}{3} \frac{G}{\rho}, 1, 1, 0, 0) \\
 \iota_2 &= (0, 0, -2G, 0, 2\sigma_{11} + \sigma_{22}, 2\sigma_{22} + \sigma_{11}, 0, 0) \\
 \iota_3 &= (0, 0, 0, -\frac{2}{3} G \phi_1^2 (G - \tau) - \frac{4}{3} G \phi_2^2 (G + \tau), 0, \\
 &\quad -\rho(G - \tau) \phi_1^2 + \rho(G + \tau) \phi_2^2, 2G\rho \phi_1 \phi_2, 0) \\
 \iota_4 &= (0, 0, 0, 0, 0, 0, 0, 1)
 \end{aligned} \tag{50}$$

These left null vectors are applicable along a material streamline, i.e.,  $\dot{\phi} = 0$ . The explicit calculation of  $Q$  and the  $\iota_1$ ,  $\iota_2$ ,  $\iota_3$ , and  $\iota_4$  complete the demonstration of the hyperbolic nature of the model. Before concluding however, a few remarks should be made concerning the expression for  $Q_B$ .

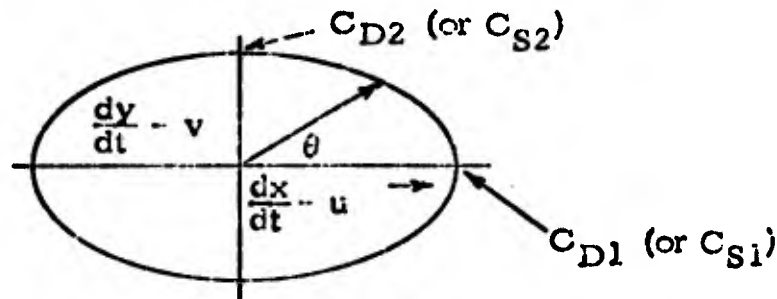
The expression  $Q_B = 0$  supplies 4 real and distinct solutions for  $\phi_0$  given  $\phi_1$  and  $\phi_2$ . Therefore,  $Q_B = 0$  furnishes 4 linearly independent left null vectors,  $\iota$ . Two solutions are obtained from each of the bracketed expressions in  $Q_B$ . The bracketed expressions are analogous to the dilatational and shear wave characteristic forms obtained in linear elasticity. However, the wave velocities are now directionally dependent if  $\sigma_{11} \neq \sigma_{22}$ . Explicitly,  $\{ \ }_D = 0$  implies the following "propagation velocity" relationship.

$$\frac{\left(\frac{dx}{dt} - u\right)^2}{(C_{D1})^2} + \frac{\left(\frac{dy}{dt} - v\right)^2}{(C_{D2})^2} = 1 \quad (51)$$

The expression  $\{ \ }_S$  implies.

$$\frac{\left(\frac{dx}{dt} - u\right)^2}{(C_{S1})^2} + \frac{\left(\frac{dy}{dt} - v\right)^2}{(C_{S2})^2} = 1 \quad (52)$$

Equations (51) and (52) are illustrated in the following sketch.



Propagation Velocity Diagram Assuming  $\sigma_{11} \neq \sigma_{22}$  and  $\sigma_{12} = 0$ .

The sketch illustrates that the dilatational wave velocity relative to the moving material is given by

$$C_D(\theta) = \sqrt{C_{D1}^2 \cos^2 \theta + C_{D2}^2 \sin^2 \theta}$$

where  $\theta$  is the angle between the propagation direction and the x axis, and  $C_{D1}$  and  $C_{D2}$  are given in Eqn. (48).

The directional dependence of the wave velocity in the dilatational wave is due to the energy dependence included in  $\pi$ , and the directional dependence in the shear wave is due to the objective stress rate included in the constitutive relationship. The variation of the propagation velocities (if  $\sigma_{11} \neq \sigma_{22}$ ) with direction is expected to be present in most, if not all, models which account for internal energy effects and the principle of objectivity. However, this variation with direction will be small for the physical problems of interest.

II-6. TABLE OF SYMBOLS FOR PART II

$d_{ij}$	deformation rate tensor
$e$	specific internal energy
$F$	material function describing the relationship between current $J'_2$ and maximum static $J'_2$
$g$	a material function which controls the amount of inelastic deformation which the material experiences as the static failure surface is approached
$G$	shear modulus
$H$	material function describing the static failure surface, $\sigma_1 - \sigma_3 = H(P, \sigma_2)$
$I$	generalized inelastic strain measure ( $I = \int_0^t \dot{I}(\tau) d\tau$ )
$\dot{I}$	generalized inelastic deformation rate measure
$\bar{I}$	$\sqrt{3} I$
$\text{In}d_{ij}$	inelastic portion of the deformation rate
$J'_2$	second invariant of the deviatoric stress tensor
$K$	bulk modulus
$P$	mean stress
$t$	time
$T$	transitional function for describing hysteretic materials
$\alpha$	a measure of the proximity of the current state of stress to the static failure surface
$\beta$	dilatancy material constant
$\gamma$	material constant related to the rate sensitive material properties (dimensions of $[\frac{1}{\text{time}}]$ )

$\epsilon_{ij}$	infinitesimal strain tensor
$\epsilon_1, \epsilon_2, \epsilon_3$	principal strain components
$\mu$	compression ( $\rho/\rho_0 - 1$ )
$\pi$	material function which is analogous to a hydrodynamic equation of state, $P = \pi(\rho, e, I, \rho_m)$
$\rho$	density
$\rho_m$	maximum element density experienced up to the present time
$\sigma_{ij}$	stress tensor
$\sigma_1, \sigma_2, \sigma_3$	principal stress components ( $\sigma_1 \geq \sigma_2 \geq \sigma_3$ )
$\overset{\Delta}{\sigma}_{ij}$	Jaumann definition of objective stress rate
$\tau$	dummy time variable, $\tau \leq t$
$\bar{\phi}$	material function controlling the rate of inelastic deformation when $F > 0$
$\omega_{ij}$	spin tensor

II-7. REFERENCES FOR PART II

1. Perzyna, P., "The Constitutive Equations for Rate Sensitive Plastic Materials," Quart. Appl. Math., Vol. 20, No. 4, 1963.
2. Perzyna, P., "On Thermodynamic Foundations of Viscoplasticity," Mechanical Behavior of Materials Under Dynamic Loads, Edited by U. S. Lindholm, Springer-Verlag, 1968.
3. Prager, W., "An Elementary Discussion of Definitions of Stress Rate," Quart. Appl. Math., Vol. 18, No. 4, 1961.
4. Green, S. J., Perkins, R. D., "Uniaxial Compression Tests at Strain Rates from  $10^{-4}$ /sec. to  $10^4$ /sec on Three Geological Materials," General Motors MSL-68-6, April 1968.
5. Perkins, R. D., Green, S. J., "Uniaxial Stress Behavior of Porphyritic Tonalite at Strain Rates to  $10^3$ /sec," General Motors MSL-68-42, February 1969.
6. Rosenblatt, M., "Analytical Study of Strain Rate Effects in Hypervelocity Impacts," Shock Hydrodynamics, Inc., NASA Final Report CR-61323, January 1970.
7. Swanson, R. S., "Development of Constitutive Equations for Rocks," Ph.D. Dissertation at the University of Utah, December 1969.
8. Handin, J., Heard, H. C., Magouick, J. N., "Effect of the Intermediate Principal Stress on Failure in Limestone, Dolomite, and Glass," Journal of Geophysical Research, January 1967.
9. LaMori, P. N., "Compressibility of Three Rocks, (A) Westerly Granite and Solenhofen Limestone to 40 kbar and  $300^{\circ}\text{C}$ , (b) Cedar City Tonalite to 40 kbar at Room Temperature," Proceedings: Strategic Structures Research, Vulnerability/Hardening Long Range Planning Meeting, Volume I, DASA 2288-1, June 1969.
10. Courant, R., "Methods of Mathematical Physics," Vol. II, Interscience Publishers, 1962.

**BLANK PAGE**

**PART III**  
**FRACTURE MODEL FOR ROCKS**  
by M. Rosenblatt and S. Timurtas

**III-1. INTRODUCTION**

Experimental rock failure data cannot generally be fit by the models which are commonly used for metals. The difficulty is illustrated by the observation that triaxial extension\* failure data for rocks fall on a different curve than triaxial compression\* failure data in maximum shear stress vs pressure plots. The familiar von Mises, Prager-Drucker, and Tresca models, on the other hand, require that both sets of such data fall on a single curve.

If the percentage difference between the compression and extension data is small, as may be the case at high pressures, then a simple form relating maximum shear stress,  $\frac{\sigma_1 - \sigma_3}{2}$ , to pressure can be satisfactory.

However, at low pressures the percentage difference can be quite significant, and in these cases the distinction between failure under compression vs extension loading should be explicitly accounted for.

The separation between triaxial compression and extension data for rocks is typified by the plot in Figure 1. The limestone data shown cannot adequately be fit by one curve. The two curves which are plotted on Figure 1 were obtained through the use of a modified Coulomb model developed in this study and discussed in Section 3.2

Some investigators have chosen to fit the experimental data using invariants. In the current study, we chose instead to characterize the fracture surface in terms of the principal stresses. More precisely, we use a rotation of the principal axes to obtain a rotated stress space in which the mean stress (pressure) is proportional to one coordinate and the maximum shear stress ( $\frac{\sigma_1 - \sigma_3}{2}$ ) is proportional to another coordinate. The third coordinate is therefore determined. This rotated stress space is convenient for the comparison of data with physical models. For example, the von Mises yield condition in the rotated stress states will be a circle and the Tresca condition will be a hexagon.

In Section 2, the rotated stress space is mathematically defined. In Section 3, limestone failure data, which include triaxial compression, triaxial extension, and torsion loading are fit in the rotated stress space. In the current study, only limestone data were fit because insufficient data exist for other materials in the intermediate region between triaxial compression and triaxial extension. However, the results of the present study indicate a way to extrapolate to other rocks using only triaxial compression and triaxial extension data.

---

\*Triaxial compression will be defined herein as  $\sigma_1 > \sigma_2 = \sigma_3$ , triaxial extension as  $\sigma_1 = \sigma_2 > \sigma_3$ .  $\sigma_1$ ,  $\sigma_2$ , and  $\sigma_3$  are the principal stresses and  $\sigma > 0$  implies compression.

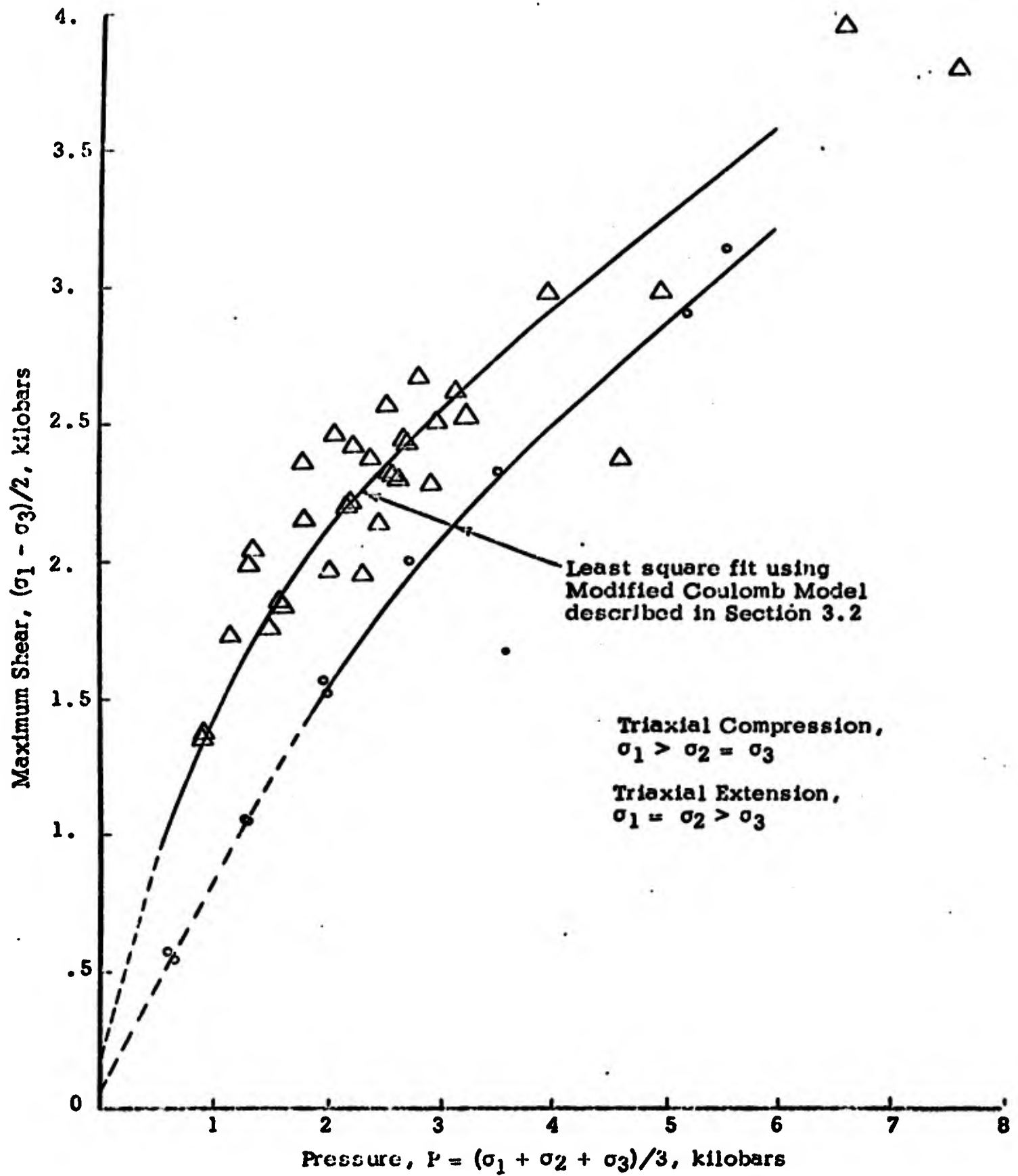


Figure 1. Triaxial Compression and Extension Failure Data For Solenhofen Limestone (from Ref. 1)\*.

\*Reference list for Part III is on page 102.

### III-2. MATHEMATICAL DESCRIPTION OF THE ROTATED PRINCIPAL STRESS SPACE

It is assumed that failure conditions for rocks can be characterized by a surface in principal stress space. Figure 2 shows an example of a possible failure surface which is a surface of revolution about the (1,1,1) line in  $(\sigma_1, \sigma_2, \sigma_3)$  principal stress space. This line, of course, corresponds to  $\sigma_1 = \sigma_2 = \sigma_3$ , and points on the line are in pure hydrostatic pressure. In general, pure hydrostatic pressure will not cause failure or yielding and thus the line defining hydrostatic pressure is expected to be within the failure surface.

In  $(\sigma_1, \sigma_2, \sigma_3)$  principal stress space, any plane which is normal to the (1,1,1) line defines conditions causing constant pressure or mean stress (i.e.,  $P = \frac{\sigma_1 + \sigma_2 + \sigma_3}{3}$ ). The intersection of such a plane of constant pressure with a representative failure surface illustrated in Figure 2 is a circle. The distance in a constant pressure plane from the pure pressure line (1,1,1), or  $\sigma_1 = \sigma_2 = \sigma_3$ , to the failure surface is proportional to the second invariant of the deviatoric stress.

Because of the physical importance of the  $\sigma_1 = \sigma_2 = \sigma_3$  line, it is convenient to rotate principal stress space so that this line becomes one of the new coordinate axes. To define the other axes, we use a rotational transformation by which one new stress coordinate is established as being proportional to the maximum shear stress,

$$y = (\sigma_1 - \sigma_3) / \sqrt{2} \quad (1a)$$

Making this specification, the other stress coordinate for the rotated system becomes

$$x = (\sigma_1 - 2\sigma_2 + \sigma_3) / \sqrt{6} \quad (1b)$$

The coordinate along the  $\sigma_1 = \sigma_2 = \sigma_3$  line is

$$z = \sqrt{3} P = (\sigma_1 + \sigma_2 + \sigma_3) / \sqrt{3} \quad (1c)$$

The x, y, and z coordinate lines are shown relative to the  $\sigma_1, \sigma_2,$  and  $\sigma_3$  axes in Figure 2b. Their direction cosines are given by:

$$x = \frac{1}{\sqrt{6}} (1, -2, 1)$$

$$y = \frac{1}{\sqrt{2}} (1, 0, -1)$$

$$z = \frac{1}{\sqrt{3}} (1, 1, 1)$$

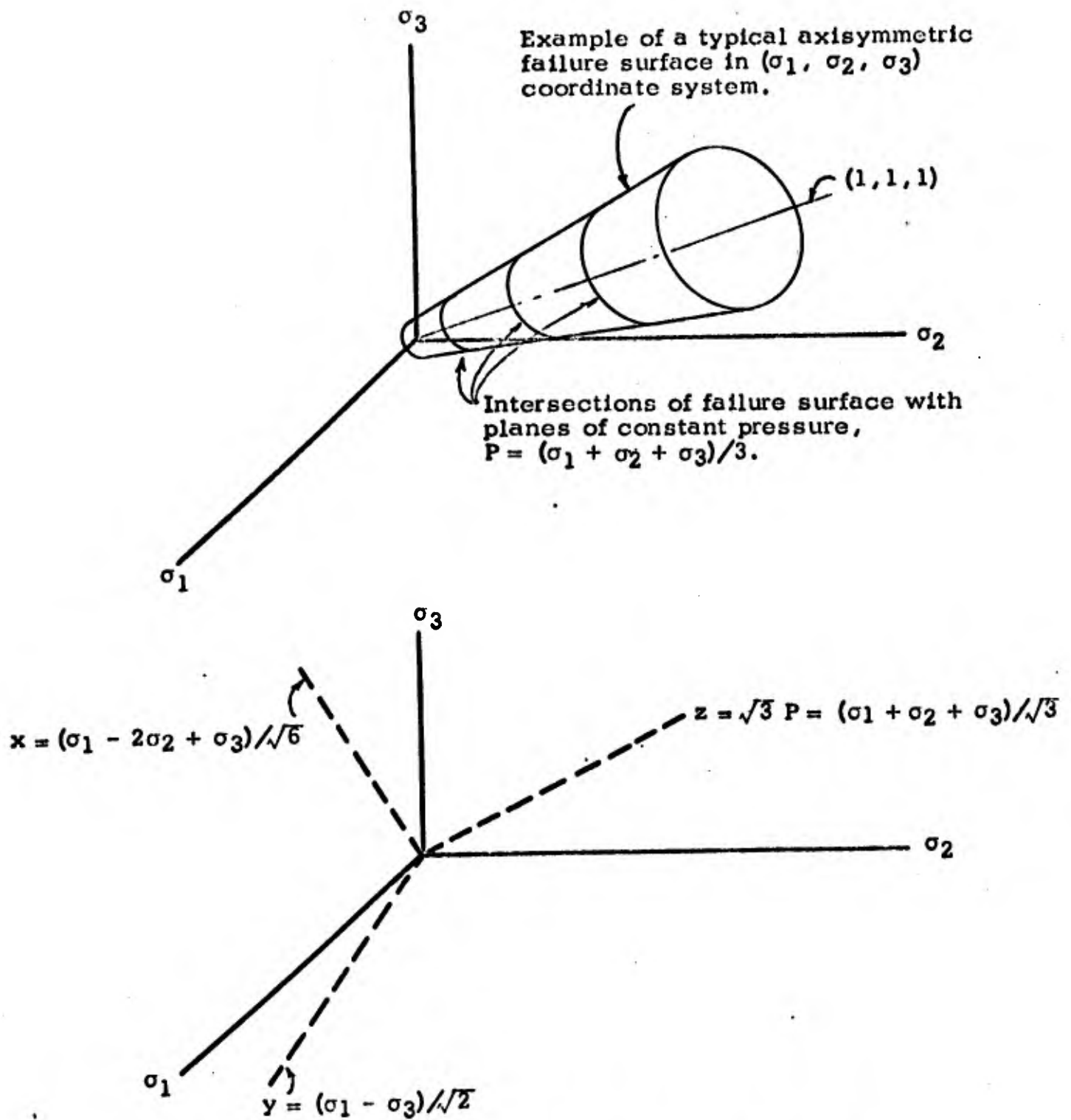


Figure 2. Relative Orientations of the  $(\sigma_1, \sigma_2, \sigma_3)$  and the Rotated  $(x, y, z)$  Coordinate Systems.

Figure 3a shows the rotated stress system. The failure surface previously illustrated in the principal stress coordinate system in Figure 2a is centered about the z, or pressure axis in the rotated system in Figure 3a. The intersections between planes of constant pressure and any failure surface can be projected onto the x, y plane, and that plane is then referred to as the  $\pi$  plane. Figure 3b shows the  $\pi$  plane, with the failure surface now superimposed in terms of isobar curves. For the surface chosen in this example, the isobar curves are simply concentric circles.

There are six permutations of the algebraic order of  $\sigma_1, \sigma_2, \sigma_3$ . Hence the failure surface in the  $\pi$  plane consists of six symmetrical sectors. A failure surface defined in one sector can thus be obtained in the other sectors by series of mirror image transformations about the sector boundaries. The sector boundaries correspond to the conditions  $\sigma_2 = \sigma_3$  and  $\sigma_1 = \sigma_2$ , which are the triaxial compression and triaxial extension conditions defined by the footnote on page 81. Inserting the triaxial compression condition,  $\sigma_2 = \sigma_3$  into Eqn. (1), the sector boundary for this condition is  $y = \sqrt{3}x$ . Similarly the triaxial extension condition yields the sector boundary  $y = -\sqrt{3}x$ . These boundaries,  $y = \pm\sqrt{3}x$ , are actually planes, since they are valid for all pressures (values of z).

For the remainder of this discussion, we will consider only the sector in which  $\sigma_1 \geq \sigma_2 \geq \sigma_3$ . This sector of the  $\pi$  plane is shown in Figure 4. The left boundary corresponds to triaxial extension and the right boundary to triaxial compression. All data from experiments under these conditions will thus fall on these boundaries. Where a torsional loading component is present, the data will fall between the triaxial compression and extension boundaries.

The von Mises, Tresca, and Coulomb surfaces are conveniently plotted in the  $\pi$  plane as shown in Figure 4. The von Mises surface is defined as

$$2 J_2' = \sigma_1^{j*} \sigma_j^{i*} \leq 2/3 Y_M^2 \quad (2)$$

and the Tresca surface as

$$\sigma_1 - \sigma_3 \leq Y_T \quad (3)$$

where  $\sigma_j^{i*}$  is the deviatoric stress and Y represents the yield in uniaxial stress. These surfaces can be transformed to the rotated stress system by use of the following equation, which is derived from Eqn. (1).

$$x^2 + y^2 = R^2 = \frac{1}{3} [ (\sigma_1 - \sigma_2)^2 + (\sigma_1 - \sigma_3)^2 + (\sigma_2 - \sigma_3)^2 ] = \sigma_1^{j*} \sigma_j^{i*} \quad (4)$$

Thus in the  $\pi$  plane the von Mises condition is represented by a circle where

$$R = \sqrt{\sigma_1^{j*} \sigma_j^{i*}} = \sqrt{2J_2'} = \sqrt{\frac{2}{3}} Y_M \quad (5)$$

The Tresca condition in the  $\pi$  plane is a hexagon, or in the segment shown in Figure 4, simply the straight line  $y = Y_T/\sqrt{2}$ . Where Y varies with pressure, the von Mises and Tresca conditions are series of concentric circles and hexagons, respectively.

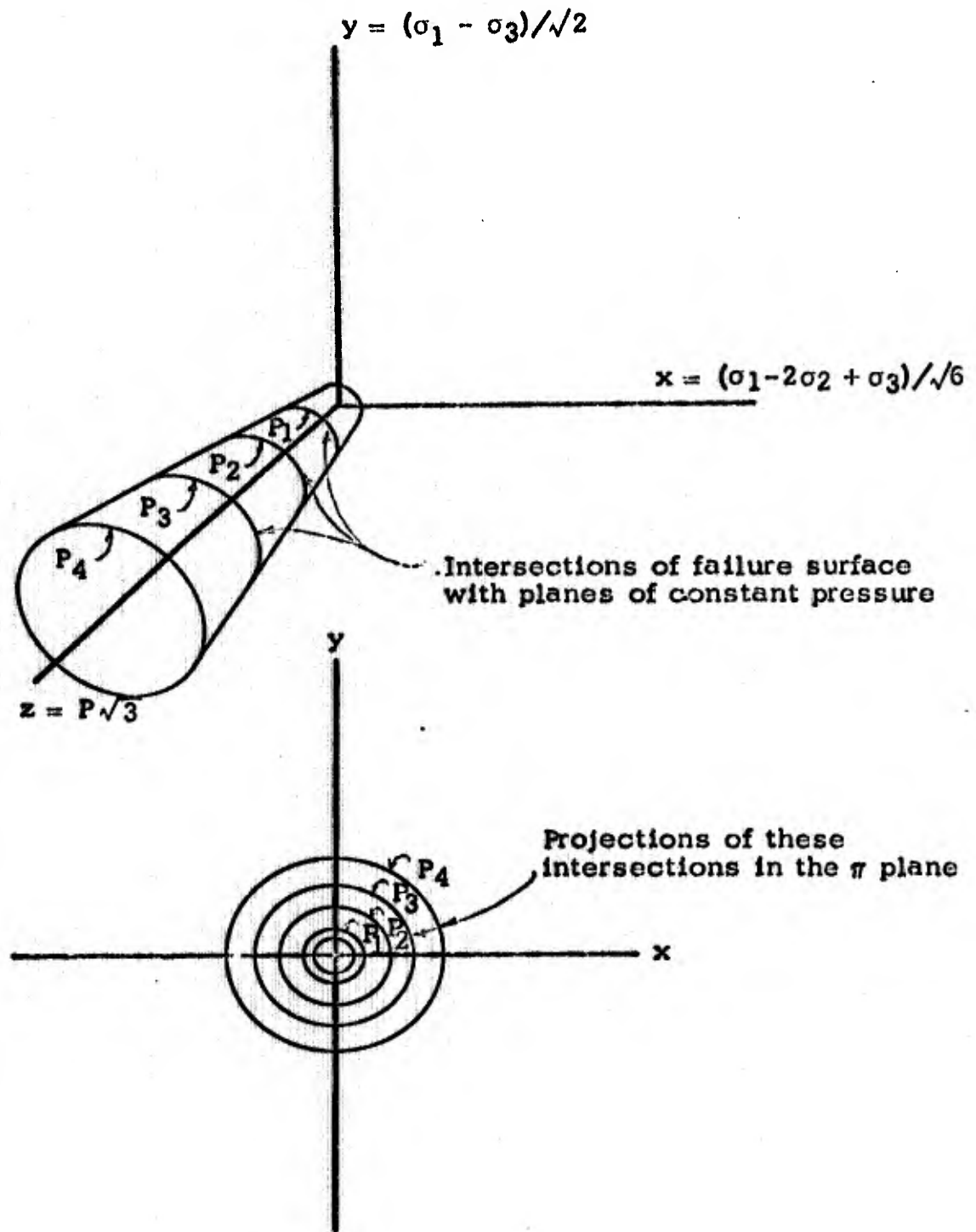


Figure 3. Rotation of Stress Space to  $(x, y, z)$  Coordinate System Showing Example of a Typical Axisymmetric Failure Surface.

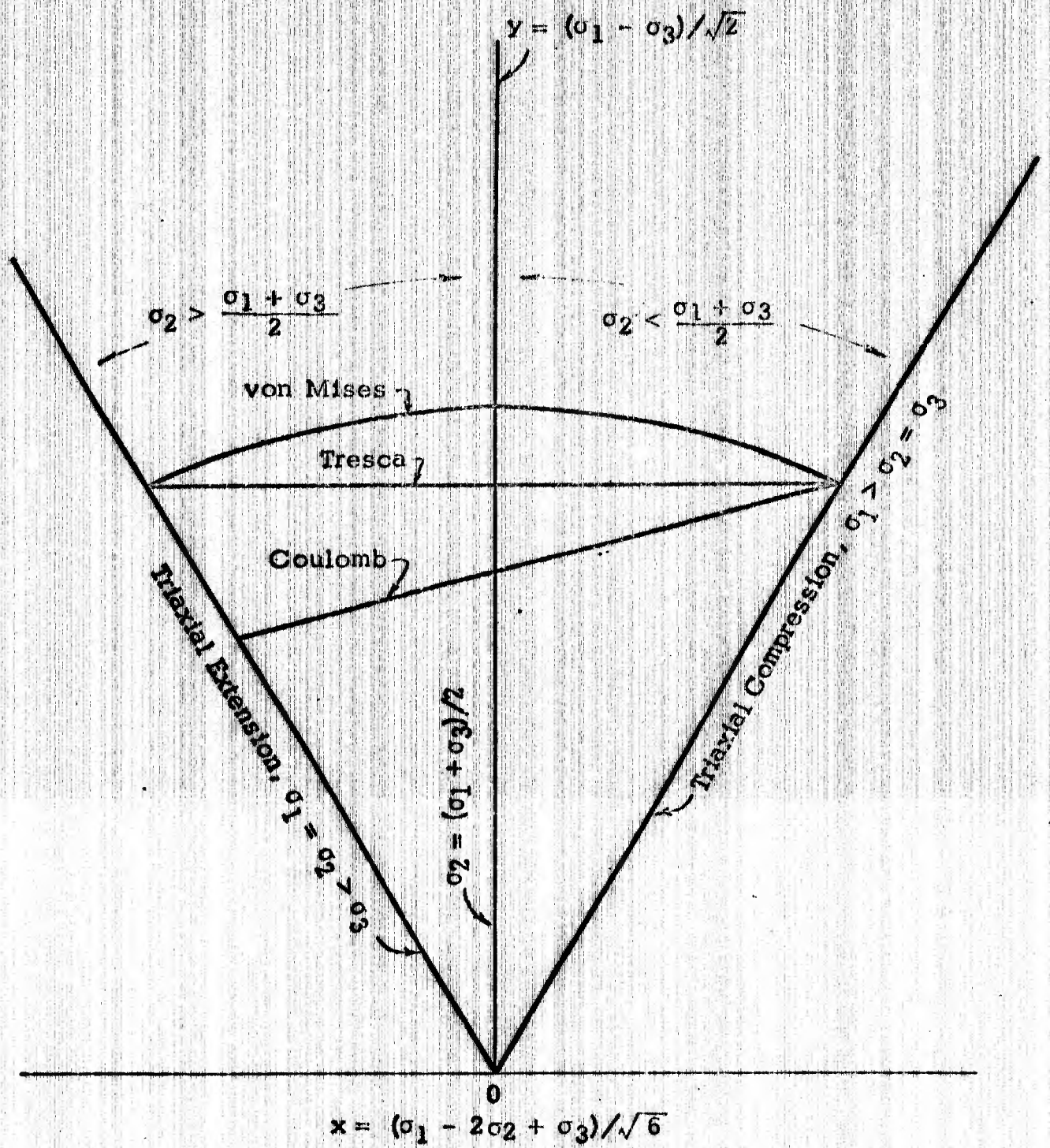


Figure 4.  $\sigma_1 \geq \sigma_2 \geq \sigma_3$  Sector of  $\pi$  Plane Showing Form of von Mises, Tresca, and Coulomb Criteria for One Pressure.

From the data in Figure 1, we see that the value of  $\frac{\sigma_1 - \sigma_3}{2}$ , and hence of  $y$  in Figure 4, is different for failure in triaxial compression vs triaxial extension. Hence neither the Tresca nor von Mises condition will satisfy the experimental data. To fit the data, the fracture line for a given pressure in the  $\pi$  plane must intersect the compression boundary at a higher value than the extension boundary. The Coulomb condition produces a fracture line of this type, as is seen in Figure 4. However, in the Coulomb model, all the straight lines between the compression and extension boundaries (corresponding to different pressure levels) have the same slope. As will be seen in the sections which follow, the experimental data do not conform to such a model.

### III-3. DETERMINATION OF THE STATIC FAILURE SURFACE FOR SOLENHOFEN LIMESTONE

Triaxial compression and triaxial extension data are available for many geological materials. However, data under torsion loading or biaxial loading are needed to determine the characteristics of the fracture surface between the triaxial compression and triaxial extension lines on a typical plane of constant pressure. Such torsion or biaxial data are unfortunately not common. In this study, Solenhofen limestone was chosen as the material to be investigated because pure torsion and torsion plus triaxial compression data are available in addition to the more common triaxial compression and tension data. Reference 1\* contains the data used in this study; they are summarized in Table I for convenience. The three principal stresses, as well as the corresponding coordinates in the rotated stress space are given in this table. However, in place of the  $z$  coordinate, the pressure ( $P = z/\sqrt{3}$ ) or mean stress is indicated. Table I is broken down into the triaxial compression, triaxial extension, and torsion data. The torsion data were either pure torsion with a super-imposed pressure or torsion plus triaxial compression. Thus the torsion data fall into the right half of the stress sector in the  $\pi$  plane shown in Figure 4.

The approach taken to fit the experimental data in Table I was to first use a least square fit program with a general quadric function to obtain the overall characteristics of the limestone fracture surface. Once these characteristics were identified, a physical model was formulated, and this model in turn was used to fit the experimental data.

#### III-3.1 THE LEAST SQUARE FIT TO THE LIMESTONE FRACTURE DATA

A general least square fit program was used which can accept an arbitrary function with any number of independent variables and any number of free parameters. The function used has the form,

$$y = F(x, P, a_1, a_2, \dots, a_M) \quad (6)$$

where the rotated stress  $y$  is the dependent variable related to  $x$ ,  $P$ , and the free parameter  $a_i$ . The assumed functional relationship between the depen-

---

\*Superscripts are reference numbers. The Reference List for Part III is on page 102.

TABLE I - FAILURE DATA FOR  
SOLENHOFEN LIMESTONE (from Ref. 1)

(Units are kilobars, positive stresses are compressive)

A. TRIAXIAL COMPRESSION ( $\sigma_1 > \sigma_2 = \sigma_3$ )

$\sigma_1$	$\sigma_2 = \sigma_3$	$x = \frac{\sigma_1 - 2\sigma_2 + \sigma_3}{\sqrt{6}}$	$y = \frac{\sigma_1 - \sigma_3}{\sqrt{2}}$	$P = \frac{\sigma_1 + \sigma_2 + \sigma_3}{3}$	$\frac{z}{\sqrt{3}}$
4.03	.35	1.50	2.60	1.58	
5.13	.69	1.81	3.14	2.17	
5.93	1.03	2.00	3.47	2.66	
6.63	1.38	2.14	3.71	3.13	
4.65	.35	1.76	3.04	1.78	
5.09	.69	1.80	3.11	2.16	
5.63	1.03	1.88	3.25	2.56	
3.47	0	1.42	2.45	1.16	
5.51	.76	1.94	3.36	2.34	
5.88	1.03	1.98	3.43	2.65	
5.66	1.03	1.89	3.27	2.57	
6.30	1.27	2.05	3.56	2.95	
6.60	1.53	2.07	3.59	2.55	
5.65	1.00	1.90	3.29	2.55	
7.76	3.00	1.94	3.37	4.58	
12.64	5.00	3.12	5.40	7.55	
3.98	0	1.62	2.81	1.33	
4.09	0	1.67	2.89	1.36	
3.98	0	1.62	2.81	1.33	
4.93	0.20	1.93	3.35	1.78	
5.33	.40	2.01	3.49	2.04	
5.45	.60	1.98	3.43	2.22	
5.94	.80	2.10	3.64	2.51	
6.35	1.00	2.18	3.78	2.78	
2.75	0	1.12	1.94	.92	
3.83	.30	1.44	2.50	1.48	
4.90	.98	1.60	2.77	2.29	
7.94	1.96	2.44	4.23	3.95	
8.92	2.94	2.44	4.23	4.93	
11.86	3.92	3.24	5.62	6.57	
2.72	0	1.11	1.92	.91	
4.06	.35	1.51	2.62	1.59	
4.62	.69	1.60	2.78	2.00	
5.31	1.04	1.74	3.02	2.46	
5.97	1.38	1.87	3.25	2.91	

TABLE I. (Cont'd) FAILURE DATA FOR SOLENHOFEN LIMESTONE  
(From Ref. 1)

(Units are kilobars, positive stresses are compressive)

B. TRIAXIAL EXTENSION ( $\sigma_1 = \sigma_2 > \sigma_3$ )

$\sigma_1 = \sigma_2$	$\sigma_3$	$x = \frac{\sigma_1 - 2\sigma_2 + \sigma_3}{\sqrt{6}}$	$y = \frac{\sigma_1 - \sigma_3}{\sqrt{2}}$	$P = \frac{\sigma_1 + \sigma_2 + \sigma_3}{3} = \frac{z}{\sqrt{3}}$
4.06	.04	-1.64	2.84	2.72
5.08	.42	-1.90	3.30	3.53
7.10	1.26	-2.38	4.13	5.15
7.62	1.32	-2.57	4.46	5.52
1.00	-.11	-.45	.79	.63
1.00	-.15	-.47	.81	.62
2.00	-.12	-.87	1.50	1.29
2.00	-.11	-.86	1.49	1.30
3.00	-.05	-1.25	2.16	1.98
3.00	-.14	-1.28	2.22	1.95

C. TORSION (HOLLOW CYLINDER)

$\sigma_1$	$\sigma_2$	$\sigma_3$	$x = \frac{\sigma_1 - 2\sigma_2 + \sigma_3}{\sqrt{6}}$	$y = \frac{\sigma_1 - \sigma_3}{\sqrt{2}}$	$P = \frac{\sigma_1 + \sigma_2 + \sigma_3}{3} = \frac{z}{\sqrt{3}}$
.147	0	-.147	0	.208	0
2.059	1.00	-.059	0	1.498	1.00
3.346	2.00	.654	0	1.904	2.00
3.952	2.00	.048	0	2.761	2.00
5.552	3.00	.448	0	3.609	3.00
5.851	3.00	.149	0	4.032	3.00
7.045	4.00	.955	0	4.306	4.00
7.338	4.00	.662	0	4.721	4.00
1.057	0	-.177	.359	.848	.29
3.527	1.00	.103	.665	2.319	1.54
5.198	2.00	.202	.572	3.366	2.47
4.592	2.00	1.038	.665	2.404	2.54
6.877	3.00	.754	.665	4.115	3.54
7.193	3.00	.437	.665	4.533	3.54
7.173	3.00	.457	.665	4.497	3.54
8.025	4.00	1.605	.665	4.313	4.54
6.517	2.00	.054	1.049	4.355	2.86
7.535	3.00	1.035	1.049	4.412	3.86
6.542	3.00	2.198	1.119	2.970	3.91

dent and independent variables is specified by a function  $F$  which involves the  $M$  free parameters  $a_i$  which are to be fit to the experimental data. These data are in the form  $(y^j, x^j, p^j)$  from Table I. For a given choice of the free parameters  $a_i$  the function  $F$  can be evaluated for a given data point. Then the error between the function  $F$  and the experimental point is formed by

$$E^j = y^j - F^j, \quad j = 1, N \quad (7)$$

where  $y^j$  is from the experimental data, and  $F^j = F(x^j, p^j, a_1, a_2, \dots, a_M)$ .  $j$  ranges over the  $N$  data points. The cumulative squared error is defined by

$$E^2 = \sum_{j=1}^N (E^j)^2 \quad (8a)$$

and the cumulative percent squared error is

$$E_{\%}^2 = \sum_{j=1}^N \left( \frac{E^j}{y^j} \right)^2 \quad (8b)$$

Notice that for a given set of experimental data  $E^2$  and  $E_{\%}^2$  depend only on the form of the function  $F$  and the free parameters  $a_i$ . The least square fit program will solve for the free parameters  $a_i$  once  $F$  is chosen. The coefficients  $a_i$  will be found such that either  $E^2$  or  $E_{\%}^2$  is minimized.

The function  $F$  first chosen to fit the experimental data was

$$y = F = a_1 + a_2 x + a_3 P + \sqrt{a_4 + a_5 x + a_6 P + a_7 P + a_8 x^2 + a_9 P^2} \quad (9)$$

This general quadric form was chosen because most of the commonly used forms for fracture surfaces and yield surfaces are contained as special cases. For example, from Eqn. (4) and (5), the von Mises yield condition can be put in the following form

$$y = F = \sqrt{2/3 Y_M^2 - x^2} \quad (10)$$

where

$$2/3 Y_M^2 = a_4 + a_6 P + a_9 P^2 \quad (11)$$

Also, note that the yield in uniaxial stress  $Y_M$  can vary with the pressure to form a conical surface in stress space. Similarly, a modified Tresca condition can be simulated with the quadric Eqn. (9) in the following form

$$Y = F = a_1 + a_3 P + \sqrt{a_4 + a_6 P + a_9 P^2} \quad (12)$$

The above examples all have the property that they are symmetrical in the rotated stress space about the line  $x = 0$ . However, note that the general form of Eqn. (9) has the capability of being non-symmetrical. Thus, the non-symmetrical aspect of the triaxial compression and triaxial extension data can be accommodated.

Using the form of Eqn. (9), the least square fit program was executed in the least square percent sense, i.e. the coefficients  $a_1$  through  $a_9$  were found such that the cumulative squared percent error,  $E_{\%}^2$ , was minimized. Figure 5 shows the resulting failure surface fit on the  $\pi$  plane, and also gives the values of the coefficient for the quadric fit. The lines are projections of the failure surface intercepts on constant pressure planes at 0, 1, 2, 3, 4, and 5 kilobars. The failure surface is seen to expand with increasing pressure. Note particularly that the quadric fit of the experimental data produces a failure surface consisting of nearly straight line isobar projections on the  $\pi$  plane. The slope of the isobar lines decreases as the pressure increases, indicating that the difference between the  $y$ -intercept  $(\frac{\sigma_1 - \sigma_2}{\sqrt{2}})$  in triaxial compression and in triaxial extension decreases as the pressure rises.

The qualitative features of the general quadric fit in Figure 5 suggest the physical model for rock failure which is presented in the section which follows.

### III-3.2 A PHYSICAL MODEL FOR THE LIMESTONE FAILURE SURFACE

As pointed out previously, neither the von Mises, Prager-Drucker, nor Tresca models will accommodate the differences in triaxial compression and extension failure data which are observed in experiments on rocks. The Coulomb fracture criterion however, can show this characteristic, and we used that criterion as the basis for a physical model for describing the failure surface of limestone. Specifically, the Coulomb fracture criterion was modified to include a less restrictive dependence on pressure and also to include a test for tensile failure.

The Coulomb fracture criterion assumes that the shear stress tending to cause failure across a plane is resisted by the cohesion of the material and by a constant times the normal stress across the plane. Thus, shear failure is assumed to occur in a plane if

$$|\tau| = S_0 + \tan \phi \sigma_n \quad (13)$$

where  $|\tau|$  is the magnitude of the shear on the plane,  $\sigma_n$  is the normal stress on the plane,  $S_0$  is a constant which represents an inherent shear strength of the material, and  $\tan \phi$  is a constant analogous to the coefficient of sliding friction.

In Ref. 2 it is shown that fracture according to the Coulomb criterion will occur on a plane which contains the  $\sigma_2$  axis and which is oriented at an angle  $\theta_f$  from the  $\sigma_1$  axis where  $\theta_f$  is given by

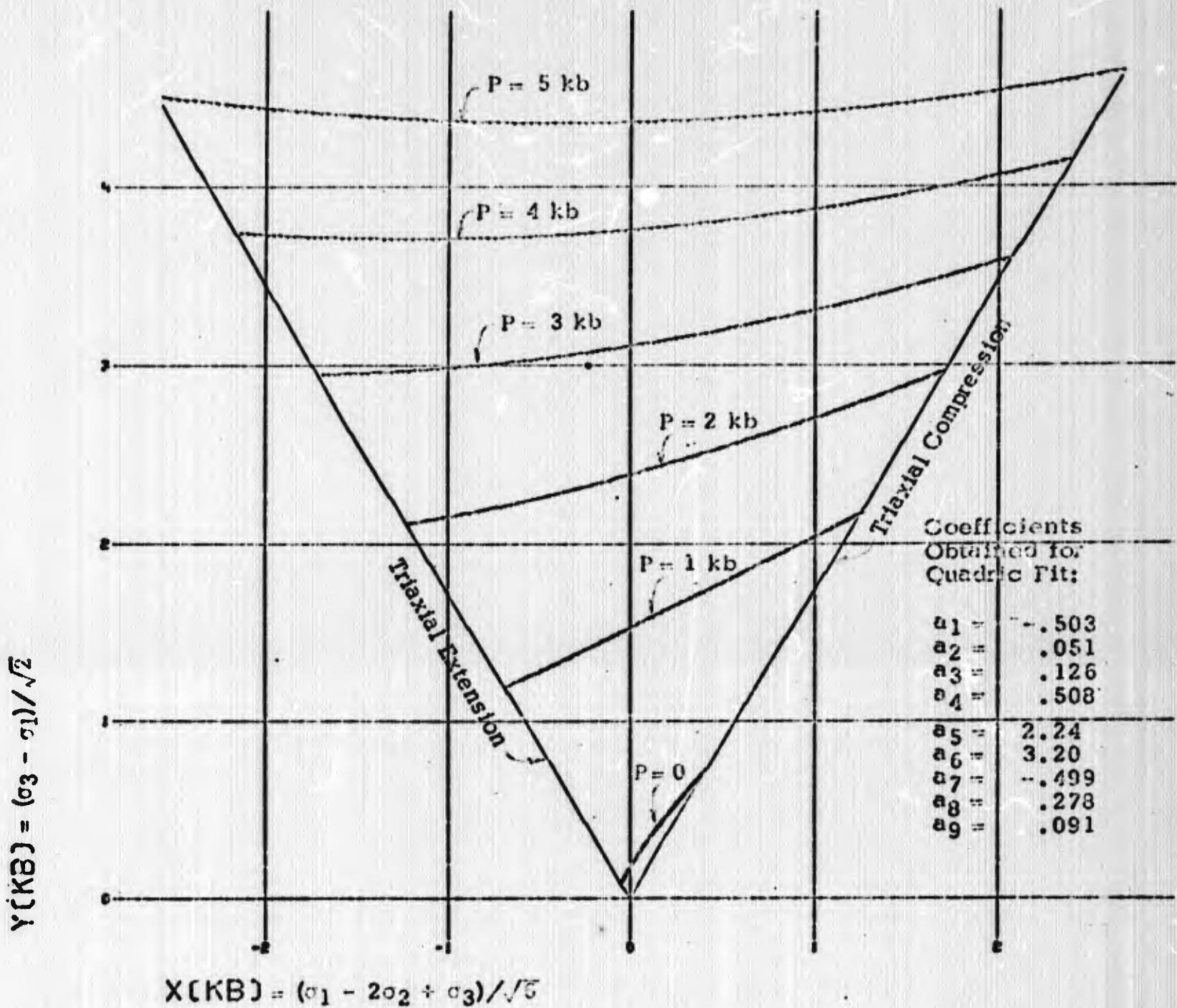


Figure 5. Solenhofen Limestone Failure Surface in  $\pi$  Plane, Obtained by Least Square Fit of Data from Ref. 1 Using General Quadratic Form,  $y = a_1 + a_2 x + a_3 P + \sqrt{a_4 + a_5 x + a_6 P + a_7 xP + a_8 x^2P + a_9 P^2}$

$$\theta_f = \pm (45^\circ - \phi/2) \quad (14)$$

It is also shown in Ref. 2 that the following relationship holds at fracture.

$$\frac{\sigma_1 - \sigma_3}{2} = S_0 \cos \phi + \left( \frac{\sigma_1 + \sigma_3}{2} \right) \sin \phi \quad (15)$$

Eqn. (15) is an equivalent form of the statement of the Coulomb fracture criterion given by Eqn. (13), and takes into account the angle of the plane on which shear failure will occur.

Eqn. (15) can be put in terms of the rotated stress coordinates by using the relationships

$$\begin{aligned} \frac{\sigma_1 - \sigma_3}{2} &= \frac{y}{\sqrt{2}} \\ \frac{\sigma_1 + \sigma_3}{2} &= \frac{x}{\sqrt{6}} + \frac{z}{\sqrt{3}} = \frac{x}{\sqrt{6}} + P \end{aligned} \quad (16)$$

Putting these relationships into Eqn. (15) we find

$$y = \sqrt{2} [S_0 \cos \phi + \left( \frac{x}{\sqrt{6}} + P \right) \sin \phi] \quad (17)$$

Equation (17) thus represents the Coulomb shear fracture criterion in terms of the rotated stress space coordinates (where P has been used in place of  $z/\sqrt{3}$ ). It shows that on every plane of constant P the fracture surface will be represented by a straight line with constant slope  $\sin \phi / \sqrt{3}$ .

The Coulomb criterion has the property that the fracture surface expands with increasing pressure. However, the expansion is constrained to be linear with the pressure. The fit to the limestone data shown in Figure 4 demonstrates that the Coulomb criterion must be generalized if it is to be used to fit the experimental data. The generalization must permit the slopes  $\left. \frac{\partial y}{\partial x} \right)_P$ , of the isobar projections on the  $\pi$  plane to vary with pressure and it must also permit a non-linear expansion of the fracture surface with pressure. Both these generalizations can be achieved by assuming  $S_0$  and  $\phi$  are functions of pressure. We then have the following relationships for the slope and for the intercept of the failure surface on the line  $x = 0$  for any given pressure:

$$\begin{aligned} \left. \frac{\partial y}{\partial x} \right)_P &= \frac{\sin \phi (P)}{\sqrt{3}} \\ y(x=0) &= \sqrt{2} [S_0 (P) \cos \phi (P) + P \sin \phi] \end{aligned} \quad (18)$$

In Eqn. (18),  $\phi(P)$  determines the slope of the isobar lines, and  $S_0(P)$  determines the expansion of the failure surface as measured by the y intercept on the  $\pi$  plane.

Equation (17), with  $S_0$  and  $\phi$  being functions of pressure, represents the modified Coulomb criterion used to represent shear fracture. In addition to shear fracture, however, tensile fracture occurs in certain stress regimes. The modified Coulomb criterion is not applicable under these conditions. For tensile fracture we will therefore make the additional assumption that

$$\sigma_3 = -T_0 \quad (19)$$

where the critical tensile stress,  $T_0$ , is assumed to be constant. Transforming Eqn. (19) into the rotated stress space,

$$y = \sqrt{2} \left( T_0 + \frac{x}{\sqrt{6}} + P \right) \text{ (Tensile fracture)} \quad (20)$$

Note that Eqns. (20) and (17) are of the same form if we identify  $S_0 \cos \phi$  with  $T_0$  and  $\sin \phi$  is set to 1.

The pressure dependence of  $S_0 \cos \phi$  and  $\sin \phi$  in Eqn. (17) were chosen as follows. First, the term  $S_0 \cos \phi$  was assumed to obey a quadratic relationship of the form

$$S_0 \cos \phi = a_1 P^2 + a_2 P + a_3 \quad (21)$$

Since  $\sin \phi$  is proportional to the slope of the isobar curves on Figure 5, we assumed it to be satisfied by

$$\sin \phi = a_4 e^{-a_5 P} \quad (22)$$

This relationship causes the slopes of the isobar lines in the  $\pi$  plane to decrease with increasing pressure and to asymptotically go to zero as the pressure goes to infinity.

Finally, by letting the critical tensile stress  $T_0$  be represented by the free coefficient  $a_6$ , we obtained the following form for the limestone failure surface

$$y = \text{Min} \{ y_S, y_T \}$$

where

$$y_S = \sqrt{2} \left[ S_0 \cos \phi + \left( \frac{x}{\sqrt{6}} + P \right) \sin \phi \right]$$

$$y_T = \sqrt{2} \left[ T_0 + \frac{x}{\sqrt{6}} + P \right] \quad (23)$$

and

$$S_0 \cos \phi = a_1 P^2 + a_2 P + a_3$$

$$\sin \phi = a_4 e^{-a_5 P}$$

$$T_0 = a_6$$

Using the least square fit program, we found the following coefficients for the least square percent error fit.

$$a_1 = .0071 (kb)^{-1}$$

$$a_2 = .374$$

$$a_3 = .216 (kb)$$

$$a_4 = .808$$

$$a_5 = .331 (kb)^{-1}$$

$$T_0 = a_6 = .144 (kb)$$

(24)

Figure 6 shows this modified Coulomb failure surface for limestone in the  $\pi$  plane. The  $P = 0$  failure curve consists entirely of tensile fracture. The  $P = 1$  kb curve consists partially of tensile fracture (indicated by a dashed line in Figure 6) and partially of shear failure. Above  $P = 2$  kb, the failure surface is due entirely to shear failure.

The least percent error square fit to the limestone failure data has a percent standard deviation of 11.3%. The maximum percent error was 35.6%.

The modified Coulomb model fit is also superimposed on the experimental triaxial compression and triaxial extension data shown in Figure 1. The region where tensile fracture occurs is indicated by a dashed line.

The two parameters,  $\sin \phi$  and  $S_0 \cos \phi$  which determine the details of the modified Coulomb fracture model are illustrated in Figure 7. These curves can be used to graphically obtain the characteristics of the limestone fracture surface. Note that this surface is a fit to the data up to pressures of about 5 or 6 kb. There are not sufficient data to justify extension to higher pressures.

### III-3.3 COMPARISON WITH RECENT BIAxIAL STRESS DATA

At the time when the modified Coulomb fit described in the prior section was made, no published data for limestone failure under loading states in the left side of the  $\pi$  plane sector shown in Figure 4 were available to us (i.e. for states between  $x = 0$  and the left, triaxial extension boundary.) The

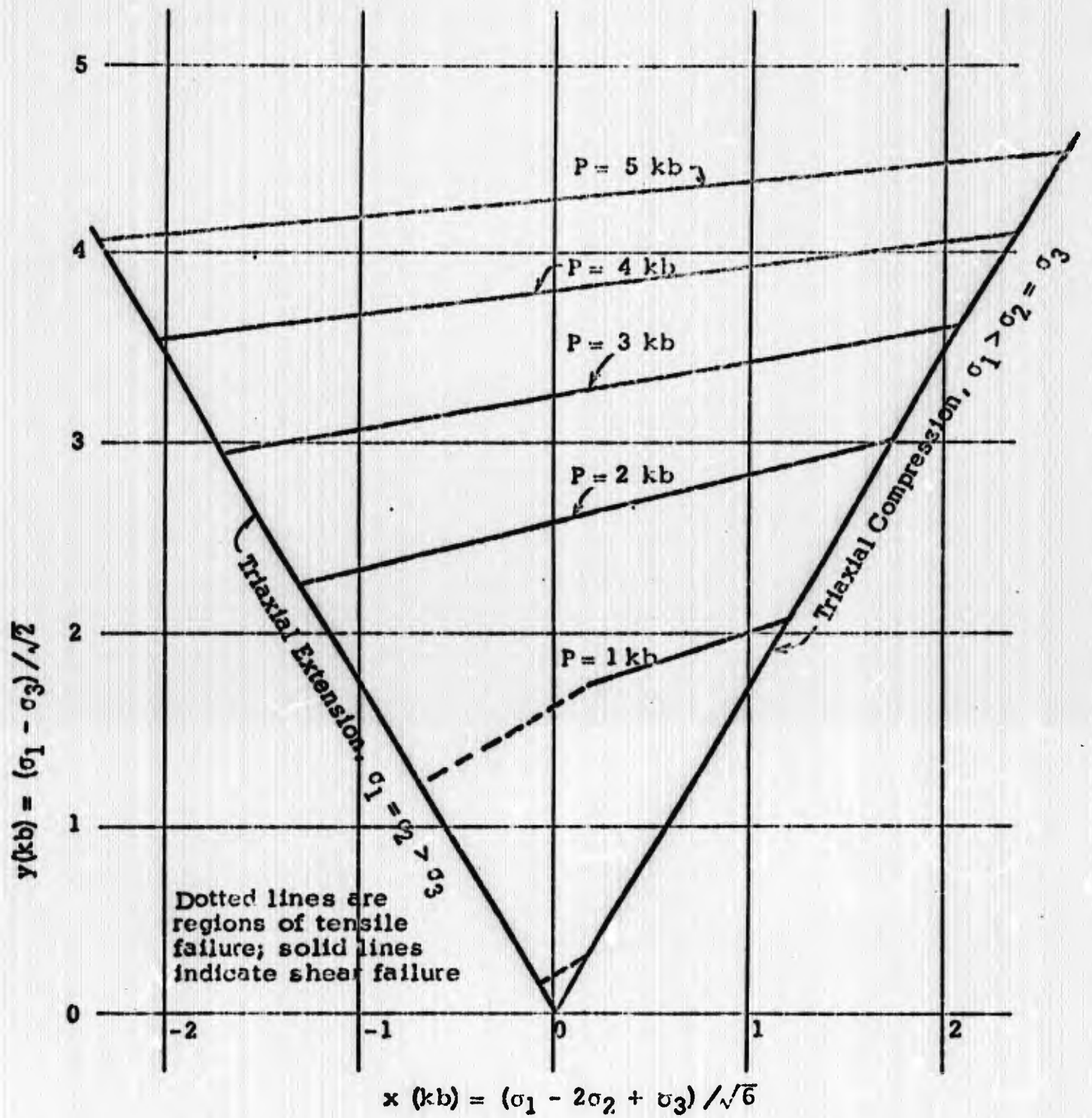


Figure 6. Modified Coulomb Model Fit of Solenhofen Limestone Failure Surface in the  $\pi$  Plane, Obtained by Least Square Fit of Data from Ref. 1.

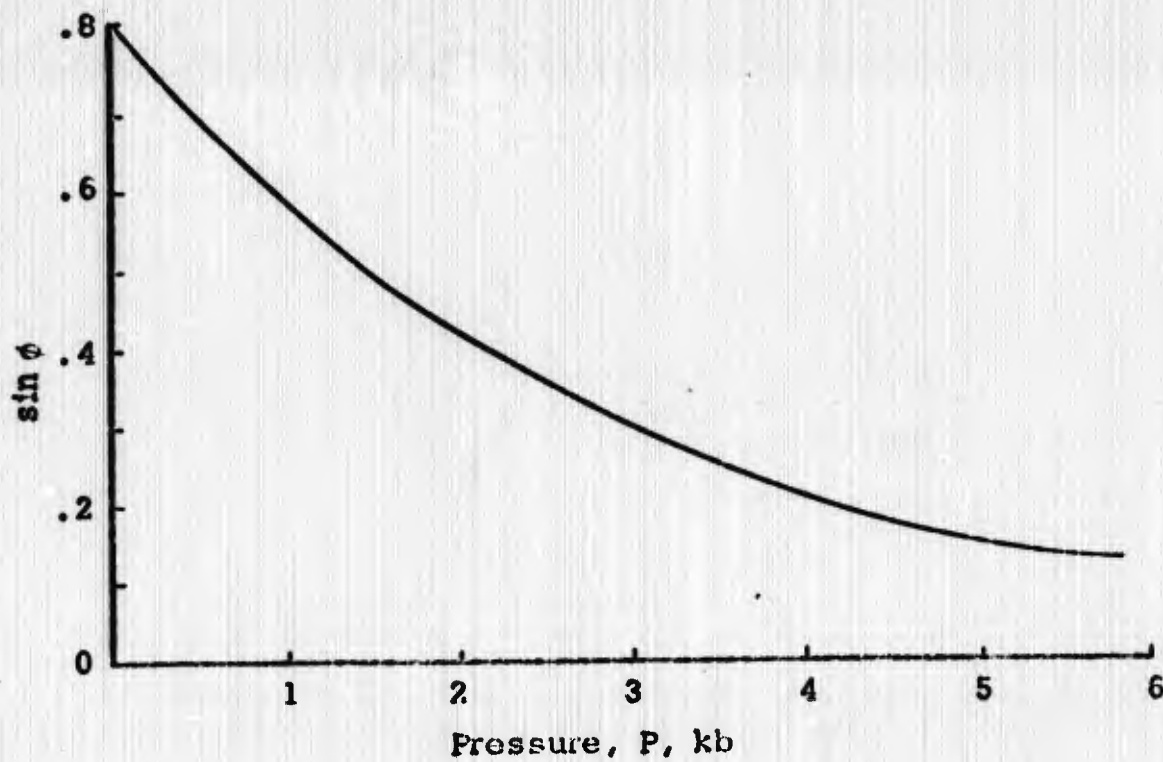
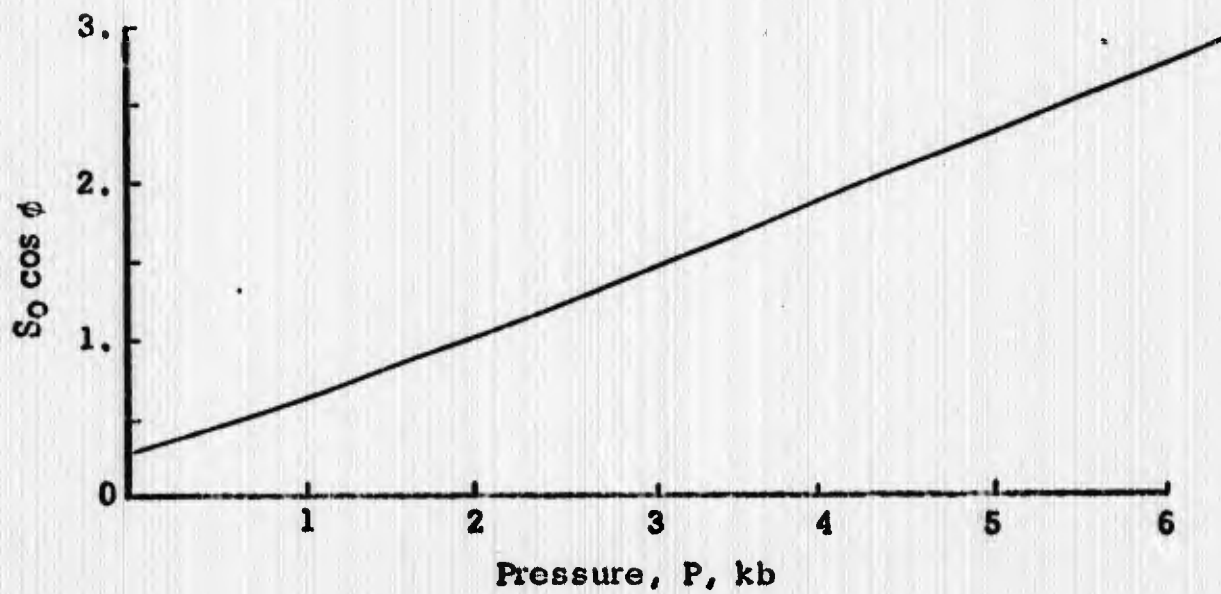


Figure 7.  $S_0 \cos \phi$  and  $\sin \phi$  in Modified Coulomb Model as Function of Pressure For Solenhofen Limestone.

straight line fit across that sector of the  $\pi$  plane was therefore uncertain. It is therefore of considerable interest to compare recently published data points obtained under biaxial loading states which fall in the left side of the  $\pi$  plane sector with the modified Coulomb model fit. In Table II, the low strain rate ( $< 10^{-4} \text{ sec}^{-1}$ ) data from Ref. 3 are tabulated in terms of principal stresses and also the rotated stress coordinates,  $x$ ,  $y$ , and  $P$ . (Also included from Ref. 3 are the results of two triaxial compression tests.) The values of  $y$  obtained from the modified Coulomb fit at the specified conditions of  $x$  and  $P$  are also shown, along with the percentage errors. The percentage errors are seen to be relatively small ( $< 10\%$ ).

TABLE II - COMPARISON OF MODIFIED COULOMB FIT FOR SOLENHOFEN LIMESTONE WITH INDEPENDENT EXPERIMENTAL DATA.  
(Units are kilobars, positive stresses are compressive)

Loading	Experimental (Ref. 3)						Modified Coulomb Fit $y_{\text{model}}$	error
	$\sigma_1$	$\sigma_2$	$\sigma_3$	$P$	$x_{\text{exp}}$	$y_{\text{exp}}$		
Biaxial	3.92	3.50	0	2.77	-1.26	2.77	2.65	4.0%
Biaxial	4.00	2.04	0	2.01	-.033	2.83	2.58	8.7%
Triaxial	2.75	0	0	.92	1.12	1.94	1.96	0.9%
Triaxial	4.4	.5	.5	1.8	1.59	2.76	2.83	2.8%

#### III-4. SUMMARY AND RECOMMENDATIONS

Triaxial compression, triaxial extension, torsion, and biaxial failure data ( $P < 7 \text{ kb}$ ) for Solenhofen Limestone have been fit using the modified Coulomb fracture models described in Section 3.2. Both shear and tensile failure are treated. Shear failure for a fixed mean stress (pressure) is represented by a straight line in the  $\sigma_1 \leq \sigma_2 \leq \sigma_3$  sector of the  $\pi$  plane (see Figure 6). The slope of the family of failure lines in the  $\pi$  plane sector decrease with an increase in pressure. Thus the differences between triaxial compression and extension become less important at high pressures. The model fits the data with an 11.3% standard deviation and a maximum percent error of 35.6%.

The generality of the model to other geological materials is not known. Many rocks show the same qualitative behavior as limestone in triaxial compression and triaxial extension failure tests. In general, however, there is not sufficient failure data in the stress region  $\sigma_1 / \sigma_2 \neq \sigma_3$  to conclude that at a constant pressure a linear fit is adequate in a  $\pi$  plane sector. On the other hand, if we assume that the forms used for limestone are applicable to

other geological materials, then the data from triaxial compression and triaxial extension tests can be used to specify the entire failure surface.

We recommend that the validity of the modified Coulomb model be experimentally tested for granite and other rocks of interest. Also, since the percent differences in triaxial compression failure as compared to triaxial extension failure at low pressures ( $P < 2$  kb) are relatively large in limestone and many other rocks, we recommend that sensitivity analyses be performed to determine the importance of this failure characteristic on ground motion and cratering calculations.

### III-5. REFERENCES FOR PART III

1. Handin, J., Heard, H. C., and Magouirk, J. N., "Effects of the Intermediate Principal Stress on the Failure of Limestone, Dolomite, and Glass at Different Temperatures and Strain Rates," *J. Geophys. Res.*, 72, 611, January 1967.
2. Jaeger, J. C. and Cook, N.G.W., Fundamentals of Rock Mechanics, Methuen & Co., Ltd., London 1969.
3. Green, S. J., Leasia, J. D., Perkins, R. D., and Jones, A. H., "Multiaxial Stress Behavior of Solenhofen Limestone and Westerly Granite at High Strain Rates," TR-71-10, Terra Tek, Inc., Salt Lake City, Utah, January 1971 (Submitted to *J. Geophys. Res.*)